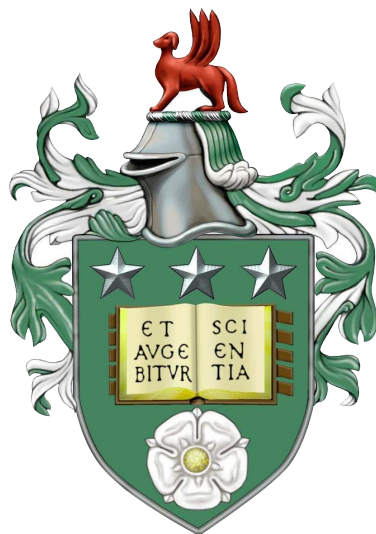


Interface morphology and Dzyaloshinskii-Moriya interaction in Pt/Co thin films

Adam William John Wells



School of Physics and Astronomy
University of Leeds

Submitted in accordance with the requirements for the degree of
Doctor of Philosophy

August 2017

Intellectual Property and Publication Statements

The candidate confirms that the work submitted is his own and that appropriate credit has been given where reference has been made to the work of others.

This copy has been supplied on the understanding that it is copyright material and that no quotation from the thesis may be published without proper acknowledgement.

The right of Adam William John Wells to be identified as Author of this work has been asserted by him in accordance with the Copyright, Designs and Patents Act 1988.

© 2017 The University of Leeds and Adam William John Wells

Publications

1. A. W. J. Wells, P. M. Shepley, C. H. Marrows, and T. A. Moore. Effect of interfacial intermixing on the Dzyaloshinskii-Moriya interaction in Pt/Co/Pt. *Phys. Rev. B*, 95:054428, 2017
2. A. Hrabec, N. A. Porter, A. Wells, M. J. Benitez, G. Burnell, S. McVitie, D. McGrouther, T. A. Moore, and C. H. Marrows. Measuring and tailoring the Dzyaloshinskii-Moriya interaction in perpendicularly magnetized thin films. *Phys. Rev. B*, 90:020402(R), 2014
3. R. A. Khan, P. M. Shepley, A. Hrabec, A. W. J. Wells, B. Ocker, C. H. Marrows, and T. A. Moore. Effect of annealing on the interfacial Dzyaloshinskii-Moriya interaction in Ta/CoFeB/MgO trilayers. *Appl. Phys. Lett.*, 109:132404, 2016
4. S. Langenfeld, V. Tshitoyan, Z. Fang, A. W. J. Wells, T. A. Moore, and A. J. Ferguson. Exchange magnon induced resistance asymmetry in permalloy spin-Hall oscillators. *Appl. Phys. Lett.*, 108:192402, 2016

Acknowledgements

For all his guidance, ideas and encouragement, I am grateful to my supervisor, Dr Tom Moore, without whom this thesis would never have come into being. Thank you for your patience, understanding and willingness to be there whenever a discussion is needed. I would also like to thank Prof. Chris Marrows, my co-supervisor, whose advice on reports, publications and all of my formal writing was invaluable.

My thanks also go to Dr Mannan Ali, whose training and experience in all things experimental have allowed for far more progress than would have been made otherwise, and to Dr Gavin Burnell for his patience in sorting the coding issues encountered during the running of many of the machines. Thanks also to the rest of the academic staff for their encouragement throughout this PhD; and for all those from other universities for their collaborations, even though none have made it into this thesis.

For the ideas and discussion within the ‘DMI club’, Aleš, Risalat, Kowsar and Philippa have my great gratitude. I am grateful also to everyone else in the condensed matter group, particularly Amy, Rowan, Fatma, George and Tim, and the wider University of Leeds School of Physics for their part in the creation of an environment of friendly discussion.

To my parents, I give thanks for their encouragement, love and restorative powers during sojourns at home, and for raising me with an appreciation of the world and its wonders. To my brother, Graham, for always being there and being all that a brother should be. For my friends, both near and far, for their support, especially my small group and team awesome. Many thanks are owed to God for His guidance and what strength and wisdom He has given me. Finally, I’d like to thank my fiancée, Liz, for her love, support and encouragement, being there when I need her and making sure I don’t starve.

Abstract

The interfacial morphology and the Dzyaloshinskii-Moriya interaction (DMI) have been investigated in thin films of perpendicularly-magnetised epitaxial Pt(30 Å)/Co(7 Å)/Pt(10 Å) and Pt(30 Å)/Co(7, 9, 11 Å)/Ir₂₀Mn₈₀(20, 50 Å). In Pt/Co/Pt, altering the substrate temperature during deposition of the top Co/Pt bilayer in the range of 100°C to 300°C formed a peak in total interfacial disorder with deposition temperature of 3.3 Å at around 250°C. The coercivity increased from 230±60 Oe to 400±60 Oe whilst the anisotropy and saturation magnetisation stayed constant at 15.0±0.3 kOe and 90±10 μemu, respectively, when the substrate temperature at deposition was reduced in value. In contrast, the anisotropy increased with deposition temperature if either the substrate temperature was increased, or the deposition temperature of only the top Pt layer was varied, though not both simultaneously.

The bubble domain expansion technique was used to measure domain wall velocity with applied magnetic fields in various in-plane (IP) and out-of-plane (OOP) configurations. Of the three prominent creep models used, it was found that the most basic model fitted best. A moderate linear correlation was seen between DMI and the difference in disorder between the top and bottom Co interfaces, indicating that as the disorder in one interface increases, its contribution to DMI decreases, allowing the relative interface disorders to dictate the strength, and even sign, of the net DMI. The net DMI increased with increasing deposition temperature, also, showing that such a growth parameter can be used to fine-tune the DMI.

Using Pt/Co/Ir₂₀Mn₈₀ samples, the growth temperature and working pressure were optimised for DMI measurements. Samples with 50 Å of IrMn, with exchange bias strengths up to 1000 Oe, showed a high density of small, rough domains forming during magnetisation reversal. Samples with 20 Å of IrMn, so without exchange bias, produced well-formed bubble domains for Co thicknesses below 9 Å, with a Voronoi-like network seen in an 11 Å sample. Bubble domain expansion showed severely skewed velocity against IP field graphs, with behaviour at higher fields not predicted by

current models, giving DMI constant values between -0.6 and -1.0 mJ/m².

Contents

1	Introduction	1
1.1	Thesis overview	3
2	Literature review	5
2.1	Pt/Co structures	8
2.2	Domain wall creep	15
2.2.1	Theory	15
2.2.2	Spin torques theory	17
2.2.3	Review	21
2.3	Dzyaloshinskii-Moriya interaction	26
2.3.1	Magnetic energy theory	26
2.3.2	Review	29
2.4	Perpendicular exchange bias	42
2.5	Conclusions	49
3	Methodology	51
3.1	Sample deposition	51
3.2	Sputtering	53
3.3	X-ray reflection and diffraction	56
3.3.1	X-ray theory	57
3.3.2	X-ray techniques	64
3.4	Magneto-optical Kerr effect	65
3.4.1	Magneto-optical Kerr effect theory	65
3.4.2	Magneto-optical Kerr effect techniques	67

3.5	Anisotropy measurements	68
3.6	Vibrating sample magnetometry	70
3.7	Kerr microscopy	71
3.7.1	Bubble domain expansion	72
3.7.2	Python fitting software	72
3.7.3	Domain wall annihilation	73
3.7.4	Other DMI measurement techniques	73
4	Sample deposition and characterisation	75
4.1	Introduction	75
4.2	Sputtering gun stability	77
4.3	X-ray characterisation	77
4.3.1	High angle X-rays	78
4.3.2	Low angle X-rays	80
4.3.3	Rocking curves	85
4.4	Magnetic characterisation	87
4.4.1	Magneto-optical Kerr effect	88
4.4.2	Anisotropy measurements	91
4.4.3	Vibrating sample magnetometry	95
4.5	Sustainability	95
4.6	Conclusions	96
5	Magnetic field-induced domain wall motion in Pt/Co/Pt	98
5.1	Kerr microscopy	99
5.1.1	Domain wall velocity measurement	99
5.1.2	Magnet Design	100
5.2	Creep Regime Test	102
5.3	In-plane field dependence of domain walls velocity	104
5.4	Analysis models	106
5.4.1	Domain wall energy variation model	106
5.4.2	Universal creep law model	108
5.4.3	Rough wall model	110
5.4.4	Model Summary	112

5.5 Dzyaloshinskii-Moriya interaction measurement	112
5.6 Conclusions	117
6 Magnetic field-induced domain wall motion in exchange bi- ased systems	119
6.1 Deposition	120
6.2 Characterisation	122
6.2.1 Structural	122
6.2.2 Magnetic	125
6.3 Domain wall structures	133
6.4 DMI	136
6.5 Conclusions	143
7 Conclusions	145
7.1 Future work	149
A Domain wall velocity fits	168

Abbreviations

DMI	Dzyaloshinskii-Moriya interaction
DW	domain wall
PMA	perpendicular magnetic anisotropy
OOP	out-of-plane
IP	in-plane
OHE	ordinary Hall effect
SHE	spin Hall effect
AHE	anomalous Hall effect
SOC	spin-orbit coupling
TAFF	thermally-assisted flux flow
XRR	X-ray reflection
LAX	low-angle X-ray
XRD	X-ray diffraction
HAX	high-angle X-ray
MOKE	magneto-optical Kerr effect
VSM	vibrating sample magnetometer
TEM	transmission electron microscopy
STM	scanning tunnelling microscopy
AFM	atomic force microscopy
WHOOP	water-cooled homebuilt out-of-plane (coil)
fcc	face-centred cubic

CONTENTS

hcp hexagonal close-packed

ML monolayers

Chapter 1

Introduction

‘Space is big. Really big. You just won’t believe how vastly hugely, mind-bogglingly big it is. I mean, you may think it’s a long way down the road to the chemist, but that’s just peanuts to space.’[5]. Yet all of it, so far as we know, is governed by the same set of laws and mechanisms. Thus, a scientific discovery here on Earth can give us knowledge about the entire universe. With such a vast array of possible topics, it is, then, necessary to specialise. Some truly fascinating effects can be seen, for example, when matter is brought together in close proximity, giving us the scientific discipline of condensed matter physics. The plethora of different ways in which atoms can combine and interact through such effects as spin-orbit coupling and the exchange interaction allow novel magnetic phenomena to manifest. It is the study of a subset of these phenomena, namely the Dzyaloshinskii-Moriya interaction and its connection to structural morphology and exchange bias on which this thesis focuses. Out of the many material systems available for study, Pt/Co systems have been used in this thesis, and in many other studies, due to their propensity for high perpendicular magnetic anisotropy, their high crystallinity and their relatively simple structure. To make this structure close to a model system, a further specialisation is taken into purely epitaxial samples.

Condensed matter physics is a discipline which has seen great advances in recent decades, in part due to the technological revolution brought about by

the computer. Emerging devices have increasingly used the phenomena studied in condensed matter physics to improve data processing speed, increase density of data storage and create new functions. As a non-volatile means of storing data, magnetism has been amongst the foremost topics studied. First postulated in 1888 by Oberlin Smith[6] and brought to fruition by Valdemar Poulsen[7], magnetic storage has been gradually improved to the level of magnetic hard-drives with storage densities of 1 terabit per square inch in 2012[8] and ones capable of storing 10 terabytes being released for general sale last year[9]. With solid-state flash drives reaching that level of storage, but with much faster access, new methods of magnetic storage are being investigated which combine the speed and shock-resistance of flash memory with the lifetimes of magnetic storage. One such method is that of racetrack memory, in which magnetic domains are shifted along a strip of material over a read/write head[10, 11].

For racetrack memory to become viable, the domain walls must be able to be moved quickly in the same direction, without colliding or annihilating each other. In order to move all domain walls in the same direction, regardless of their chirality, a current can be used with its associated spin transfer torque: the reactive torque exerted by an electron on the wall as the wall exerts a torque on the electron[12]. For stability purposes, perpendicular-to-the-plane domains are preferred, forming Bloch walls in the absence of any in-plane (IP) field[13]. For sufficiently strong IP field, however, the wall formation changes to Néel walls[14], which are affected by spin-orbit torques, i.e. those from electron migration due to the spin Hall effect, leading to much faster and more efficient domain wall motion[15, 16]. With the discovery of the Dzyaloshinskii-Moriya interaction (DMI) at the interface between a ferromagnet and a material with high spin-orbit coupling, the possibility arose for Néel wall stabilisation without the need for an applied IP field[17, 16]. This is due to the intrinsic effective IP field at domain walls, effected by the lowering of the energy of orthogonal spin states in the ferromagnet as a consequence of the DMI. Thus, the study of the DMI is not only fascinating from a pure physics perspective, but may also lead to the feasibility of such devices as racetrack memory.

The net interfacial DMI is a key ingredient in determining the equilibrium domain wall (DW) spin structure in thin films with perpendicular magnetic anisotropy and structural inversion asymmetry, such as Pt/Co/AlO_x, Pt/Co/Ir, Pt/[Co/Ni] etc. The DW spin structure in turn determines how the DW responds to driving forces. In the presence of DMI, for example, reverse domains expand asymmetrically in simultaneously applied in-plane and out-of-plane fields[18, 2, 19, 15, 20], which provides one method of evaluation of the DMI and of the DW spin structure; the main method used in this thesis. Alongside effects such as DW velocities of several hundred metres per second from spin-orbit torque and Néel wall stabilisation, beyond a critical value of DMI when the DW energy goes negative, skyrmions may be stabilised [21] and could have a huge impact on magnetic memory [11, 10] and logic devices[22, 23].

Previously it has been shown that even nominally symmetric Pt/Co/Pt possesses a net DMI[18, 2, 24, 25], with room-temperature sputtered Pt/Co/Pt on silicon exhibiting asymmetrically expanding domains under an applied in-plane field. However, if grown epitaxially on sapphire, the domain expansion can be symmetric, indicating no net DMI, or even exhibit reversed asymmetry. This highlights the importance of structure and relative interface morphology of the upper and lower Co interfaces in determining the net DMI. Since DMI originates at the interfaces in these systems, the contributions from each must differ in magnitude or sign to effect a net DMI, and it is these that are investigated and discussed in this thesis.

1.1 Thesis overview

This thesis begins with a review of literature in four key areas related to the subsequent chapters. These are: the growth and characterisation of Pt/Co/Pt thin films; magnetic domain wall motion, specifically that in the creep regime; the Dzyaloshinskii-Moriya interaction; and perpendicular exchange bias brought about at the interface between a ferromagnet and an antiferromagnet. Theoretical work needed for the understanding of these areas, techniques used and results seen is provided alongside the review

and in the subsequent methods chapter, covering X-ray reflectometry, the magneto-optical Kerr effect, magnetostatics, spin torques and domain wall motion. A methods chapter follows the review outlining the procedures used to grow samples, characterise them and extract the DMI field.

There are three experimental chapters constituting the bulk of the work done in this project. The first is on results from the growth and characterisation of the Pt/Co/Pt samples, focusing on their interfacial structure and how that relates to their magnetic properties. The second looks at the measured DMI fields and how they correspond to the structural and magnetic data found in the first experimental chapter. The third experimental chapter concerns Pt/Co/IrMn samples, their characterisation and DMI measurement. These samples differ from those in the previous two chapters, not only in their far more pronounced structural inversion asymmetry, but also in their manifestation of an exchange bias when the IrMn layer is thick enough. The thesis finishes with concluding statements summarising the key points.

Chapter 2

Literature review

In this chapter, I discuss various key papers on topics pertinent to this thesis, namely the growth of Pt/Co structures, domain wall creep, the Dzyaloshinskii-Moriya interaction and perpendicular exchange bias. Each section follows a topic from its rise to popularity in the field of condensed matter through to the most recent understanding. In this review, it is seen that much work has been carried out using Pt/Co structures. As well as their fairly close lattice parameters, their tendency towards high perpendicular magnetic anisotropy when the Pt has a (111) orientation is a highly desirable feature for study and use in applications. The current understanding is that this is due to hybridisation of the Pt 5d-Co 3d electron orbitals, with its strength due in part to the high spin-orbit coupling of the Pt. High quality polycrystalline stacks have been readily made by sputtering, displaying a (111) texture in the Pt, with the fcc structure of thin Co becoming hcp at larger thicknesses. Epitaxial structures of Pt/Co have also been sputtered at elevated, allowing study of systems closer to model than polycrystalline, however they have been used in few studies thus far. Mathet et al.[26] produced a study of epitaxial Pt/Co and how they vary structurally and magnetically with Co thickness at two deposition temperatures. Besides the surface of the Pt buffer layer, however, the disorder at the interfaces was neglected. Also, whilst there is seen a difference in surface roughness between the two deposition temperatures used, this was not taken further to

use deposition temperature as a means of affecting the interfacial disorder. It is this gap that this thesis fills.

The motion of domain walls (DWs) under a driving force can be a most useful tool for ascertaining structural and magnetic properties of a sample, as well as a method for realising applications. Thus, it has been much studied in various systems and is now fairly well understood for simple set-ups. The driving force can either be from a magnetic field directly influencing the magnetisation of the sample, or from a spin-polarised current. A current travelling through a magnetic material experiences different resistances for each spin component, causing it to become spin polarised. As the electrons pass a DW, they are rotated to the orientation of the new domain, exerting an equal moment on the magnetisation of the DW. Currents flowing through a metal with high spin-orbit coupling obtain a transverse spin polarisation from the spin Hall effect and the Rashba field. If next to a magnetic material, a spin current can pass into it and rotate its magnetisation, causing DW motion. Under a relatively high driving force, DWs will move at a speed which varies linearly with force up until the Walker breakdown. At this point, the driving force is sufficient to disturb the structure of the DW, causing it to oscillate and so to lose speed. At higher driving forces, the speed is once more linear with force, though at a lower gradient. At relatively low driving forces, DW pinning comes into effect, transitioning from a flow to a creep regime where the DW moves by thermally-activated jumps between pinning sites. For small driving forces parallel with the domains, DW motion has been very successfully modelled, and it is this model, though modified, which shall be used to analyse the DW motion in this thesis.

The gaps in our knowledge of DW motion appear when a further magnetic field is added parallel to the direction of travel. This field modifies the DW energy density, and so affects the speed at which the DWs travel. It also breaks the symmetry of the system, allowing the effects of the Dzyaloshinskii-Moriya interaction (DMI) to be seen. This interaction occurs at the interface between a ferromagnet and a material with high spin orbit coupling (SOC), such as Co/Pt. One atom in the ferromagnet interacts with another via hybridisation of electron orbitals with the intermediary

high-SOC atom. This has the effect of lowering the energy of the orthogonal spin state of the two atoms in the ferromagnet which, at a DW between perpendicular-to-the-plane domains, favours a rotation of the magnetisation about an axis along the length of the DW. Due to the stray field produced by such a configuration, a magnetic field along the DW width will either increase or decrease the DW energy, modifying its velocity in an asymmetrical fashion. Several models have been proposed to account for the behaviour of DWs in the presence of an in-plane (IP) field and DMI, but as yet none can fully account for all the features seen. Being close to the model system, epitaxial samples are most likely to clarify the current understanding, and so it is against the DW motion seen for such epitaxial Pt/Co in this thesis that these models are tested. Furthermore, there has been some study into the effect of structure upon the magnitude and sign of the DMI contribution. It has been seen that these depend upon the materials used and upon the general disorder of the sample, however, no studies look directly at how the disorder of the interface affects the DMI contribution. It is this void of knowledge which this thesis focusses upon filling.

Finally, the exchange bias seen in structures of ferromagnet and antiferromagnet is looked at. This phenomenon is due to disorder in the structure leaving some antiferromagnetic atoms uncompensated at the interface. Below the blocking temperature, the magnetisation of these atoms can either rotate with the ferromagnet, increasing coercivity, or is pinned in its direction leading to exchange biasing. Exchange biasing has been much studied for its role as a symmetry breaker in magnetisation switching, allowing deterministic switching of the magnetisation of a ferromagnetic layer via the application of current without an externally-applied magnetic field. Its links to coercivity and anisotropy have also been explored, but thus far work is lacking on its effect on the DMI. This thesis goes some way towards remedying this.

2.1 Pt/Co structures

Cobalt and platinum have been of interest to the magnetism community for several decades, specifically as an alloy[27, 28, 29], but gained significant popularity when, in 1988, Carcia et al.[30] found perpendicular magnetic anisotropy (PMA) in thin film multilayers of Pt/Co. This PMA had an inverse dependence upon Co thickness and so their explanation of such is one given by Néel in his 1954 paper[31] on interface anisotropies, although the specifics are left uncertain. Once the potential for applications was suggested by Zeper et al.[32], that of magneto-optical recording, research on the system grew considerably. The system was a prime candidate for such an application, not only due to the PMA, but also because of its enhanced Kerr effect. In 1991, Lin et al. published some key work on superlattices of Pt/Co, varying not only the layer thicknesses and repeats, but also the crystal orientation[33], following on from den Broeder et al.'s work on Co/Pd[34]. They showed that the anisotropy and coercivity of the samples are more dependent upon the Co thickness than the Pt and, more crucially, that the anisotropy was severely affected by the crystallographic orientation, exhibiting PMA for Pt (111) and strong in-plane anisotropy for Pt (110). This indicated that the anisotropy was magnetocrystalline in origin. The transmission electron microscopy (TEM) scans shown in Fig. 2.1 emphasise the benefits of a Pt seed layer, particularly for evaporation deposition, and confirm the orientation of the crystals.

Around this time, Bruno[35] published a theoretical work on the connection between magnetocrystalline anisotropy and orbital moment in itinerant ferromagnets. The method was perturbative and used assumptions that led to quantitative estimates being accurate only to an order of magnitude, but a close connection was still seen between the two quantities. It is this link which is vital to the understanding of how PMA can exist in thin magnetic layers.

One of the earliest papers on Pt/Co systems grown by DC-magnetron sputtering, as they are in this thesis, was in 1993 by Carcia et al.[36]. Various gases were used to sputter at several working pressures, and high resolution

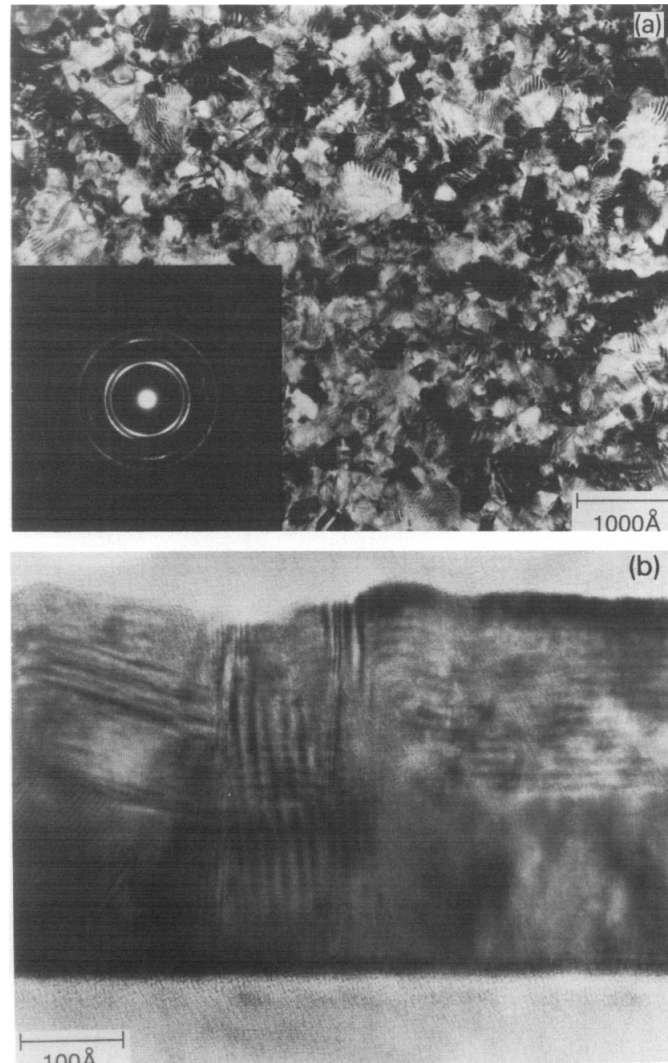


Figure 2.1: (a) Plane-view transmission electron microscopy (TEM) micrograph and diffraction pattern and (b) cross-section TEM micrograph of a $[\text{Co}(3.1 \text{ \AA})/\text{Pt}(10.2 \text{ \AA})]_{15}$ multilayer grown on 20 nm (111) textured Pt underlayer. Taken from Lin et al.'s paper[33].

electron microscopy carried out on them. It was seen that sputtering using gases with higher masses, using a ZnO seed layer or sputter-etching the substrate surface led to the promotion of a (111) texture, and so a higher PMA. Since sputtering is a far more efficient method of deposition than those used previously, this made the system a viable candidate for industrial applications. Sputtering on ZnO with a heavy gas or at a high pressure, however, gave rise to a columnar growth, pinning domain walls and increasing the coercivity[36], which is not desirable for applications where smooth domain wall motion is needed.

Further key structural analysis was carried out in work by Ferrer et al.[37] in 1997. In their paper, X-ray diffraction was employed during growth of Pt/Co, with the Co layer ranging between 2 and 12 atomic layers onto Pt (111). The Co was seen to grow layer by layer, though with the previous two layers completing whilst the next is grown. The lateral spacing of the Co atoms appeared to be that of bulk Co, but with an interplanar distance expanded by 3%; and the overall structure is that of fcc up to about 12 atomic layers, after which hcp dominates. Thin (<12 atomic layers) Co was made hcp by annealing at about 450K, with alloying at the interface beginning at about 550K. Tuning to the L_3 absorption edge of Pt showed it to be magnetised mostly in the layer closest to the interface, with the next layer exhibiting this proximity effect an order of magnitude smaller. The Pt magnetisation was seen to increase 25% after transforming the Co to hcp, though the explanation for such an effect was left for further study.

These results are complemented by Lundgren et al.[38] who used scanning tunnelling microscopy to assess the growth of Co on Pt (111), shown in Fig. 2.2. They found that the first layer of the Co grew on the lattice sites of the Pt, with the resulting strain causing dislocations across the layer. These were thought to assist the initial layer by layer growth by acting as sites of interlayer diffusion, allowing atoms to fill the previous layer instead of clumping together in more 3D structures. The second layer, however, was able to grow with bulk Co lattice spacings, leading to the formation of a hexagonal Moiré structure with areas of hcp Co forming above the dislocations, though the majority of the Co remained in fcc formation, agreeing

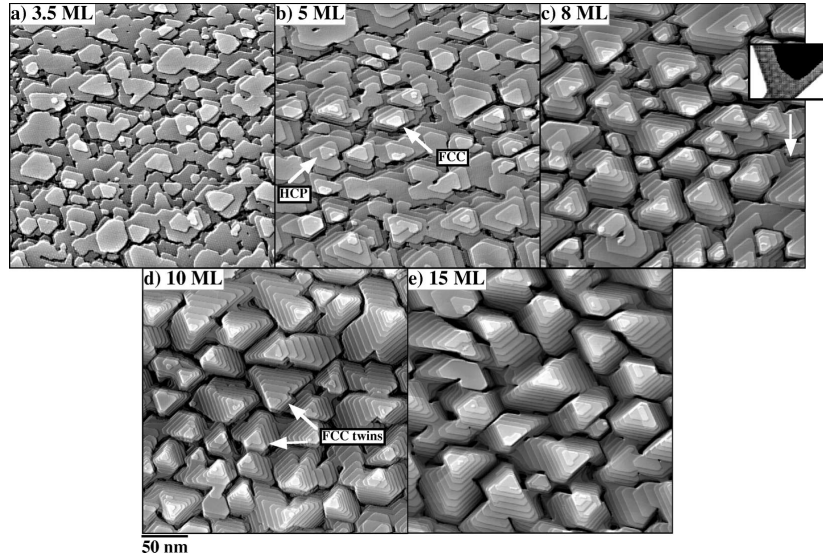


Figure 2.2: STM images showing the development of the growth and morphology of thin Co films on Pt(111). (a) STM image of a 3.5 ML thick Co film. (b) STM image of a 5 ML thick Co film. The arrows indicates islands with fcc and hcp Co stacking. (c) STM image of an 8 ML thick Co film. The inset shows an STM image demonstrating the Moiré structure observable in the valleys between the islands. (d) STM image of a 10 ML thick Co film. The arrows indicates the existence of fcc twins. (e) STM image of a 15 ML thick Co film. Taken from Lundgren et al.’s paper[38].

with Ferrer et al.’s findings. The Moiré structure continues up to five monolayers of Co, though at about 3.5 monolayers the Co starts grouping into triangular-shaped islands. The formation of these islands is suggested to detract from the smoothness of the upper Co/Pt interface and so lead to decreased interfacial anisotropy, reducing the PMA. They also put forth the suggestion that the Moiré modulation of the interplanar spacings seen at low Co coverage may contribute towards the change in PMA as well. Such work allows the tuning of the crystal structure via Co thickness and annealing temperature.

The later structural characterisation by Lundgren et al. follows an investigation in 1998 of the origin of PMA in Pt/Co by Nakajima et al.[39]. This

study used magnetic circular X-ray dichroism (MCXD), allowing energy-specific, and therefore element-orbital-specific, probing of the structure. They found a persistence of Pt $N_{6,7}$ and $O_{2,3}$ edge signals, indicating Pt 5d-Co 3d hybridisation at all Co thicknesses studied. The intensities of these signals decreased with a thicker Co layer, indicating that this hybridisation is localised at the Pt/Co interface. The hybridisation has the effect of enhancing the orbital magnetisation of the Co and effecting a magnetisation in the interfacial Pt, ultimately leading to PMA as explained using the earlier, theoretical work by Bruno[35]. Nakajima et al.[39] saw the orbital magnetisation enhancement diminish with Co layer thickness until about 6-8 monolayers, after which it increased again by a slight amount. The decrease is in line with the diminishing relative contribution of interface effects with increased Co layer thickness. They ascribed the increase at thicker Co layers to a structural change from fcc Co to hcp Co, a conclusion backed up by a kink in the Kerr rotation angle with Co thickness data at about 6-8 monolayers. Finally, values of orbital magnetic moment for bulk Co in hcp and fcc formations were measured, for the first time in the case of fcc Co.

Further key work on Pt/Co/Pt structures grown by Ar sputter deposition was carried out by Mathet et al.[26] in 2003. Structural investigation of the Pt seed layer showed that 4 nm of growth on an Al_2O_3 (0001) substrate below $650^\circ C$ gave a continuous layer with a smooth surface. Reflection high-energy electron diffraction (RHEED) showed such a layer to have an epitaxial nature akin to those obtained through ultra-high vacuum growth. A thickness of 4 nm was found to exhibit the smoothest surface, through atomic force microscopy (AFM), with root-mean-square roughness, island peak to valley roughness and lateral island width increasing with thickness, thus 4 nm was used henceforth in the paper. Depositing Co/Pt on top of the buffer layer, Mathet et al. found that spontaneous Co Pt intermixing occurred at substrate temperatures exceeding $300^\circ C$, and so all depositions were carried out at or below that. At $300^\circ C$, there is little change found structurally between a structure with 0.5 nm and 1.8 nm of Co, with scanning tunnelling microscopy (STM) images resembling the AFM images of 15 nm of Pt in terms of island size and roughness. The X-ray diffraction (XRD)

data showed the substrate peak and a peak for Pt, modulated by Kiessig fringes, yet without a Co peak, as expected due to the low X-ray scattering of Co and amount of Co material. Grain size analysis showed the grains to be as large as the layers are thick, indicating a continuous perpendicular grain. This structural characterisation shows that it is possible to grow epitaxial samples of Pt/Co/Pt with well-ordered interfaces via sputtering at elevated temperatures, a vital finding for the growth of samples in this thesis.

Comparison between hysteresis loops of Mathet et al.'s Pt/Co/Pt samples with the Pt/Co grown at 150°C and 300°C showed a lower coercivity in the former, Fig. 2.3 (c), which Mathet et al. attribute to a lower magneto-crystalline anisotropy. A rounding of the loop was seen in the former, indicating a higher density of pinning sites relevant to domain wall motion, and a reduced remanence compared to saturation magnetisation which shows there are some areas of the sample thick enough for the shape anisotropy to diminish the PMA. These observations led Mathet et al. to focus on samples grown at 300°C. Varying the thickness of the Co layer, the easy axis is seen in Fig. 2.3 to switch from out-of-plane (OOP) to in-plane (IP) as the thickness increases between 1.8 nm and 2.2 nm, indicating that this is the point at which the shape anisotropy of the sample overcomes the magneto-crystalline contribution from the interfaces. As a comparison, they found that samples grown at room temperature on an amorphous substrate have this critical point at around 1.6 nm which they attribute to less ordered interfaces. Delays were seen via magneto-optical microscopy in magnetisation relaxation curves which showed that the main mechanism for magnetisation switching is through domain wall propagation. This technique also allowed analysis of the Barkhausen activation length, which is seen to be much greater than the grain sizes, showing strong exchange interaction between grains and that a small fraction of grain boundaries contribute to domain wall pinning with an applied field in the region of the propagation threshold. These findings show how promising Pt/Co/Pt is as a structure in which to assess magnetisation dynamics and interactions, as well as a material system to be used in applications due to the ease of applying such growth conditions on an

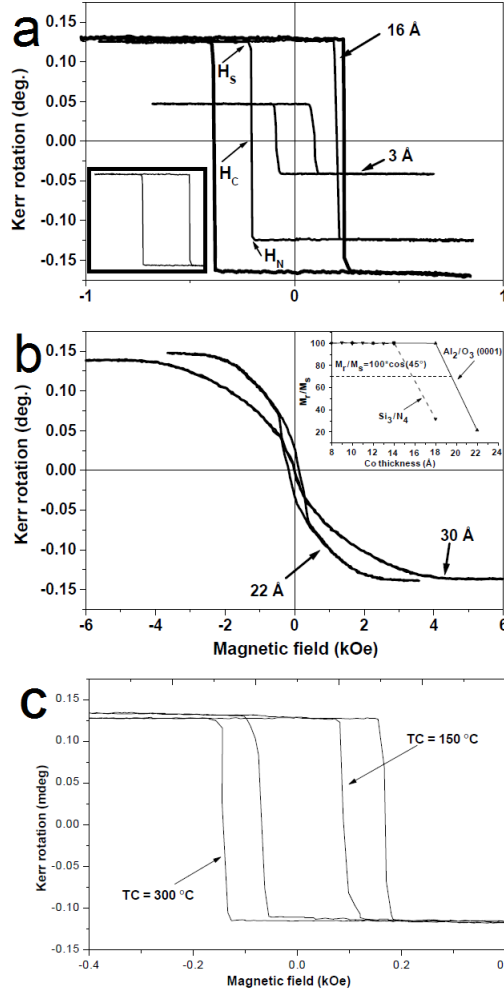


Figure 2.3: Evolution of Pt/Co/Pt hysteresis loops with the Co layer thickness. The Co growth temperature is 300°C : (a) $t_{\text{Co}} < t^*$ (the critical thickness between in-plane and out-of-plane easy-axis magnetisation), the inset corresponds to the Faraday ellipticity of a Pt/Co(5 Å)/Pt structure measured at 2K; the coercive field is about 200 Oe, the Faraday ellipticity amplitude is 0.3° (b) $t_{\text{Co}} > t^*$, the inset corresponds to the remanent magnetization ratio with the Co layer thickness in the case of Pt/Co/Pt trilayers sputtered on sapphire (solid line) or Si_3N_4 (dash line) substrates. (c) a comparison of two temperatures of Co deposition, measured at room temperature. Taken from Mathet et al.'s paper[26].

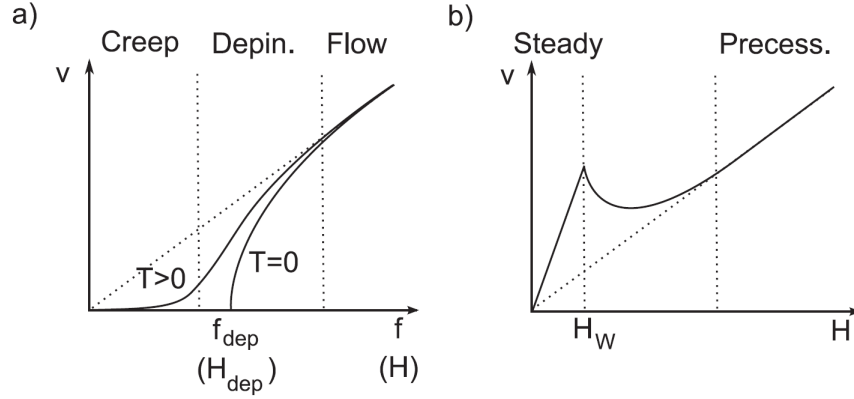


Figure 2.4: (a) Theoretical variation of the velocity, v , of a 1D interface (domain wall) in a 2D weakly disordered medium submitted to a driving force, f (magnetic field, H), at zero and finite temperature, T . The creep, depinning, and flow regimes are labelled. (b) Regimes of domain-wall flow motion in an ideal ferromagnetic film without pinning. The steady and precessional linear flow regimes are separated by an intermediate regime which begins at the Walker field, H_W . Taken from Metaxas et al.'s paper[40].

industrial scale.

2.2 Domain wall creep

2.2.1 Theory

Domain walls move with different mechanisms depending upon the driving force applied. The creep regime is an area in velocity-space, shown in Fig. 2.4, in which domain walls move by jumping between pinning sites, giving the overall appearance of creeping forward. This relies upon thermal fluctuations to raise the wall's energy beyond the pinning site's. It requires a lower applied magnetic field than the depinning regime where the walls are far less affected by pinning, or the flow regime where continuous motion is completely uninterrupted by pinning sites[40] and their velocity depends linearly on the driving force. Creep motion is partially statistical and relies upon thermal jumps between pinning sites, such as that shown in Fig. 2.5.

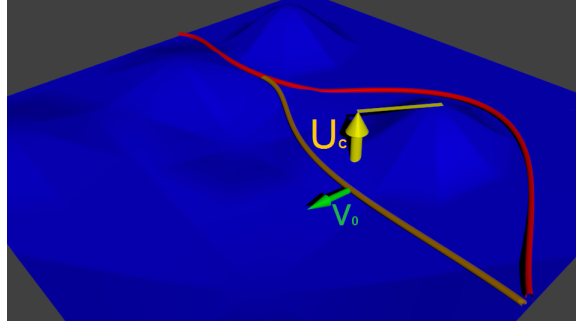


Figure 2.5: A graphic representation of the potential energy landscape in a magnetic thin film. The red line represents the domain wall; the orange line, that of the domain wall after it has overcome a pinning site. The pinning potential, U_c , and the characteristic velocity, v_0 , are shown as yellow and green arrows, respectively.

The velocity can therefore be modelled by[40]:

$$v = v_0 \exp[-(T_{\text{depin}}/T)(H_{\text{depin}}/H)^\mu] \quad (2.1)$$

where T_{depin} , the depinning temperature, is given by U_c/k_B with U_c being the height of the pinning energy barrier and k_B being Boltzmann's constant. H_{depin} is the depinning field, v_0 is a numerical prefactor referred to hereafter as the characteristic velocity and μ is a dynamical exponent taken to be $1/4$ for a 1D structure moving in a weakly disordered medium.

In the flow regime, if the driving field is increased beyond a critical point, the Walker breakdown field, the domain wall no longer remains stable but instead transitions into a precessional regime[40], as shown in Fig. 2.4 (b). Once fully in the precessional regime, the velocity once more increases linearly with driving field, but at a lesser rate than in the steady state regime.

Domain wall energy variation

To be able to successfully model our systems, we find that we must modify the creep equation to take into account changing T_{depin} and H_{depin} . These

changes can be linked to the changes in domain wall energy density, ϵ , like so[18]:

$$v = v_0 \exp[\zeta(\mu_0 H_z)^{-1/4}], \quad (2.2)$$

where the exponent scaling factor

$$\zeta = \zeta_0[\epsilon(H_x)/\epsilon(0)]^{1/4}.$$

Here v_0 is the characteristic velocity, ζ_0 is a scaling constant, and for a mixed Bloch-Néel wall configuration:

$$\epsilon = \epsilon_0 - \frac{\pi^2 \delta \mu_0^2 M_s^2}{8K_D} (H_x + H_{DMI})^2. \quad (2.3)$$

For purely Néel:

$$\epsilon = \epsilon_0 + 2K_D \delta - \pi \delta \mu_0 M_s |H_x + H_{DMI}|, \quad (2.4)$$

where the pure Bloch wall energy density $\epsilon_0 = 2\pi\sqrt{AK_0}$ where A is the exchange constant and K_0 is the effective anisotropy, used as a fitting parameter; $\delta = \sqrt{A/K_0}$ is the domain wall width; M_s is the saturation magnetization; $K_D = (N_x \mu_0 M_s^2)/2$ where the demagnetizing factor $N_x = t * \ln(2)/(\pi\delta)$ with t the thickness of the ferromagnetic film.

2.2.2 Spin torques theory

Whilst it is relatively simple to move a domain wall by applying an external magnetic field to propagate one or other domain, it can be advantageous to instead use electrical currents since these can be more easily directed, can require less power and do not need a moving read/write head[10]. The first means of moving a domain wall using a current came from spin transfer torque (STT)[41], which involves an electron's spin being rotated by the domain wall as it passes through it. Since a torque is exerted on the electron, an equal and opposite torque is exerted on the spins in the domain wall, shifting them slightly. The combined effect is that the domain wall moves

in the direction of the electron flow.

As heterostructures became more widely studied, particularly those with ferromagnetic layers on top of heavy metals, other effects were seen due to spin-orbit torques[42]. As the current flows through the heavy metal, the high spin-orbit coupling induces the spin Hall effect (SHE), causing a spin gradient across the layer. This causes electrons with a certain spin direction to migrate into the ferromagnet and exert a torque on its spins. At the domain wall, this effectively causes the wall to move. Similarly, at the interface between the two layers, the Rashba field causes an out-of-equilibrium spin polarisation which is misaligned from the magnetisation of a Bloch wall, effecting a torque[43]. Due to the geometry, the migrating spins from the SHE have no effect on Bloch walls perpendicular to the current direction, so the wall must be either Bloch-Néel, or purely Néel to be moved.

Hall effect

First discovered in 1879 by Edwin Hall[44], the Hall effect consists of the transverse movement of electrons under a longitudinal flow. Depending on the material and environment, this effect can have several driving forces and can lead to either charge or spin separation in the transverse direction. Charge separation can easily be detected by measuring the transverse voltage whereas spin separation often relies on the inverse effect to measure.

Ordinary Hall effect The original Hall effect, now known as the ordinary Hall effect, OHE, occurs in materials through which a current is flowing, under an applied magnetic field[44]. It has the consequence of shifting electrons to one side of the material, causing a charge imbalance and thus an electric field perpendicular to both the applied magnetic field and the current direction. This occurs due to the Lorentz force acting upon the electrons: as they move through a magnetic field, it is perceived as a perpendicular electric field in the electrons' rest frame, thus applying a transverse force to

the electrons. The Lorentz force is

$$F = q[E + (v_e \times B)] \quad (2.5)$$

where q is the charge of the electron, E is the electric field, v_e is the velocity of the electrons and B is the magnetic field through which the electrons move. In equilibrium, where the electric field from the charge imbalance balances the applied magnetic field, the electrons feel no net force and so

$$E_y = -v_{ex}B_z \quad (2.6)$$

where further subscripts indicate the component of the vector along the x, y or z axis. Taking $E_y = V_{\text{Hall}}/w$ and the current $I_x = qntwv_{ex}$ where w is the width of the material through which the electron is moving, t is its thickness and n is the charge carrier density, one finds the Hall voltage, V_{Hall} to be given by:

$$V_{\text{Hall}} = I_x B_z / (nte) = I_x B_z R_{\text{Hall}} / t \quad (2.7)$$

where $R_{\text{Hall}} = 1/(ne)$ is the Hall coefficient. Thus the Hall voltage depends linearly upon the applied current and magnetic field, as expected from physical arguments, but also inversely upon the areal charge density in the plane perpendicular to the magnetic field. This last relation can be explained by a decrease in magnetic field density per charge as the areal charge density increases, thus decreasing the Hall effect[45].

Extraordinary Hall effect Also known as the anomalous Hall effect, the extraordinary Hall effect, EHE, is similar in outcome to the OHE, except that it occurs within a magnetic material without the need for an external magnetic field[46]. Its origins are not merely from the Lorentz force due to the inherent magnetisation, rather they are from both extrinsic and intrinsic sources. The extrinsic contribution comes from disorder in the material; as electrons approach a defect, they are pushed to one side of it in a mechanism known as skew scattering[47], emerging with a trajectory including a trans-

verse component. If two defects are present in close proximity, the electron can undergo side-jump scattering[48], wherein it is shifted towards one side yet continues onwards without a transverse component of its trajectory. The intrinsic source is that of Berry curvature from a changing Berry phase.

Spin Hall effect The spin Hall effect occurs in materials with high spin-orbit coupling, typically heavy elements, and requires no external magnetic field or internal magnetisation[49]. Its effects are to separate electrons of differing spin, giving each a different transverse velocity. This leads to a spin gradient in the directions perpendicular to the current.

Rashba field

Alongside the Hall effect, there is also a contribution to the spin current from the Rashba field[43]. This is the effective field felt by moving electrons due to the interfacial electric field. On a more detailed level, the structural inversion asymmetry at the interface leads to this interfacial electric field, as well as to a band gap between the orbital normal to the interface and those parallel with it. By breaking the symmetry at the interface, hybridisation may also occur between these orbitals, allowing itinerant electrons to hop between them.

The Rashba field affects the electrons, analogous to the Magnus effect, altering their trajectory depending on their spin orientation[43]. At the interface between a heavy metal and a ferromagnet, the Rashba field generates a spin current out of the heavy metal, where the largest spin-orbit interaction takes place, into the ferromagnetic layer, applying a torque on the spins there and moving the domain wall. The outcome of this effect, then, is similar to the spin Hall effect and so has caused much debate over which contributes the most, though it seems that this depends much on the system studied[50].

2.2.3 Review

The theory behind creep motion, that of travel via jumping from pinning site to pinning site, was expounded upon in a 2000 paper by Chauve et al.[51]. In their paper, they improved upon previous investigations of the functional-renormalisation group approach to elastic systems in disordered media by averaging around disorder instead of expanding around an unknown mean-field solution, and thus improving accuracy, as well as taking an approach which proves the scaling relations instead of assuming them. These allowed accurate analysis of the dynamics and the derivation of the creep law, Eq. 2.1 shown in Section 2.2.1: a vital equation for the analysis of domain wall motion in low applied driving forces. The law had been previously proposed qualitatively, but not with the theory for deriving the prefactor and exponent as is done in by Chauve et al.. Their paper was also the first to propose the depinning regime as a regime between creep and flow. The theoretical work done by Chauve et al. underpins much of the analysis used in subsequent experimental papers and in this thesis.

Two years before Chauve et al.'s paper was released, Lemerle et al.[52] produced experimental work on creep in polycrystalline Pt/Co/Pt, analysed using a less rigorous derivation of the creep law akin to that of Blatter et al.[53]. Lemerle et al.'s paper was a key contribution to the creep law as it was the first direct measurement of the creep regime for a moving interface in a disordered medium. The method used to accomplish this is through polar magneto-optical Kerr effect microscopy, in which a nucleated domain is propagated via a field pulse and its displacement measured to determine its average velocity. Upon analysis of the velocity under various applied field strengths, the scaling factor for the average energy barrier and the exponent of the correlation function along the magnetic domain wall was extracted. They found that the values obtained for these two parameters agree well with those predicted by the theory they derived and theory from other literature[54], respectively. This showed that, up to the 200 mT fields they applied, domain wall motion in high quality Pt/Co/Pt is governed by the creep law.

This analysis was extended by Metaxas et al.[40] in 2007 to look at magnetic domain wall behaviour in the transition between creep and flow regimes, illustrated in Fig. 2.4. Again, polycrystalline Pt/Co/Pt was used, grown at elevated substrate temperatures with various thicknesses of Co. Measurements using the polar magneto-optical Kerr effect allowed the extraction of domain wall velocity, as well as coercive field, saturation magnetisation and effective anisotropy through the varying of applied field, and Curie temperature via the application of heat. Although the strength of the applied field had the same range as for Lemerle et al.[52], Metaxas et al. were able to see the full transition to the flow regime, possibly due to the samples being grown at elevated temperatures with a thinner Pt seed layer. This enabled extraction of the maximum field at which the creep law was still valid and the wall mobility for high fields, and from this the damping parameter and Walker fields for the steady state and precessional state. They discussed the lack of an observed Walker field and provided the explanation that it occurs below the field needed for flow, meaning that all of the flow is in the precessional regime. They also conceded some inaccuracies in their extracted values, especially the damping parameter, which they found could not be confirmed via ferromagnetic resonance due to excessively broad linewidths. Nevertheless, this is a key paper in establishing the dynamics of magnetic domain wall motion in its various regimes and provides evidence in support of the theory of earlier work.

Work on Pt/Co/Pt domain wall dynamics slightly spatially closer to this thesis appeared in 2013 in the form of a paper from the University of Leeds Condensed Matter group, along with the University of Glasgow, by Mihai et al.[55]. The samples used in this work were epitaxial Pt/Co/Pt grown in the machines used in this project, and so this paper has been of great assistance for guidance during the early stages of growth and characterisation. Beyond the initial structural and magnetic characterisation, however, Mihai et al. used Kerr microscopy to look at the depinning energy of magnetic domain walls, and how it changed with substrate temperature during deposition. They found that the trend of depinning energy with deposition temperature follows well the trend of coercivity with deposition temperature, see Fig.

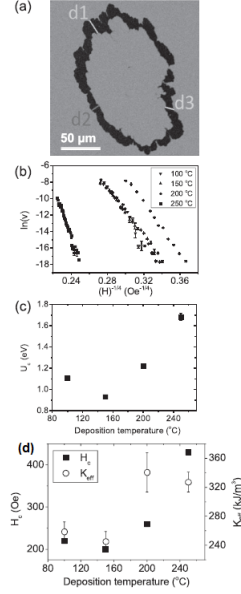


Figure 2.6: (a) Wide-field Kerr microscope image of a DW displacement. The black region denotes the area covered by the DW during the field pulse. Displacements were measured at three locations (d1, d2, and d3) on each image, averaged and plotted as a function of pulse duration to obtain the DW velocity. (b) Natural logarithm of DW velocity, $\ln(v)$, as a function of applied field H raised to the power $-1/4$, for Pt(3.0 nm)/[Co(0.5nm)/Pt(1.0nm)]₂ with the upper Co/Pt layers deposited at various substrate temperatures. (c) Pinning energy U_c as a function of the substrate temperature during growth of the Co/Pt. (d) Coercivity H_c (filled squares) and effective perpendicular anisotropy constant K_{eff} (open circles) of Pt(3.0 nm)/[Co(0.5 nm)/Pt(1.0 nm)]₂. The upper Co/Pt layers were deposited at substrate temperatures in the range of 100-250°C. Taken from Mihai et al.'s paper[55].

2.6, and saw that for lower temperature growth there was faster magnetic domain wall motion with fewer nucleation sites. This was attributed to more ordered samples with sharper interfaces than at the higher temperatures. It was also seen that velocities were 2-3 times larger than in polycrystalline samples under the same driving force suggesting an improved domain wall creep velocity in highly-ordered epitaxial samples.

Continuing with the theme of temperature dependence, Gorchon et al. investigated how the temperature of the sample at the time of measurement affected the creep and flow[56]. Polycrystalline Pt/Co/Pt was used with the velocity being found in the same manner as with the previous papers. Performing linear fits of the velocity, v , against applied field, H , for $\ln(v)$ vs $H^{1/4}$, $\ln(v)$ vs H and v vs H , as shown in Fig. 2.7, they were able to extract fitting parameters for the creep, thermally assisted flux flow and depinning (flow) regimes respectively. They found the logarithm of the characteristic velocity in the creep regime to depend linearly upon temperature and so deemed it to be composed of a combination of the disorder correlation length and the attempt frequency at passing barriers. The disorder correlation length was found to be approximately equal to the lateral size of Pt crystals, indicating that most pinning occurs at crystal boundaries, taken to be a temperature-independent mechanism. Using the extracted parameters, they calculated the elastic energy density and pinning energy density of the magnetic domain wall, finding the former to be more influenced by temperature than the latter. Overall, by looking at the change with temperature of the magnetic domain wall motion, the mechanisms behind the parameters used in theory were better understood.

More recently, in 2016, Jeudy et al. published a paper describing an empirically-derived creep law capable of describing a wide range of material systems[57]. This new law differs from the standard creep law by an offset of -1 to the $(H/H_{\text{dep}})^{-\mu}$ term, where H is the applied field driving the movement, H_{dep} is the field needed to depin the domain wall and μ is the creep exponent taken to be 1/4. The inclusion of this offset causes the energy barrier to tend towards zero when the applied field approaches the depinning field, and towards the conventional creep law energy barrier term when the

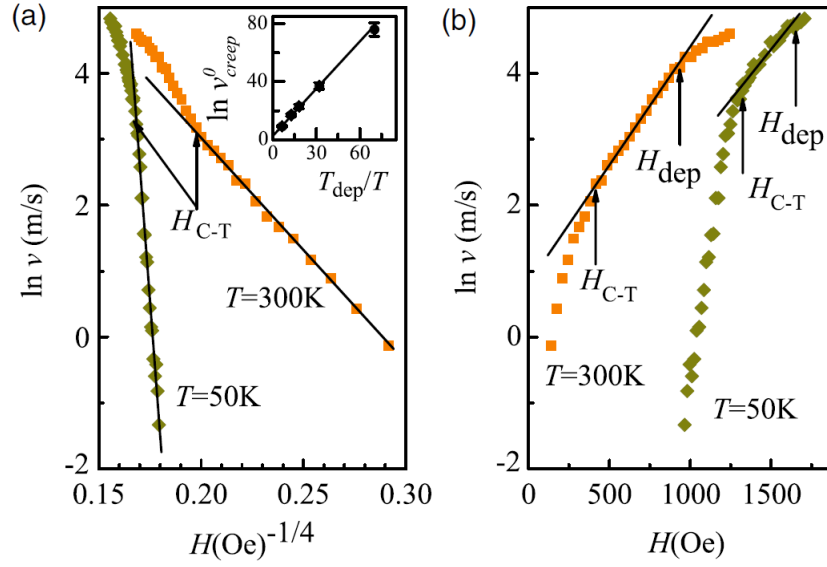


Figure 2.7: Field-dependent, H , domain wall velocity, v . (a) Plot of $\ln v$ vs $H^{1/4}$ to evidence the creep regime and its upper boundary H_{C-T} (creep). Inset: creep prefactor v_{creep}^0 deduced from an extrapolation of the creep law (straight line) to $H^{1/4} = 0$. (b) Plot of $\ln v$ vs H reveals the thermally assisted flux flow (TAFF) regime and its two boundaries H_{C-T} (TAFF) and H_{dep} (TAFF). Taken from Gorchon et al.'s paper[56].

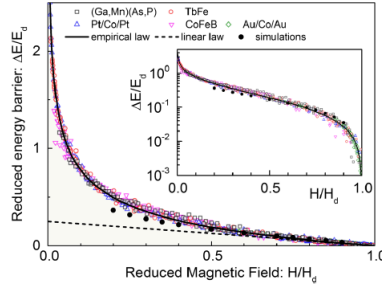


Figure 2.8: Universal energy barrier of the creep regime. The variation of the reduced energy barrier height $E=E_d$, with $E_d = k_B T_d$, where T_d is the depinning temperature and k_B is Boltzmann's constant, is reported as a function of the reduced field $H=H_d$, where H_d is the depinning field, for five different magnetic materials and for temperatures ranging from 10 K to 315 K (25 curves are superimposed). The solid line is a plot of Jeudy et al's model. The black circles correspond to the predictions of Kolton et al[58] whose energy scale was adjusted to experimental data. The dashed line corresponds to the linear variation of the energy barrier close to the depinning field ($H = H_d$). Inset: Universal barrier presented in semi-log scale showing a good quantitative agreement with Jeudy et al's model over more than 3 orders of magnitude. Taken from Jeudy et al.'s paper[57].

applied field is much smaller. This was the behaviour seen in extracted energy barrier terms for not only Pt/Co/Pt, but also for (Ga,Mn)(As,P), TbFe, CoFeB and Au/Co/Au systems, as in Fig. 2.8. Thus, this adjusted creep law can be used to describe all of the creep regime up to the depinning transition.

2.3 Dzyaloshinskii-Moriya interaction

2.3.1 Magnetic energy theory

The magnetic configuration of a structure is dependent upon several factors, with the lowest energy state for each spin being determined by nearby interaction with other spins via the exchange interaction, interaction with longer-range order via anisotropies, including shape anisotropy, and interaction with other spins via intermediaries as in the Dzyaloshinskii-Moriya

interaction. In the thin films studied here, the high interface to bulk ratio means that interactions at the interface are very important.

Exchange interaction

The exchange interaction is the main way in which spins directly influence each other and stems from energy differences resulting from electrons exchanging positions. Along with a high density of states at the fermi level, it is responsible for ferromagnetism. A simplified explanation is that electrons with parallel spins will have wave functions further apart due to the Pauli exclusion principle, which leads to a lower Coulomb interaction between the electrons and so a lower overall energy[59]. Likewise, if the exchange constant is negative, the system can settle into an antiferromagnetic ordering.

The sign and magnitude of the exchange constant for two spins, “a” and “b”, J_{ab} , is dependent on the exchange integral, J_{ex} , the Coulomb integral, C and the overlap integral, B , as such: $J_{ab} = (J_{ex} - CB^2)/(1 - B^4)$. The Coulomb integral represents the energy due to the Coulomb repulsion of the electrons, being of the same charge. The exchange integral has no physical analogy, appearing only for identical particles, and represents the energy difference were two electrons to exchange positions. The overlap integral is a dimensionless term representing the degree to which the wave functions of the electrons overlap. The exchange constant, in turn, determines the energy associated with the spins of two electrons via the Heisenberg exchange Hamiltonian: $H_{Heis} = -2J_{ab} < \vec{s}_a \cdot \vec{s}_b >$.

Dzyaloshinskii-Moriya interaction theory

A particularly important effect in this project is the Dzyaloshinskii-Moriya interaction (DMI). This is an example of an interaction between spins that relies upon an intermediary[60, 61]. Electrons from two ferromagnetic atoms hybridise with electrons in an atom with high spin-orbit coupling. This has the effect of lowering the energy of their orthogonal spin state[62]. For homogeneous films, unless the effect is strong enough to overcome the other energy terms and cause chiral magnetic structures, the contributions cancel

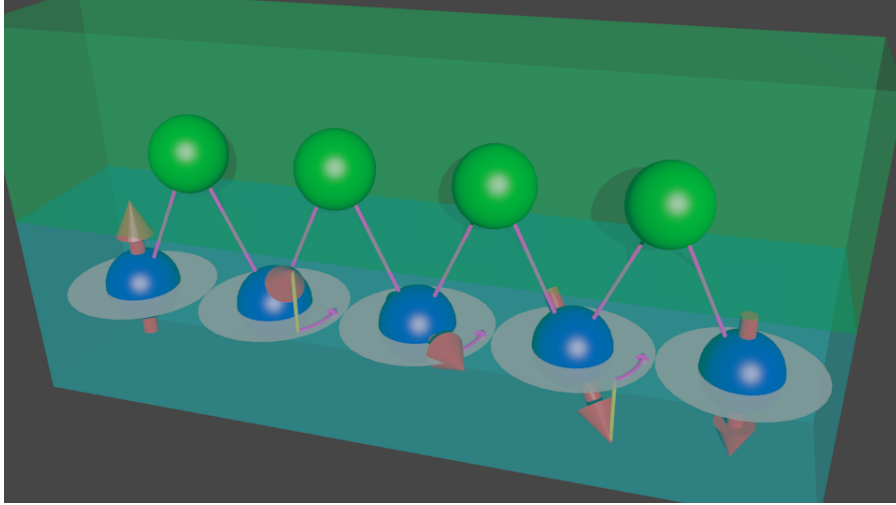


Figure 2.9: Representation of DMI on a Bloch-Néel DW. The ferromagnetic atoms (blue) interact via the atoms with high spin-orbit coupling (green). The interaction is highlighted as pink with the effecting torque as a pink arrow rotating the moments' (red) projection (yellow) onto the plane of free movement.

out and the net effect is zero. Therefore symmetry breaking is needed in the form of, say, a domain wall. At such a wall, there is a magnetisation gradient, breaking the symmetry and allowing rotation about the axis perpendicular to the plane of the film (Fig. 2.9). Due to stray field minimisation, moments tend to rotate about an axis parallel to the width of the DW, resulting in so called Bloch walls (Fig. 2.10 A,B). However, if the DMI is strong enough then the moments are rotated about an axis parallel to the DW length resulting in Néel walls (Fig. 2.10 C,D). In such a configuration, the stray field from the moments at the wall is not cancelled, leading to a net magnetic field parallel with the DW width; thus the effect of the DMI can be seen as a magnetic field aligning the spins in the DW, known as the effective DMI field, with a magnitude given by: $H_{\text{DMI}} = D/(\mu_0 M_s \delta)$ where D is the DMI strength, M_s is the saturation magnetisation and δ is the DW width[2]. In most systems, the DMI is not strong enough to entirely pull the moments into alignment, and so a mixed Bloch-Néel wall results.

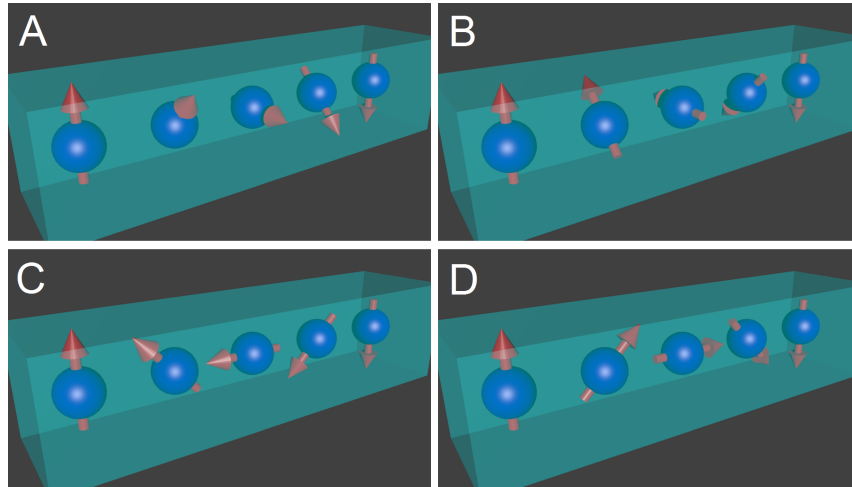


Figure 2.10: Representation of Bloch (A, B) and Néel (C, D) domain wall configurations. A and C are left-handed (anticlockwise); B and D are right-handed (clockwise)[64]. A useful mnemonic is to see the moments in a Bloch wall as blocking passage past them, and as those in a Néel wall as kneeling towards one or other domain.

Chirality Depending upon the atoms involved, the DMI strength can have differing magnitudes and signs. This leads to two possible chiralities associated with DWs with sufficiently high DMI contributions[67, 64], shown in Fig. 2.10. The two chiralities of a Bloch wall (Fig. 2.10 A and B) are degenerate in energy, since both minimise the stray field along an axis of symmetry. Néel walls that are due to DMI contributions with a positive (negative) DMI strength, D, and hence a positive (negative) effective DMI field have chiralities which are right-handed (left-handed)[63]. Since the DMI manifests itself as an effective field, it is worth noting that an applied field of sufficient strength can also set the DW chirality and configuration.

2.3.2 Review

One of the first papers to investigate experimentally the effects of the Dzyaloshinskii-Moriya interaction (DMI), and the first on Pt/Co structures, is that of Thiaville et al.[16] in 2012. Beginning with models of a static domain wall

(DW) to show that the transition between Bloch and Néel walls is gradual, they moved on to DW dynamics, a previously untouched area where DMI is concerned. Their simulations showed DMI stabilising the Néel wall structure against precession, and so increasing the Walker field, without changing the magnetic DW mobility. Using a model with just two parameters, the DW position and the DW magnetic moment angle, they derived an expression for the DW energy density of a Néel wall and showed that the model agrees well with numerical simulations. Looking at the experimental results of Miron et al.[65] and Metaxas et al.[40], Thiaville et al. noted a domain wall velocity in Pt/Co/AlO_x five times that of Pt/Co/Pt. They attributed this to a net DMI field at the domain walls, which is absent for Pt/Co/Pt, stabilising a Néel wall and so increasing the Walker field. This means that at the applied fields studied, the Pt/Co/AlO_x was still in the flow regime whilst the Pt/Co/Pt was in the slower precessional regime. They backed this up by applying an in-plane (IP) field to work with or against the DMI field and subsequently saw a shift in Walker field for the four IP fields applied. The authors also used the Néel wall-stabilising effect of the DMI to explain the large domain wall velocity under an applied current, allowing the DW to feel the effects of the spin Hall effect. They finally pointed out the usefulness of the intrinsic DMI field with regard to applications such as racetrack memory, due to the chirality allowing all walls to move in the same direction under an applied current. These findings were key to a lot of subsequent work and set the basis upon which further investigations of DMI on domain walls stand.

Emori et al. focussed their investigation onto current-driven DW propagation[17] with different seed layers. Initial comparisons to field-driven motion showed that the current assists field-driven motion in Ta/CoFe/MgO, but hinders field-driven motion in Pt/CoFe/MgO, with the same dynamical scaling shown by current- and field-driven motion across three decades of velocities, after scaling the current by a constant. This indicated that both methods of DW driving operate under the same mechanisms. By using a Hall cross setup with an applied longitudinal magnetic field, Emori et al. were able to extract the Slonczewski-like and field-like torques, attributed to the spin Hall effect and Rashba field, respectively. They found the former to

give values leading to spin Hall angles akin to literature in Pt/CoFe/MgO, but twice as large as literature in Ta/CoFe/MgO. The field-like torque was seen to be negligible in Pt/CoFe/MgO but larger than the Slonczewski-like torque in Ta/CoFe/MgO, although they felt that further investigation into such a large field-like torque was beyond the scope of their project. Focusing, thus, on Pt/CoFe/MgO, Emori et al. argued that observations of DW motion against the direction of electron flow were consistent only with a Néel wall structure, necessitating a stabilising DMI. They assessed the rigidity and chirality of the DW by showing the effect of an applied longitudinal and transverse field upon the DW velocity, finding resilience to change of the DW magnetisation up to the maximum available field of 600 Oe. Comparing their data to a 1D model, they found good qualitative agreement.

Current-induced domain wall motion was also investigated by Ryu et al.[66], except in Pt/Co/Ni/Co/TaN structures. They showed the effects of different applied fields on current-induced DW velocity. Out of plane (OOP) fields offset the velocity slightly, favouring the propagation of the domain aligned in the direction of the applied field, an effect which the authors noted is absent in DW velocity when driven by spin-transfer torque. Fields applied in the plane of the film modified the velocity considerably, with transverse fields having an effect independent of the configuration of the wall (up-down or down-up). By plotting the velocity against longitudinal applied field, as in Fig. 2.11, they showed data which has become ubiquitous in subsequent papers: crosses with the up-down and down-up configurations offset along the applied field axis, corresponding to the strength of the effective DMI field present at the DWs. The authors modelled this using an internal field to represent the effective DMI, with its sign depending on the DW configuration to take chirality into account, and found the model to accurately represent their data. To establish the contribution of the interfaces, Ryu et al. changed the thickness of the Pt layer. An increased thickness of Pt increased the offset of the data, which they termed the critical field, and the anisotropy in much the same manner. The change of DW velocity with applied field decreased with Pt thickness, as predicted by their model. Taking this further, the authors introduced a gold layer between the Pt and the Co

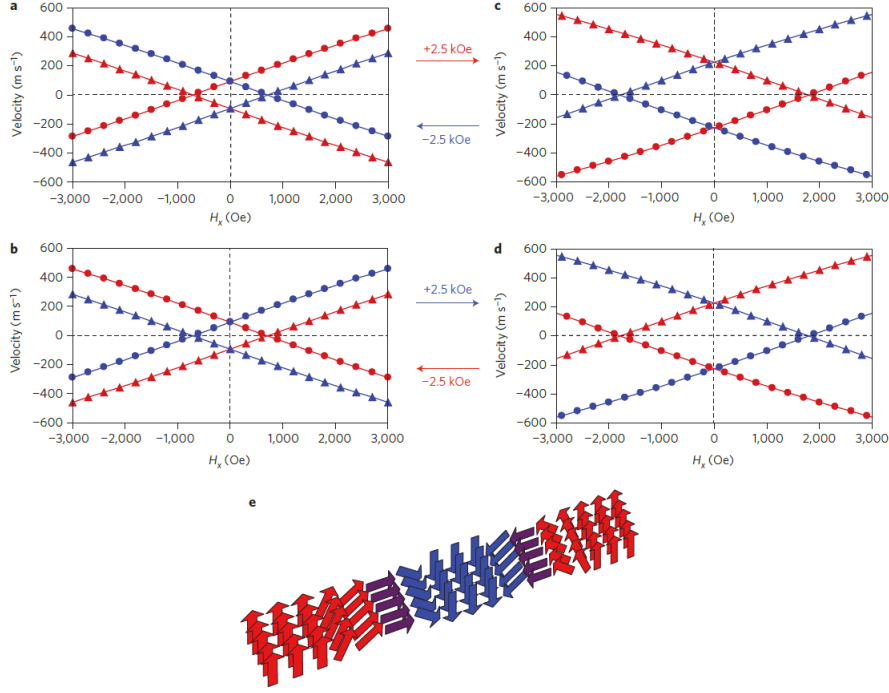


Figure 2.11: a, b, c, d, One-dimensional model of domain-wall dynamics. An analytical one-dimensional model was used by Ryu et al.[66] to calculate the current-driven domain-wall velocity as a function of longitudinal fields H_x in the presence of SHE-STT. a,b, Experimental results for opposite signs of the spin Hall angle. Red and blue symbols represent $\uparrow\downarrow$ (left side in e) and $\downarrow\uparrow$ (right side in e) domain walls, respectively. Triangles and circles correspond to positive and negative currents. These results reproduce most features of Ryu et al.'s experiments, with the major difference that domain walls move along the electron flow in zero external field. c,d, To mimic the experimental data, an internal longitudinal offset field of ± 2.5 kOe is included in the model to account for the DMI. This offset field has opposite signs for $\uparrow\downarrow$ and $\downarrow\uparrow$ domain walls. The sign of the offset field is also reversed when the sign of the spin Hall angle is reversed. These offset fields favour Néel domain walls, that is, with their magnetization along the nanowires. e, They also favour one chiral rotation direction for both $\uparrow\downarrow$ and $\downarrow\uparrow$ domain walls, as shown schematically. The chiral nature of the two neighbouring Néel domain walls shown is preserved by the change in direction of the longitudinal moment (purple) within the domain walls. Taken from Ryu et al.'s paper[66].

to suppress the proximity-induced magnetic moment. As they predicted, both the critical field and the anisotropy decreased rapidly, with the critical field approaching zero. Finally, the authors replaced the TaN cap with a thick Pt cap, and used a reduced thickness of the lower Pt layer in order to induce the spin Hall effect predominantly from the top interface and thus reverse its direction. As expected, the velocity switched sign with regard to the current. By changing the thicknesses of the top and bottom Co layers, the authors were also able to change the dominant source of the DMI, reversing the critical field. These are vital contributions to understanding the role of the interfaces upon DMI, with the critical field enabling a quantitative extraction of the effective DMI field.

Another way of extracting the DMI field, without the need to pattern samples, was introduced in a 2013 paper by Je et al.[18]. The authors nucleated a magnetic bubble domain in polycrystalline Pt/Co/Pt using an OOP field pulse, before expanding it under an applied IP field. The IP field caused the bubble to expand asymmetrically as the field worked with or against the DMI field in the DW, as illustrated by Fig. 2.12. From these expansions, the velocity was measured and a contour plot was produced of the DW velocity against applied IP field and OOP field pulse. Contours on this plot showed clearly the asymmetry in velocity with IP field being consistent under various OOP field strengths indicating a constant offset to the IP field by the DMI field. The authors explained this through a modification of the creep law, where the exponent is multiplied by a ratio of DW energy densities, with and without an applied IP field. This was done with two forms of the DW energy density, both including DMI field contributions: one for a mixed Bloch-Néel wall; and one for a purely Néel wall when the combined applied IP field and DMI field were sufficient to stabilise a Néel wall. This model was seen to describe well the shape of the bubble domains, as well as the velocity data (seen in Fig. 2.12 c), and was used in many subsequent papers. The authors then proceeded to change the Pt layer thicknesses in the structure, showing that the asymmetry was reduced as the lower Pt layer thickness was increased, but stayed constant for changes to the upper Pt layer. This began to highlight the sensitivity of

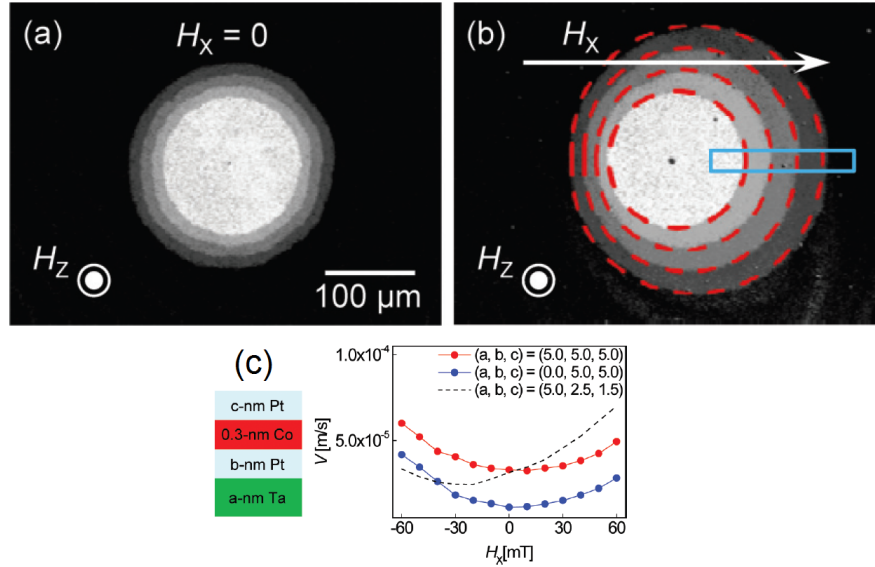


Figure 2.12: Circular DW expansion driven by an out-of-plane magnetic field H_z (3 mT), (a) without an in-plane magnetic field and (b) with an in-plane magnetic field H_x (50 mT). Each image is obtained by adding four sequential images with a fixed time step (0.4 s), which are captured using a magneto-optical Kerr effect microscope. The white arrow and the symbols indicate the directions of each magnetic field. The blue box in (b) designates where the DW displacement is measured. The dashed red circles in (b) show the calculation results based on Je et al.'s equation of domain wall energy with an extension to arbitrary angles. (c) shows almost symmetric velocity data with respect to H_x obtained from films with thick Pt layers. The black dotted line is shown as a reference of the asymmetric DW motion. The letters a, b and c in the key indicate the thicknesses of Ta buffer layer, lower Pt layer, and upper Pt layer respectively. Taken from Je et al.'s paper[18].

the DMI to structure, although the authors did not delve further into more detailed explanations.

The same bubble expansion method was used by Hrabec et al. in our paper the following year[2], except that the sample was tilted to enable the use of one magnet for both IP and OOP fields. In this paper, the effect of the interface on DMI was studied in more detail by inserting an Ir layer into a polycrystalline Pt/Co/Ir(t nm)/Pt stack. By increasing the thickness of the Ir from 0 nm to 2.6 nm, the interface could be gradually changed from Co/Pt to Co/Ir. Even a small dusting of Ir decreased the coercivity, which stayed near the subsequent value for thicker Ir layers. The anisotropy stayed mostly constant, indicating that in these samples the lower Pt/Co interface contributed the most to anisotropy, which was convenient for studying changes of the top interface without concern for the anisotropy. Looking at how the extracted DMI changes with Ir layer thickness, the sample with no Ir showed a negative DMI field indicating a difference between the interfaces even without Ir. After a dusting of Ir, the DMI fields fell to a much lower value, less than that needed to stabilise Néel DWs. The addition of further Ir switched the DMI field sign, reversing the chirality, which showed that Ir has either a much lower or opposite DMI contribution to Pt. A similar trend was found previously in work on epitaxial $[\text{Co/Ni}]_n/\text{Ir}(t \text{ nm})/\text{Pt}$ by Chen et al.[67]. Since only one interface was providing the DMI in Chen et al.'s stack, one could conclude that Ir had an opposite sign of DMI to Pt. Hrabec et al. went on to compare their polycrystalline samples with an epitaxial sample of Pt/Co/Pt which showed a near-negligible DMI, attributed to much more uniform interfaces cancelling each other's DMI contributions. This paper was an important step in ascertaining the role of interfaces on DMI, and helped make popular the bubble expansion technique of measuring DMI.

Franken et al. continued with the idea of tuning the DMI by changing layer thickness, in this case for the top Pt[14]. They estimated the DMI via current-induced DW motion, taking the slope of the depinning efficiency with applied IP longitudinal field to be the sample's anisotropy, whilst its offset from the origin relates to the DMI field. A greater offset, and so DMI field, was seen for a 1 nm Pt capping layer compared to a 2 nm capping

layer, which the authors attributed to an increase of structural inversion asymmetry increasing the net DMI, considering the Pt seed layer is 4 nm thick. Replacing the Pt cap with one of AlO_x increased the offset and decreased the slope such that the offset was not visible within the range of fields studied (± 35 mT). This was similar to previous work; the novel part of this paper came with the estimation of the DW configuration via resistance measurements. By measuring the resistance of multiple DWs under the influence of a range of IP longitudinal fields, a peak was seen at the point when the DWs change from Bloch to Néel, since Néel walls have an additional AMR resistance contribution compared to Bloch walls. No peak was seen for the sample with an AlO_x cap as the DMI was sufficiently strong to stabilise Néel walls. This data was key evidence for the switching of Bloch to Néel walls under a DMI field.

In 2015, Yang et al. clarified the origins of DMI in a computational paper on Co/Pt bilayers[62]. First principles calculations were performed in a procedure adapted for interfaces to find the total DMI strength and its distribution between layers. They showed a decrease of DMI strength with increased Co thickness for various Pt thicknesses, as shown in the previous experimental papers, as well as a decrease by half of the DMI strength when 25% intermixing was included. Replacing the Pt with Au or Ir changed the chirality of the DMI, also as seen experimentally. The individual layer analysis, reproduced in Fig. 2.13, showed the highest DMI contribution to originate in the interfacial Co layer, with smaller, opposite contributions from subsequent Co layers and a very small contribution from the interfacial Pt layer. Spin-orbit coupling (SOC) energy was seen to be correspondingly largest in the interfacial Pt from the Co layer, which the authors noted is consistent with the Fert-Levy model describing a Co-Co-Pt triangular interaction: a standard interpretation of DMI in subsequent papers. Upon calculating the DMI as a function of proximity-induced magnetic moment (PIM), Yang et al. found the DMI to decrease with increased PIM, the opposite result to that previously asserted[68]. This was explained by the competition between SOC and exchange splitting, which reduces the DMI. Similarly, a larger DMI was calculated for Co/Pt than Co/Pd due to the

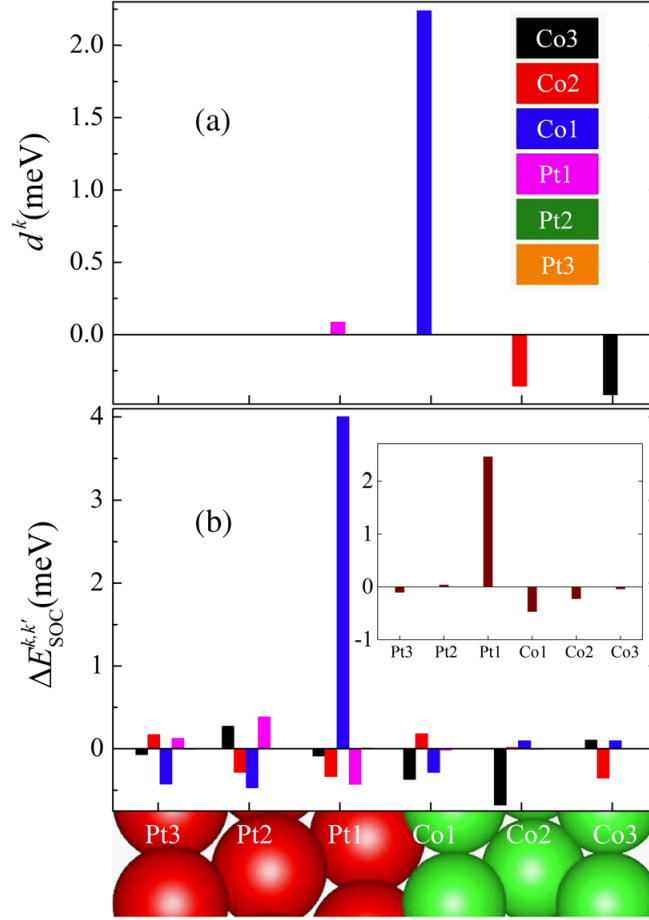


Figure 2.13: Anatomy of DMI for the Co(3 ML)Pt(3 ML) structure. (a) Layer resolved DMI coefficient d^k vs layer k . (b) The corresponding localization of the associated spin-orbit coupling (SOC) energy source in the atomic sites of all layers k' . For example, the large DMI coefficient d^{Co1} of the spin pairs in the Co1 layer [blue bar in (a)] is associated with a large variation $\Delta E_{\text{SOC}}^{\text{Co1,Pt1}}$ of the SOC electronic energy in the Pt1 layer [blue bar in (b)] induced by an inversion of the chirality in Co1. For comparison, the distribution of SOC energy variations induced by an inversion of the chirality of the total structure is shown (inset). Taken from Yang et al.'s paper[62].

higher SOC, a key part to explaining the differences in DMI between different material systems.

Further work on the origin of DMI has been carried out by S. Kim et al.[69] on Pt/Co/MgO. They used temperatures in the range of 100°C to 300°C to control the difference between IP and OOP hopping energies without permanently affecting the physical structure or major electric state of the trilayer. X-ray magnetic circular dichroism (XMCD) was used to probe the spin and orbital magnetic moments of Co and Pt. The spin magnetic moment was seen to change little with temperature, whereas the change of intra-atomic magnetic dipole moment was significant, suggesting a strong temperature dependence of IP and OOP d-orbitals. In terms of orbital magnetic moment, only the OOP orbital moment displayed temperature dependence, which showed a close connection between the orbital anisotropy and the DMI due to the similarity to the DMI temperature dependence. These results suggested that the temperature dependence of the DMI is governed by the change in asymmetric electron occupation in orbitals, which the authors proceeded to discuss theoretically. Initially a tight-binding model was used, including orbital anisotropy, which reproduced the temperature dependence of the DMI and the orbital magnetic moment. Another model based on calculations from first principles confirmed that the intra-atomic magnetic dipole moment is governed by the strength of the interfacial hybridisation and 3d orbital filling. It also showed that the DMI and orbital anisotropy follow the same trend with temperature, with deviations between them being ascribed to the aspect of orbital magnetic moment not associated with structural inversion asymmetry.

Shortly before Yang et al.'s publication, Lavrijsen et al. produced a paper looking at interface engineering in Pt/Co/Pt via alteration of the top Pt layer deposition pressure[19]. Initial magnetic characterisation showed the anisotropy, and subsequently the coercivity, to increase with deposition pressure. A deviation from linear in a plot of anisotropy against deposition Ar pressure⁻¹ showed the transition pressure between layered and alloyed growth. Using the bubble expansion method, the exponent scaling factor was extracted for no applied IP field and found to scale with the anisotropy

to the power of $5/8$, as derived by Kim et al.[70]. The key finding of this paper, however, came with application of an in-plane (IP) field during bubble expansion. Instead of elliptical bubble expansions, teardrop shapes were formed, as shown in Fig. 2.14. These domain shapes were seen to lead to velocity vs IP field graphs which differed greatly from the parabolic curves seen previously. Either a parabola with a peak at the centre was seen, at lower deposition pressures, or a severely tilted parabola with a kink. The minimum for these curves was also constant with each pressure- an unexpected observation due to the previously-found sensitivity of the DMI to both interfaces. To investigate these peculiarities further, the authors found the creep law constants at each IP field, noting that the characteristic velocity was proportional to the IP field and symmetric about zero IP field. The exponent scaling factor, however, was seen to become highly asymmetric with IP field at high deposition pressures in contrast to the inverted parabola predicted by models thus far. The authors noted this, but aside from noting a possible contribution from domain tilting, offered no solid explanation.

An explanation for the non-elliptical teardrop-shaped bubble domains was delved into by Lau et al. in 2016[71]. Using Pt/[Co/Ni]₂/Co/Ta/TaN they saw the domain wall with DMI field antiparallel to the applied field initially reach a minimum, displaying a flattened edge, before forming a pointed shape which had a greater velocity than the wall with DMI field parallel to the applied field. Taking wall energies into account, the authors calculated the lowest energy DW shape using the Wulff construction[72]. This gave the teardrop shape seen at high IP fields, for sufficiently small anisotropy, though it predicted it occurring when applied IP field and DMI field were approximately equal in strength, contrary to the observed flattening near the velocity minimum. The authors thus adopted a pseudoequilibrium Wulff construction which takes into account wall sections with multiple energy minima with magnetisation direction. This change reproduced the flattening, although only for unrealistic DW anisotropy values. The authors proposed instead that the formation of Bloch points could be the reason for such shape changes at lower fields, but did not explain much further. Nevertheless, the reproduction of the teardrop shape by their model went

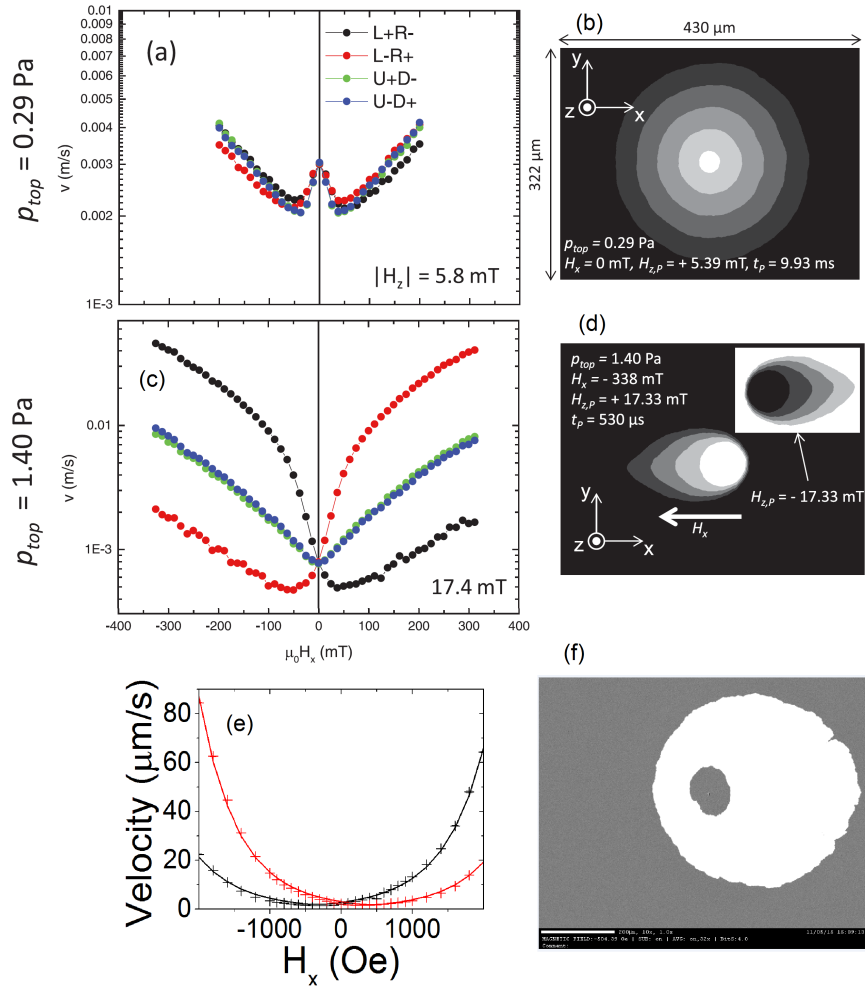


Figure 2.14: Comparison of domain wall velocity against in-plane field graphs, with their corresponding domain shapes. (a)-(d) are taken from Lavrijsen et al.'s paper[19] and show deviation from the parabolic shapes seen in this project, (e) and (f).

a way towards further understanding the effect of DMI on bubble domain walls.

The idea to include angular variation was taken further by Pellegren et al. in a paper published in 2017[73]. In it, they replaced the absolute domain wall energy density with a parameter taking the elasticity of the DW into account, being a combination of DW energy density and the second spatial derivative of DW energy density. Their analytical model was shown to agree well with simulations. They also included more explicitly perturbations from equilibrium by pinning sites, not only making the model more closely represent a physical system, but also allowing the extraction of pinning site density upon fitting to experimental data. The authors used a structure akin to that used by Lau et al.[71] to test their model and found a good agreement, extracting DMI field, pinning site density and effective anisotropy for their system. The velocity vs IP field curves were of the same form as those of Lavrijsen et al.[19] found for samples with the top Pt layer deposited at high pressures, i.e. a tilted parabola with a kink. This model was thus key to describing the DW dynamics in these sets of samples.

Following on from earlier attempts to explain asymmetries in velocity data, D.-Y. Kim et al. have used current-induced domain wall motion in Pt/Co/X/Pt wires, with X=Al, Pt, W or Ti, to shed light on the issue[74]. They used the shift in velocity vs OOP field lines for given driving currents to ascertain the spin torque efficiency which showed clearly the Néel and Bloch-Néel regimes when IP longitudinal field was varied. The pure Bloch configuration point, however, was at a different field to the minimum velocity in OOP field-driven propagation, prompting further analysis. The velocity curves were thus decomposed into symmetric and antisymmetric parts (other contributions were seen to be negligible). The symmetric part agreed well with the standard creep model without any fitting parameters. The antisymmetric part was seen to saturate at roughly the same field as that needed to stabilise pure Néel walls, with the shift in velocity minimum being at a lower field. This gave the authors reason to claim that such a shift will be inconsequential for samples with large DMI, and can be corrected using the antisymmetric saturation field, the two of which are linearly re-

lated, independent of material system, as shown by the insertion of a layer of various materials under their Pt cap. Thus, despite concerns about the basic model being inadequate for extracting DMI from samples exhibiting large asymmetries, D.-Y. Kim et al. have shown that an accurate value can still be found.

2.4 Perpendicular exchange bias

Exchange biasing, the emergence of a unidirectional magnetic anisotropy, was originally discovered in 1956 by Meiklejohn and Bean[75], with an interpretation which predicted exchange biases two orders of magnitude too large. Several more accurate microscopic descriptions have been proposed since, with perpendicular exchange bias only emerging in earnest this century. A paper which went some way towards clarifying the mechanism behind exchange bias is that from Ali et al. in 2003[76]. In it they used Co/IrMn and Co/FeMn to dispute a common theory of planar domain walls (that is, walls with their width parallel with the interface normal) being the cause of exchange biasing by calculating the domain wall width in their samples and showing that exchange biasing is seen in antiferromagnet (AFM) layers much thinner than such a width. Their data from samples of increasing AFM layer thickness, Fig. 2.15, showed an enhancement in coercivity before the onset of exchange biasing, indicating that exchange biasing is not brought about by the AFM structure stabilising either. They noted that perpendicular domain walls (those with their width in the plane of the film), however, may exist and could be a cause of the exchange bias. Training effects in their samples' hysteresis loops were used as evidence towards such perpendicular domain walls.

Along with other collaborators, Ali et al. continued in another paper to compare their data to a model of AFM DWs[77]. The model which best describes the peaks in exchange bias at low AFM thicknesses is that of Malozemoff[78], however, it is a zero-temperature model and so cannot describe the suppression of the peak as the temperature increases. To take account of this, Ali et al. employed the domain-state model, which includes

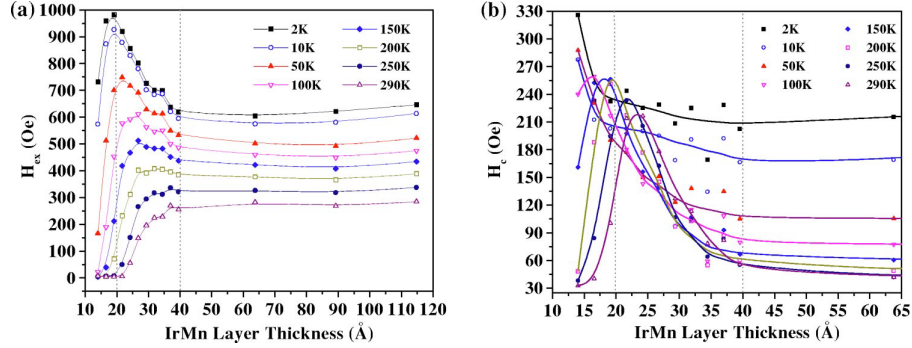


Figure 2.15: IrMn thickness dependence of the exchange bias field H_{ex} (a) and coercivity H_c (b) for a number of temperatures. Lines between the points are a guide to the eye. Taken from Ali et al.'s paper[76].

disorder in the system and uses the Monte Carlo method for calculating finite temperature solutions. The model described well the various features seen based upon the formation of perpendicular domain walls separating an IP domain structure in the AFM layer. The authors explained the peak in exchange bias with AFM thickness via DW stability: at low thicknesses, the DW was not stable enough to form consistently, leading to no pinning of uncompensated spins at the ferromagnet (FM)/AFM interface. Such unpinned uncompensated spins, however, could be switched at sufficient IP field, increasing the coercivity of the sample as seen experimentally. As the AFM thickness increased, the walls stabilised leading to many pinned uncompensated spins and a high exchange bias. At higher thicknesses, the energy cost of a DW through the entire AFM layer increased and so fewer were formed leading to a drop in exchange bias. As the temperature increased, the DWs became more unstable, needing thicker AFM layers to support them but also leading to fewer being formed; hence the shifting of the peak to higher thicknesses, and its suppression. Such an intuitive model, able to describe the complex behaviour seen, permeates through most subsequent papers.

Ali et al. used a spin valve structure so as to compare the exchange biased and free layers; Sort et al., however, used more coupled [Pt/Co] multilayers below IrMn so as to generate a perpendicular exchange bias,

in their 2005 paper[79]. Using this stack, they varied the thickness of the Co layers to assess trends in the magnetic properties. The squareness of the magnetic hysteresis loops was seen to decrease to zero for thick Co(0.65 nm to 1.3 nm), as expected from the competition between PMA and shape anisotropy, but also to decrease slightly for very thin layers (<0.6 nm). This pattern was mirrored in the effective anisotropy and several possible explanations were given, though the most likely seemed to be an increase of intermixing at the interfaces for thin Co layers reducing the PMA. A similar peak was observed for the coercivity and exchange bias, also around a Co thickness of 0.65 nm. It was suggested that these effects were linked in some part by the PMA pulling the interfacial spins into a more perpendicular direction and aligning the spin projection, thus increasing the exchange bias and coercivity. However, this effect was not the only factor affecting the exchange bias, since the exchange bias was seen to be similar for samples with very different anisotropies. The authors showed the effect of a change of Curie temperature with Co thickness, noting that for thinner Co, the Curie temperature could approach the blocking temperature of the AFM, making the field-cooling far less effective. To extend the investigation of the effect of the anisotropy, the authors inserted a very thin Pt layer in between the top Co and IrMn layers. They saw a significant peak in exchange bias with Pt spacer layer thickness for the thinnest Co layer (0.38 nm), but steady decreases for Co layers thicker than 0.6 nm. A significant increase of PMA as Pt spacer layer thickness was increased was seen in the thinnest sample, however the enhancement of the exchange bias via the resulting spin projection alignment would not account for the factor of three increase in exchange bias. It was postulated that the remaining enhancement could be from mechanisms similar to those suggested in reports that defects near the interface increase the local anisotropy or AFM structure order, effectively forming more DWs in the AFM and so increasing both exchange bias and coercivity. For samples with thicker Co, the spacer layer's enhancement of PMA was small, so the largest effect was to decrease the Co-IrMn coupling strength at the interface. From these results, a clear link was seen between perpendicular exchange bias and PMA.

From a more application-driven standpoint, van den Brink et al. made use of an IP exchange bias to aid in the switching of perpendicular tunnel junctions, the results of which they presented in a 2016 paper[80]. Using Pt/Co/Pt(0.3 nm)/IrMn/TaN structures, field cooled in an IP field to set the exchange bias and patterned into Hall crosses, as shown in Fig. 2.16, they were able to see a reversal of the Co magnetisation under sufficient applied current density with no external magnetic field. The lack of necessity for such an applied magnetic field is key to making such PMA tunnel junctions far more viable as non-volatile random-access memory and other applications. By application of an external IP magnetic field, however, either parallel or perpendicular to the exchange bias (with the current in the same direction), the authors were able to assess the full effect of the AFM layer. A field of about 5 mT antiparallel to the exchange bias was sufficient to prevent magnetisation reversal under any current density and corresponded to the translation along the applied magnetic field axis needed to make the data for the two directions of the applied magnetic field agree. Indeed, even for the highest current densities used, a field perpendicular to the exchange bias had switching of at most 50% of the domains, indicating random rather than deterministic magnetisation reversal. An explanation of the behaviour was given in terms of AFM grains, each with their own exchange bias direction. Field cooling caused each to align along their easy axis in the direction closest to the applied field, though this could be offset by a significant angle. Whilst each then contributed to the overall exchange bias in the sample, the grains further from alignment required a higher current density to switch the Co they are coupled to. When current flowed perpendicular to the set direction, however, the angular offsets cancelled out and no net exchange bias was seen. Whilst, then, this paper acted as a proof of principle for applications, it also made clearer the formation of AFM layers during sputtering.

Another paper showing a similar idea to van den Brink et al.'s paper, and published a month before, is that of Fukami et al.[81]. The main difference is that Fukami et al. used the AFM PtMn to provide both the IP exchange bias and the SHE spin current in order to switch the magnetisation of Co/Ni

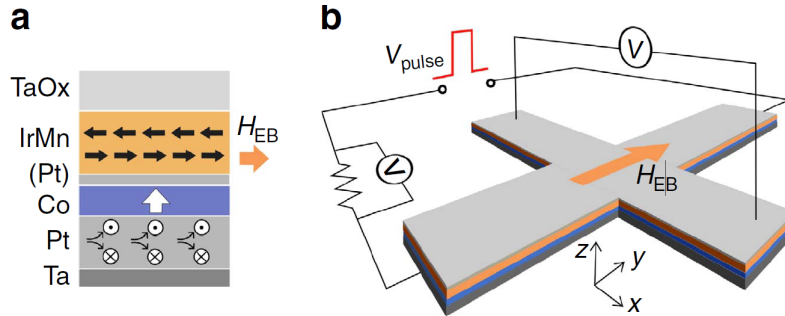


Figure 2.16: Schematic sample layout. (a) Cross-section of the deposited stack (labels indicate the deposited materials) used in van den Brink et al.’s paper, showing the magnetic easy axis of the Co (white arrow), simplified spin structure of the IrMn (thick black arrows), exchange bias (EB) field H_{EB} (orange arrow) and spin current generated from a charge current running through the Pt (circles). (b) Hall cross structure consisting of two 10×1 mm rectangles with a certain H_{EB} (orange arrow) and measurement scheme comprising a voltage pulse generator (V_{pulse}), a series resistor and two voltmeters (V). Taken from van den Brink et al.’s paper[80].

with a perpendicular magnetic easy axis. They found that at least 7 nm of PtMn was needed to bring about an exchange bias and hence deterministic switching. Beyond this, their results were very similar to van den Brink et al. with the most likely explanation also attributed to switching within grains. One additional point was made, following on from the more detailed investigation of the minor loops during switching, which was that since such a system had a range of currents over which it partially switches it could be used in memristor devices, where the resistance of the component depends upon its current history.

The mechanism behind exchange biasing due to IrMn was investigated by Kohn et al. in a 2013 paper on the structural effects of IrMn_3 [82]. Disordered $\gamma\text{-IrMn}_3$ was grown in Fe/IrMn/Cr structures, with the $L1_2$ ordering achieved via heated deposition of Ir/IrMn/Fe/Cr. The structures were confirmed using TEM and the magnetic configuration of the two was found by neutron diffraction. Figure 2.17 shows these spin configurations: the ordered $L1_2\text{-IrMn}_3$ showed a T1 magnetic structure (the magnetisation forming tri-

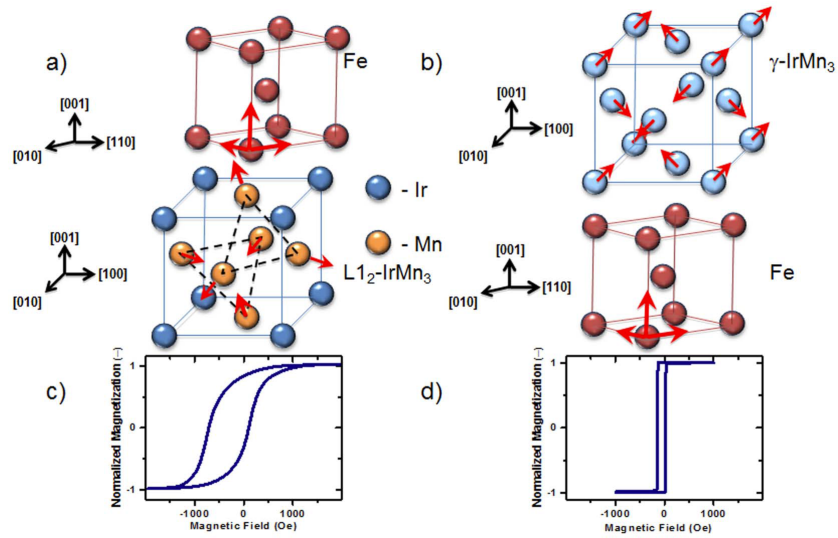


Figure 2.17: Schematic representation of crystallographic and magnetic structures of epitaxial bcc-Fe and IrMn_3 thin films, which determine the unidirectional anisotropy and hence the reversal mechanism of magnetic moments in the exchange-biased Fe layer. Magnetic structures characterized in Kohn et al.'s research: T1, chemically-ordered $\text{L1}_2\text{-IrMn}_3$ (a), and a newly characterized spin-density wave structure of chemically-disordered $\gamma\text{-IrMn}_3$ (b). The significant influence of IrMn_3 antiferromagnetic structure on interface-coupling of the epitaxial Fe layer as manifested by magnetization hysteresis loops of Fe exchange-biased to $\text{L1}_2\text{-IrMn}_3$ (c) and $\gamma\text{-IrMn}_3$ (d) (magnetic field applied along Fe[100] unidirectional axis). Taken from Kohn et al.'s paper[82].

angles in the 111 planes), whereas the disordered γ -IrMn₃ was fitted to a model in which the most likely configuration was one with the spins aligned in directions 45° away from the crystal diagonals towards the cube faces—a result not previously considered. Upon vector analysis of the Fe magnetisation switching with an applied IP field perpendicular to the exchange bias direction, it was seen that in disordered γ -IrMn₃ a two-stage process of 90° domain wall nucleation and propagation was responsible. In ordered L1₂-IrMn₃, however, a perpendicular component was detected, indicating a rotational process, which followed from the triangular T1 configuration of the AFM spins. From this paper, then, a much deeper understanding of the spin configuration in both ordered and disordered IrMn₃ was acquired.

Theories on the origin of exchange bias have thus far focussed on uncompensated spins at the interface. Yanes et al., however, put forth a model in their 2013 paper in which DMI is the cause of such an exchange bias[83]. A perfect L1₂-IrMn₃/Co interface was modelled, with no uncompensated spins, and it was found that the DMI led to a perpendicular effective DMI field, its direction dependent upon the chirality of the T1 spin structure in the IrMn₃. Introducing a Co lattice relaxation of 17% perpendicular to the interface maintained the DMI field direction, merely reducing its strength by 15%. The coercivity was seen to increase when interfacial interaction was allowed, partly from Co-Co two-site anisotropy, and partly from Mn-Co interaction distorting the T1 AFM state and creating a net magnetisation in the AFM. The authors also ran the simulations without various interactions. It was seen that with purely the DMI at the interface, a large exchange bias was seen, indicating that DMI is a primary cause; yet when all interfacial interactions apart from DMI were allowed, the coercivity increased, but there was also a smaller exchange bias in the opposite direction. This showed that whilst in this model DMI was the primary cause of exchange bias, there were other causes, although the authors did not expand upon that topic. It was also noted that the values of exchange bias found in this model were 20 to 100 times larger than experimental values, the cause of which could have been due to the model system not including defects or intermixing at the interface, as well as being carried out at absolute zero temperature. Nev-

ertheless, such a model made a considerable contribution to explaining the cause of exchange bias in systems with no uncompensated spins.

To consolidate the various areas of research into exchange bias from the start of this century, Zhang et al. published a review in 2016[84]. It covers many systems, both polycrystalline and epitaxial, and assesses the cause of the exchange bias in them along with other related effects, such as the change in coercivity. In all these systems, if uncompensated interfacial spins exist, it is their pinning which contributes the most towards exchange bias, with effects such as anisotropy variation contributing even in compensated interfaces. Uncompensated spins which are not pinned contribute towards changes in coercivity, along with long-range spin-flop mechanisms. The authors described the anisotropies associated with various systems before summarising two of the main models used to describe the magnetisation dynamics: the effective field model and that of domain wall nucleation. The effective field model averages the magnetic contributions into three fields, giving a basic model of the magnetic switching. The domain wall nucleation model considers the symmetries of the anisotropy contributions on the formation of DWs and captures many more subtle features of the magnetisation dynamics, also allowing the film microstructures to be included. Finally, some future applications of structures with exchange bias were looked at, with regard to phenomena such as Hall effects and spin torques.

2.5 Conclusions

It is principally through these key papers that significant progress has been made in understanding the mechanisms behind Pt/Co growth and magnetic structure, DMI and exchange bias. Thus the groundwork has been laid for the topics covered in this thesis, allowing a greater insight into their working and explanation. The overall aim of this project is to investigate how the interface morphology affects the Dzyaloshinskii-Moriya interaction. To that end, the background in Pt/Co studies gives a great advantage in knowing the range of layer thicknesses, deposition temperatures and pressures necessary to grow such structures epitaxially. It also gives a better idea of

the mechanisms involved, thus helping with the interpretation of X-ray data. The chosen method of DMI measurement involves propagating domain walls in the creep regime, mostly due to the well-analysed motion therein. Such analysis enables modelling of the domain wall velocity data and extraction of DMI field values. Following on from this, the work done on the cause and workings of the DMI are vital during the analysis of these extracted values, enabling a clearer understanding of how the interface affects DMI in nominally symmetrical structures. Finally, the progress made in structures with exchange bias allows greater control over the outcomes of growing structures with a ferromagnetic-antiferromagnetic interface. They allow us to better understand the magnetic behaviour seen due to DMI and exchange biasing and link that to how the interface is formed; the overall goal.

Chapter 3

Methodology

This section discusses the methods used to grow and measure samples in this project, including the limitations of the techniques and their advantages. It covers: DC-magnetron sputtering; X-ray reflection and diffraction; ways to measure the magnetisation including the extraordinary Hall effect, vibrating sample magnetometry and the magneto-optical Kerr effect; and techniques for measuring the Dzyaloshinskii-Moriya interaction.

3.1 Sample deposition

The system used to sputter samples in this thesis was a bespoke, high-vacuum, multi-sample chamber fitted with seven direct current magnetron sputter guns and two radio-frequency guns (unused) with a throw distance about 10 cm. Gun powers were limited to 50 W, but depositions for this thesis were undertaken between 10 W and 24 W, with the aim to keep the rate around 1 Å per second, as calibrated by X-ray reflectometry.

When sputter depositing, as with any type of growth, there are many parameters to take into consideration; as such, several types of sample sets were used so as to separate the contributions from each. All sample sets had a Pt seed layer deposited at 550°C onto a C-plane sapphire (Al_2O_3) (0001) substrate, which had previously been annealed at 700°C for four hours to improve the surface quality[55]. The Co and top Pt layer were

then sputtered with the substrate temperature held at a value within the range 50 °C to 500 °C to aid epitaxy, focusing between 100 °C and 300 °C where a high degree of crystallographic ordering was found previously. The base pressure immediately prior to deposition ranged from 0.6×10^{-7} Torr to 8.8×10^{-7} Torr, with most base pressures better than 3.5×10^{-7} Torr, and a working Ar pressure between 2.6×10^{-3} Torr to 3.9×10^{-3} Torr was used. The main type of sample set used had the Co/Pt bilayer grown at different temperatures, beginning with the highest temperature and ending with the lowest (Fig. 3.1 A). Sample sets in this thesis can be assumed to be set type A unless stated otherwise. Due to the heating mechanism design in the sputter system, all substrates were heated to the same degree. This meant that a significant time period, usually around 25 minutes, elapsed between growths for different temperatures as the system cooled. This had two main effects, namely allowing more time for any impurities (mostly water vapour) in the system to settle on the exposed surface of the Pt seed layer of the lower temperature samples, but also reducing the base pressure during growth as impurities were removed. Impurities were removed by the chamber pumps at a rate diminishing with improved base pressure and also by gettering, a process in which impurities react with material as it is being sputtered and so are locked into the deposit. In an effort to differentiate between the effect of temperature and base pressure, another set of samples was grown in the opposite order, starting with the lowest deposition temperature and ending with the highest (Fig. 3.1 B). Whilst this separated the contributions of base pressure and temperature, it also added the complication that all the lower-temperature samples were annealed during the growth of the higher-temperature samples, meaning that, although the samples had different deposition temperatures, they all experienced annealing at the temperature of the hottest sample grown in the set.

To separate the contribution from the two interfaces, two further types of sample set were grown where the Co layer was deposited at the same temperature for all samples and only the deposition of the top Pt layer was varied. One of these sets was in the normal high to low temperature order (Fig. 3.1 C) and the other in reverse order (Fig. 3.1 D). This was in an

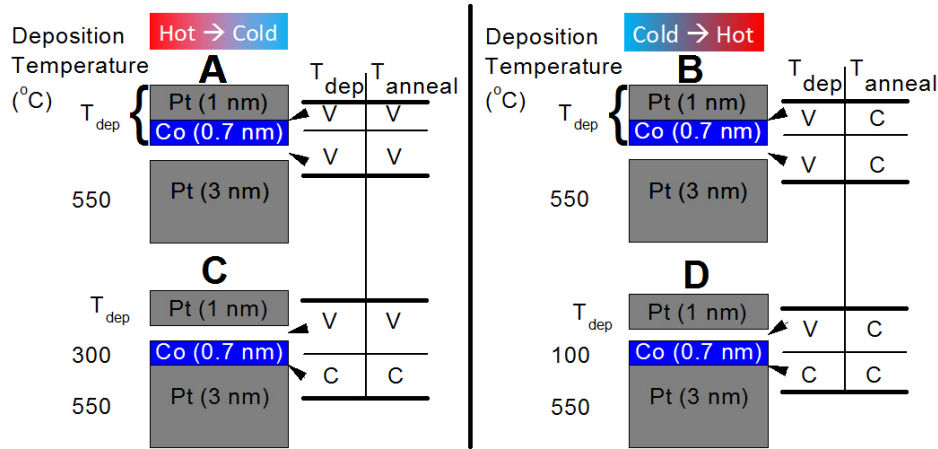


Figure 3.1: Definition of sample sets A, B, C and D according to which deposition conditions vary (V) or stay constant (C) between samples, with respect to the top and bottom Co interfaces in a Pt(3nm)/Co(0.7nm)/Pt(1nm) stack. The deposition conditions indicated are the deposition temperature, T_{dep} , and the annealing temperature, T_{anneal} . T_{anneal} is defined as the highest temperature experienced by the completed stack.

effort to keep the deposition of the lower Co interface constant whilst varying conditions for the upper. Again, in the reversed order the lower temperature samples were all annealed as the higher ones were grown.

3.2 Sputtering

Sputtering is relatively quick and cost-effective and so has been used extensively in the growth of thin film samples. Starting for Pt/Co in 1993[36, 85, 26], it was not until 2013 that the Pt/Co films were sputtered epitaxially[55]. The process remains the same and involves a non-reactive working gas, a target of the material to be deposited and a substrate on which to deposit the material[86]. These are housed within a chamber capable of low pressures, typically $< 10^{-6}$ Torr. In our case, the chamber was evacuated initially via a dry roughing pump (one without oil, thus avoiding hydrocarbon backflow, where the oil can enter the chamber), and then via a cryogenic pump. The

cryogenic pump operates by cooling a surface to very low temperatures (in the region of 18K using liquid helium), upon which the gases in the chamber condense and so are effectively removed from the chamber. This method of cooling is less effective for lighter molecules, especially helium, however it removes a sufficient amount to allow sputtering with few impurities. Another system used for removing impurities is the Meissner trap, which works along the same lines as a cryogenic pump, except at higher temperatures (using liquid nitrogen) with a larger surface area, and is particularly effective at removing water vapour. This typically decreased the base pressure in the chamber by an order of magnitude. Water vapour can be a particular problem when sputtering, unlike helium, due to its reactive nature and its persistence in maintaining a presence on the walls of the chamber. An effective technique against such a presence is to perform a bake-out, where the chamber is heated to evaporate the water vapour and allow it to be trapped more permanently by the pumps. Before depositing on sapphire, the substrates in this thesis were heated to allow reconstruction of the surface and to evaporate any residue, improving the quality of the surface. The entire chamber heated up during this stage and so it additionally acted as a bake-out. By lowering the base pressure of the chamber in these ways, one can reduce the number of impurities in the deposited films, especially at the interfaces, which can remain exposed in the time before subsequent layer depositions.

Once a sufficient base pressure has been achieved, a pure working gas (argon in our case) is allowed into the chamber, typically to the pressure of a few mTorr. A high voltage is applied in a gun between an anode and the target material, see Fig. 3.2, which ionises the working gas molecules and accelerates them towards the target. Upon collision, the ions displace atoms of the target which then travel away, a number of them landing on the substrate and gradually forming layers. In our case, where conductive targets were used, a DC voltage on the order of 200 V was able to be used; if the target is an insulator, however, an AC voltage is needed to avoid building up an excess charge on the target which repels any further ions, although this was not used on any samples from which data was used. To reduce the

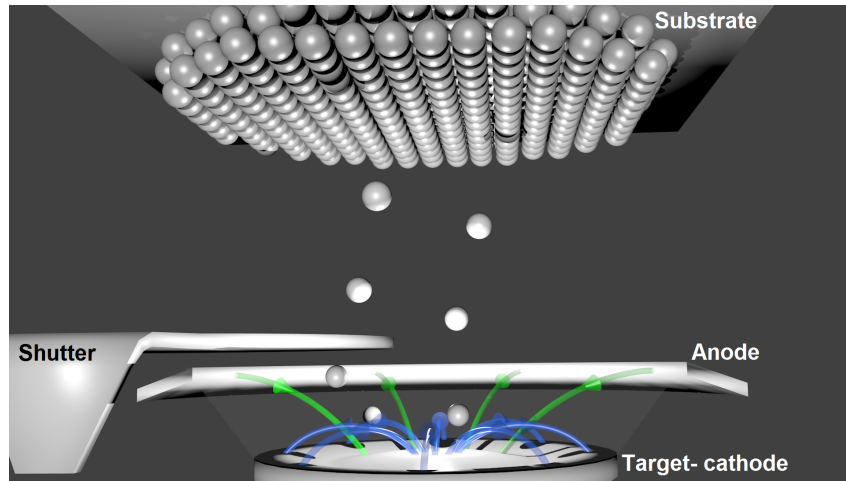


Figure 3.2: Diagram of the sputtering set-up inside the chamber. The blue and green arrows represent the magnetic and electric fields, respectively.

pressure of working gas needed to maintain a constant plasma, a magnetron was used to direct the flow of ions into a toroidal racetrack, increasing their local density. A lower working pressure increases the mean free path of the displaced target atoms meaning their kinetic energy is not as diminished from collisions when they reach the substrate, allowing more energetic adsorptions, as well as decreasing the number of atoms which deviate away from the substrate. If, for a given pressure, there is insufficient working gas to maintain a steady plasma, the power of the gun can be increased; this will increase the current, allowing more atoms to be ionised. It will also increase the voltage, imparting more kinetic energy to the particles as they are accelerated towards the target and knocking off more target atoms. Combined with the increased number of ions colliding with the target, this increases the sputter rate, forming layers on the substrate more quickly.

As the sputtered atoms arrive at the substrate, they settle into position, diffusing towards areas of lower energy. This can either be seen as spreading out or, alternatively, clumping together into groups. The former is usually preferred for thin-film devices, but which behaviour occurs depends upon the material and sputtering conditions. Likewise, the speed at which this

happens depends mostly upon the material and the temperature of deposition. If the deposition is too fast, new layers form before the previous one has fully relaxed and so defects are formed in the film. Conversely, if the deposition is too slow then more contaminants in the chamber can settle on the film, causing impurities as they are buried by subsequent layers. The defects of the former can be mostly removed by annealing, where the high temperatures overcome energy barriers, allowing atoms to fill vacancies and realign slight crystal orientations. This also, however, promotes more intermixing at the interface[87]. In the latter case, where impurities are buried in the film, the effect of annealing will most probably depend upon the types of impurity.

3.3 X-ray reflection and diffraction

The structure of thin film samples plays a very great role in its magnetisation dynamics, so the ability to characterise certain aspects of it is vital. X-rays allow one to extract properties of the internal structure of samples, such as layer thickness, electron density, crystallographic ordering and interface roughness and intermixing. The basic setup is shown in Fig. 3.3 and involves an X-ray source irradiating the sample at an angle ω to the sample surface, with a detector at angle 2θ to the incident X-rays, in the same plane as ω . The main scan type used is a specular scan where ω is varied and 2θ is changed to be twice ω . This is done at high angles ($\omega > 15^\circ$) for the analysis of crystallographic ordering or at low angles to enable the extraction of layer thicknesses, electron density and interface roughness-intermixing. Since the scan takes in a large portion of the film, any roughness is averaged out and is indistinguishable from intermixing. Rocking curves can be used subsequently, where ω is varied whilst 2θ is kept fixed, to separate roughness and intermixing.

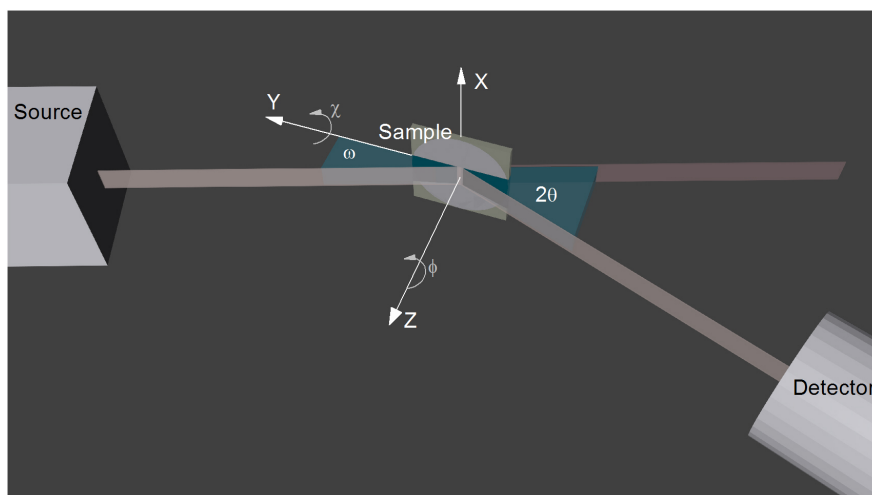


Figure 3.3: The geometry of X-ray reflection with the axes of motion in one of the X-ray machines, Ark, labelled.

3.3.1 X-ray theory

The X-rays in this project were generated by an X-ray tube, in which electrons were rapidly accelerated towards a target, in this case copper. The energy imparted by these incoming electrons raised electrons in the copper from the K shell (2s orbital) to a higher one. This allowed electrons, particularly in the 2p orbital (L_2 and L_3 shells), to fall into the vacancies, emitting X-ray photons in the process. K_α comes from the electron falling from the 2p orbital and since this involves two shells, two varieties of K_α photons were emitted: $K_{\alpha 1}$ from the L_3 shell and $K_{\alpha 2}$ from the L_2 shell. In the X-ray kits used here, all but K_α was removed, with the option of removing $K_{\alpha 2}$ using a 4-bounce, where the beam is refracted between two crystals, ‘bouncing’ four times, such that just the $K_{\alpha 1}$ photons remain.

Here, roughness was defined as the collective deviation of atoms from an atomically sharp interface, and intermixing as the deviation of individual atoms. A parameter combining the two, σ , was taken as the interface disorder, defined as $\sigma = \sqrt{\text{roughness}^2 + \text{intermixing}^2}$.

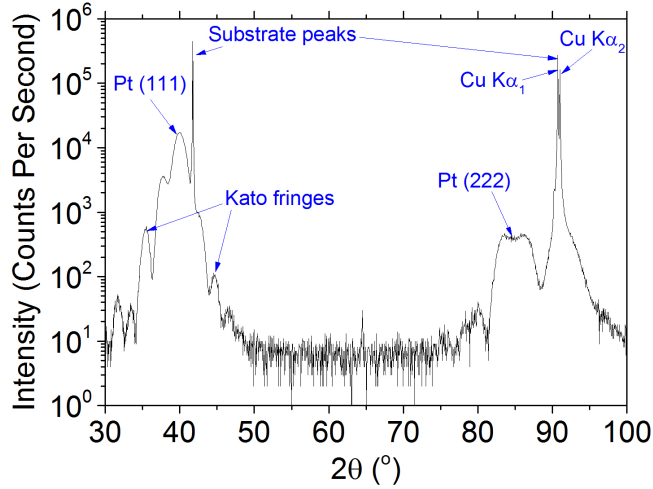


Figure 3.4: An example high angle X-ray diffractometry scan of Pt/Co/Pt with various features labelled.

Specular reflection

Specular scans vary ω , the angle between the X-ray source and the samples surface, and 2θ , the angle between the X-ray source and the detector, such that $2\theta = 2 \times \omega$. In this project, X-ray scans were restricted to reflection, so $0^\circ < \omega < 90^\circ$. Under these conditions, the reflected beam was modulated by Bragg's law, which states that reflections from parallel surfaces interfere constructively when the path difference between beam paths is equal to an integer number of wavelengths. Since the path difference is dependent upon the angle of incidence and reflection, the Bragg condition can be found: $\sin \omega = n\lambda/(2d)$ where d is the distance between layers, λ is the wavelength of the beam, in this case 0.154 nm, and n is an integer.

Since the distance between atomic planes is comparable to the wavelength, at high angles, peaks in detected X-ray intensity with angle appeared, as shown in Fig. 3.4. From the angle at which these peaks appear it is possible to establish the distance between atomic planes which, when the material and its lattice spacing is known, can provide the crystallographic directions present in the sample. If only the peaks associated with one crystallographic direction are seen then the sample can be established

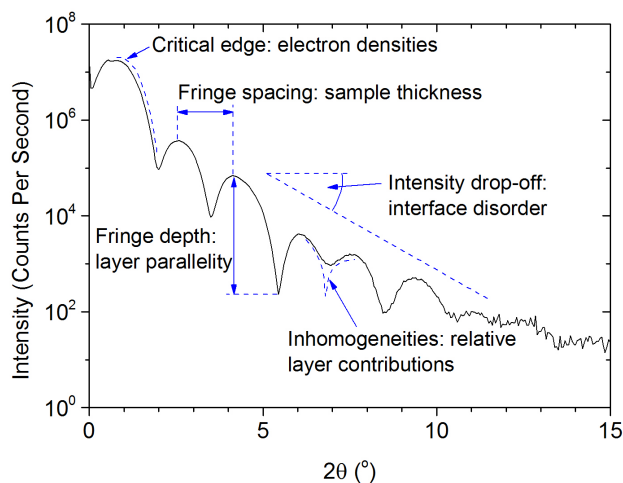


Figure 3.5: An example low angle X-ray reflectivity scan of Pt/Co/Pt with various features labelled.

as epitaxial or nearly-epitaxial. One cannot be certain of perfect epitaxy as peaks from a less common crystallographic direction may well exist, but have intensities below the level of background noise. The widths of the peaks can also be useful since they depend upon the thickness of the contributing layers and the spread of atomic plane distances from strain; although instrument broadening must also be taken into account.

At lower angles the same effect can be seen but from interference between material layer interfaces, rather than crystal layers. However, since the path differences are made from multiple wavelengths, the Bragg condition is met more regularly as the angle changes and the peaks are seen as fringes, illustrated by Fig. 3.5. The resulting diffraction pattern is a convolution of fringes from each combination of interfaces[88]. By analysing these fringes a number of sample properties can be deduced such as layer thicknesses, electron densities, how parallel the layers are and the interfacial disorder. The angular spacing of the fringes is inversely proportional to the distance between the reflecting surfaces since the bigger the distance, the smaller the angular change needed for a given path difference. The deepness of the fringes when undergoing destructive interference indicates how

parallel the reflecting interfaces are. This is because interfaces which are not parallel will vary in distance between them at different points on the film, meaning that there will not be a single angular value that undergoes complete destructive interference. The rate at which the fringes lose intensity with angle indicates roughness-intermixing, σ . The more disordered the interface, the more off-specular scattering occurs and so the less intense the specular reflection. The position of the critical edge allows estimation of the electron densities. At very low angles one sees total reflection from the sample. Above a critical angle dependent upon the refractive index, and thus the electron densities, the beam begins to be transmitted into the sample and so a drop off in intensity is seen- the critical edge. Using these principles, one can use a model stack to simulate the convoluted pattern and by fitting this to measured data one can extract values for the various sample properties.

When fitting a model to data, a parameter known as goodness of fit, GOF, is used to gauge how close the parameters are to being correct. This is a measure of how far the simulated points are from the actual ones. Four of the main ways to calculate this GOF are mean absolute error (MAE), mean squared error (MSE) and the logarithms of each. These give different weightings to different parts of the scan. MAE takes an average over the scan of the absolute difference between the model and the measured values. MSE does the same but with the squared difference and gives more weighting to the points where the biggest difference is found. Thus MSE is most useful in scans with very low noise. Since the scan data decreases rapidly in intensity with angle, both MAE and MSE give far more weighting to the lower angles. This is useful for fitting the critical edge and extracting electron densities. The logarithms of MAE and MSE drastically reduce the contribution from the lower angles allowing the entire scan to be fitted with more balanced weighting. Thus for scans with appreciable noise, $\log(\text{MAE})$ was most often employed.

Due to the noise in the measured data, the fitted model can never be perfect and so one must appreciate the reliability of various extracted values. Due to the regular repeats of the fringes, the total thickness of the sample can

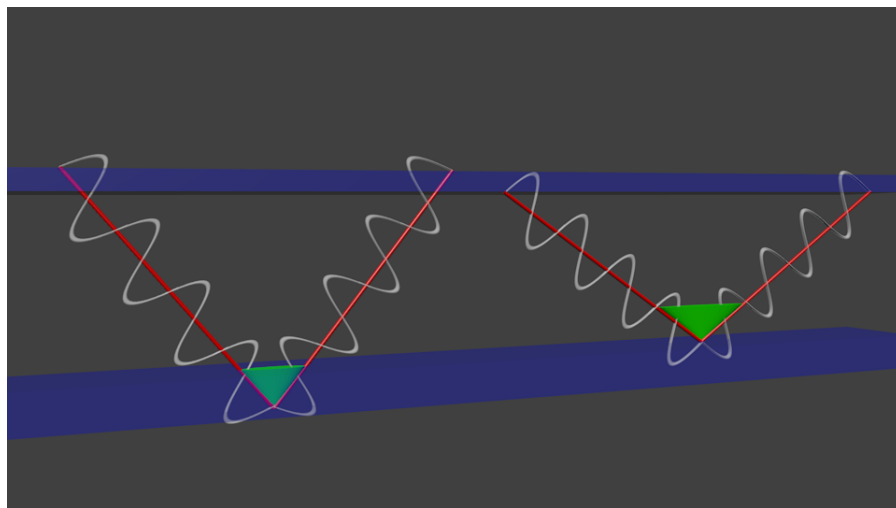


Figure 3.6: A representation of X-ray reflection from a layer with significant interface disorder, highlighting the range in angle over which constructive interference can take place. The blurred interfaces are in blue, the X-rays in white, their paths in red and the angle of specular scattering in green.

be found most reliably. The total σ can also be trusted from the overall drop off of intensity with angle. The parameters of individual layers, however, are less reliable as the contribution from one parameter can be skewed by the others. Thus the reliability of the fitting of one parameter depends upon the model being in a global minimum of GOF, not stuck in a local minimum.

Figure 3.6 shows how disorder at the interface leads to a range of reflection angles over which constructive interference can take place for X-ray reflection off a layer. The large difference in angles seen in these extremes smooths out the Kiessig fringes, disrupting the interference pattern. The blurred interface model fits mostly with disorder from intermixing; however, when averaged over a large area, interface roughness can also be approximated as such.

Rocking curves

Since most X-ray scans probe a large area compared to atomic distances any interfacial or surface roughness is averaged out and is indistinguishable from

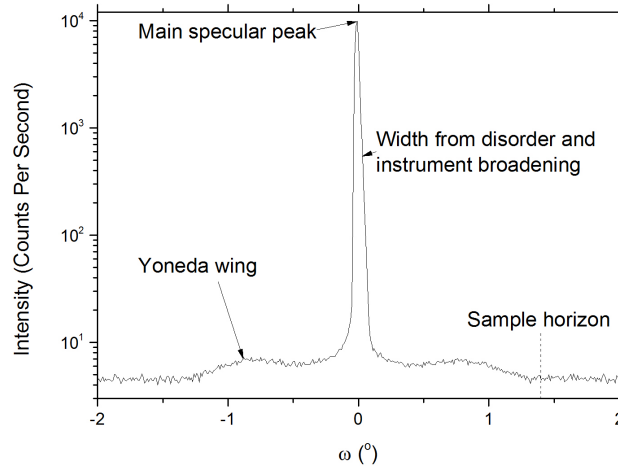


Figure 3.7: An example X-ray rocking curve of Pt/Co/Pt taken at the first Kiessig fringe. Here, ω has been shifted to have its zero-point at θ .

intermixing. To separate roughness and intermixing, examples of which are shown in Fig. 3.8, off-specular reflections need to be detected where the change in wave vector is not parallel to the surface normal. This is achieved through rocking curves, where 2θ is held constant and ω is varied, as shown in Fig. 3.7. Intermixing should not contribute to these off-specular reflections since it merely spreads out the interface, leaving it perpendicular to the sample normal, and so by assessing the relative intensities of the specular to diffuse reflections, one may gain an indication as to the overall roughness. One difficulty with this method is that the diffuse scattering can have an intensity comparable to background noise; as such these rocking curves are often performed at lower angles at the peak of a Kiessig fringe. The lower angles, whilst increasing intensity, also decrease the sample horizon, where $\omega = 0$ or $\omega = 2\theta$ such that the incoming or detected X-rays are parallel to the sample surface and intensities at further angles cannot be taken. This becomes a hindrance if the diffuse scattering extends to angles beyond the sample horizon since then some diffuse intensity will not be accounted for when comparing with specular, skewing the results.

A further peculiarity with these scans comes in the form of Yoneda wings. These are peaks in intensity at either side of the specular peak, correspond-

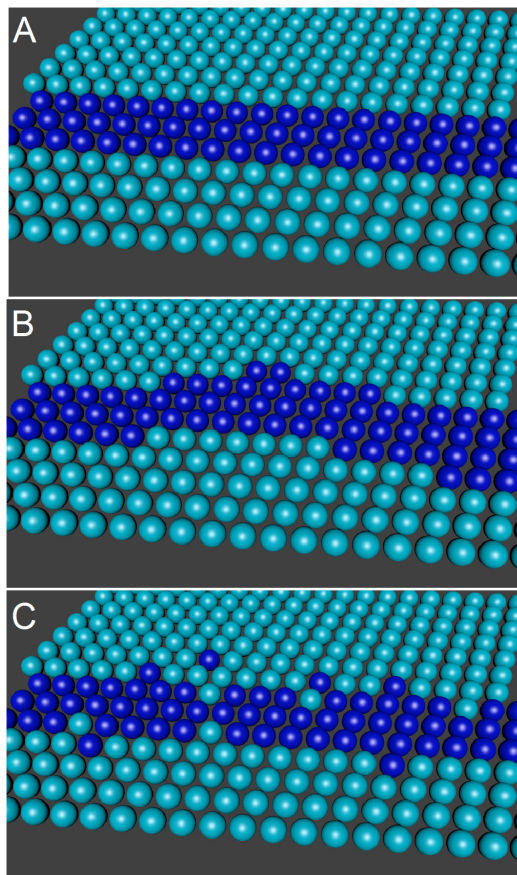


Figure 3.8: Representation of disorder in the fcc Pt (111)/Co/Pt stack. Roughness (B) is taken to be the deviation of the interface from perfectly smooth (A). Intermixing (C) is taken to be the deviation of individual atoms away from the interface.

ing to the critical angle of reflection. Their origin is mostly ascribed to resonance peaks from double diffraction[89]. Another promising theory is that at the critical angle of reflection, between total reflection and partial transmission, the incoming beam is reflected parallel to the sample's surface, allowing for many scattering events to occur and so increasing the intensity of the detected X-rays[90]. A similar process happens in reverse, when the detector is at the critical angle.

The overall scan should then be a combination of a specular peak and diffuse wings. The specular peak will be a delta function, broadened by several processes. Instrument broadening occurs due to the beam at the source and the detector being finite in width- this spreads the angles over which the detector picks up specular reflections. The other main source of peak broadening comes from interface disorder, where roughness slightly shifts the angle for specular reflectivity and intermixing spreads the depth over which reflections can occur, widening the possible angles for specular reflectivity. The more serious roughness effectively removes intensity from the specular peak and shifts its angle into the diffuse scatter.

3.3.2 X-ray techniques

All X-ray data in this project was obtained through the use of a Bruker D8 Discover (dubbed Arkengarthdale, or Ark) and an older, bespoke machine (dubbed Wharfedale). The former is faster and affords a greater number of axes of motion. The latter, however, generates more intense X-rays and so was needed specifically for seeing features which would otherwise be lost to noise, such as some rocking curve shoulders. To load Wharfedale the sample must be placed on some Blu Tack on a plate and pushed against it with another plate until its surface is in the plane formed by three pillars arising from the plate. These pillars are aligned with the system and so this loading technique eliminates the need to align the sample in the χ or Z directions (see Fig. 3.3). The technique does, however, add the possibility of damage to the sample surface from the pressing plate. To alleviate this, a tissue was used to add a protective layer and no change was seen in magnetic behaviour before

and after the loading procedure. The alignment of ω involves a rocking curve with 2θ fixed at one degree, for alignment to the sample surface.

Arkengarthdale's loading procedure consists of placing the sample onto the sample holder and securing it through the use of suction on its reverse side. This removes the possibility of damage to the sample surface, but means that χ and Z are not automatically aligned, making the alignment procedure more involved. The alignment of ω remains the same as with Wharfedale, but afterwards Z -scans and χ -scans need to be carried out, with rocking curve scans in between, until the change in alignment is negligible. This is because as one axis is aligned, it moves the others slightly out of alignment. The rocking curve was repeated most as alignment is most sensitive to ω . At lower angles of 2θ , χ has a very small effect on alignment, but grows larger as 2θ increases.

3.4 Magneto-optical Kerr effect

3.4.1 Magneto-optical Kerr effect theory

A key technique in assessing the magnetic behaviour of thin samples is that of Kerr microscopy. This utilises the magneto-optical Kerr effect to track magnetisation spatially. First observed by John Kerr in 1877[91], it describes the rotation of the polarisation of light when reflecting off magnetic material, similar to the Faraday effect[92] which concerns light passing through a material. Since the rotation is proportional to the magnetisation, one can measure relative magnetisation by, for example, using crossed-polarisers to convert the rotation to intensity.

The effect is a consequence of the magnetisation introducing an asymmetry into the permittivity of the material, seen as off-diagonal terms in the dielectric tensor[93]. This causes the components of the light to have different velocities when moving through the material, but also changes the phase difference between them when they are reflected. There are three main configurations of the magneto-optical Kerr effect, as shown in Fig. 3.9: polar MOKE where the magnetisation is out of the plane of the film; longitudinal

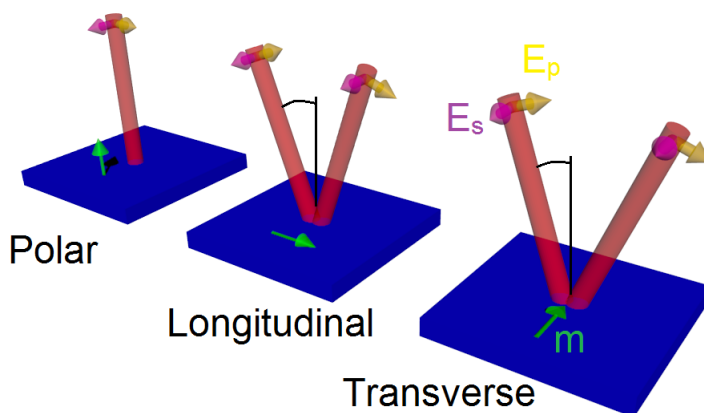


Figure 3.9: Illustration of the various geometries employed using the magneto-optical Kerr effect. The magnetisation of the samples, m , is indicated by green arrows. The optical beam, red, has components of the electrical field in the p, yellow, and s, purple, directions. The black arcs show the angle of incidence.

MOKE where the magnetisation is parallel to both the film and the plane of incidence; transverse MOKE where the magnetisation is parallel to the film, but perpendicular to the plane of incidence. These configurations are probed by light with electric components in the plane of incidence, E_p and/or perpendicular to the plane of incidence E_s , either in phase leading to linearly polarised light, or out of phase leading to elliptical or circularly-polarised light. Polar MOKE leads to a small electric component, orthogonal to that from the incident light, and so does not depend upon a particular incident polarisation to have an effect. This is similar for longitudinal MOKE, except that the angle of incidence must be non-zero, the MOKE signal growing smaller the closer the incidence angle is to zero. Transverse MOKE differs from polar and longitudinal as it adds a small electric component parallel or antiparallel to the incident electric component when using p-polarised light, thus changing the intensity, rather than rotating the polarisation. When s-polarised light is used, there is no effect. With a mix of s- and p-polarised light in a transverse setup, both the intensity and polarisation angle are altered as the p-component's intensity is adjusted. Transverse MOKE also

requires the angle of incidence to be greater than zero.

3.4.2 Magneto-optical Kerr effect techniques

Laser MOKE was carried out in a darkroom using a Thorlab 10 mW 3B HeNe laser of wavelength 632.8 nm (model HNL100L), with electromagnets capable of applying up to 550 mT at the sample location controlled via software. A Thorlab GTHM polariser, placed immediately after the laser, polarised the beam horizontally (that is, p-polarised), with an equivalent adjustable analyser placed just before the photodiode. Longitudinal measurements with a magnetic field applied in the plane of the sample were taken by direct reflection off the sample. Polar measurements with the applied magnetic field perpendicular to the sample plane were taken by reflection off one mirror, through a half-reflecting mirror and through the pole piece of one of the magnets, before reflecting off the sample, back through the pole piece and reflecting off the half-reflecting mirror into the analyser. Towards the latter part of this project, a lock-in amplifier was added to the Laser MOKE setup. This used a modulator placed between the laser and the polariser to modulate the beam. The detected beam was then demodulated, removing some of the noise. The frequency of modulation was kept at a high enough value (about 100 kHz) compared to the sampling rate that there was no overlap between measurements. In both cases, the hysteresis curves were constructed point-by-point, averaging over a period on the order of 0.1 s.

Out of plane (OOP) measurements were first taken over the full range of applied magnetic fields (± 550 mT) to ensure sample saturation with a coarse increment. When the switching fields had been found, magnetic field sweeps of increments sufficiently small to give several points during magnetisation switching were taken, focused on the regions of switching. The magnetic field range was insufficient for IP measurements for most samples due to their high anisotropy (on the order of 1 T) and, as such, were only taken for samples if their OOP loops appeared as if along a hard axis.

3.5 Anisotropy measurements

The magnetic anisotropy, or symmetry breaking, in a material can greatly affect its magnetostatics. In bulk samples, this manifests mostly as magnetocrystalline anisotropy from the symmetry breaking due to the crystal structure. This causes orbitals to align preferentially along certain directions, making the magnetisation do likewise. Since actual samples are not infinite in extent, shape anisotropy can come into effect. This involves the magnetisation shifting to minimise stray fields at the interface and, if strong enough, can cause the magnetisation to break up into multiple domains. Furthermore, there are interface anisotropies from interactions with other materials at the interface. This is particularly pronounced in the samples in this project as the interaction between Co and the sandwiching Pt is strong enough that, for thin layers of Co, the magnetisation prefers to be orientated out of plane (OOP) in what is known as perpendicular magnetic anisotropy (PMA). This comes from hybridisation between the Co 3d and Pt 5d orbitals at the interface[39], drastically reducing the energy for the perpendicular alignment of the Co spins. Since spins in subsequent Co layers experience this PMA second-hand through the exchange interaction, interfacial anisotropy is proportional to the inverse of the layer thickness. This is an example of uniaxial anisotropy, where all the spins prefer to align along one axis.

An additional anisotropy effect is exchange biasing, in which an asymmetry is induced in the magnetisation direction usually taking the form of a unidirectional anisotropy. In this project the main source of exchange biasing is from an antiferromagnetic layer on top of the ferromagnetic layer. Antiferromagnetic materials contain layers of spin alternating in direction. At the interface, there is usually some diffusion of atoms from the antiferromagnet, resulting in about a monolayer where some antiferromagnetic atoms are uncompensated by their surrounding atoms, allowing them to couple with the ferromagnetic atoms and change their magnetisation direction[78]. Of these, a few are pinned in their direction by the antiferromagnet and it is these pinned uncompensated atoms which contribute an exchange bias[94].

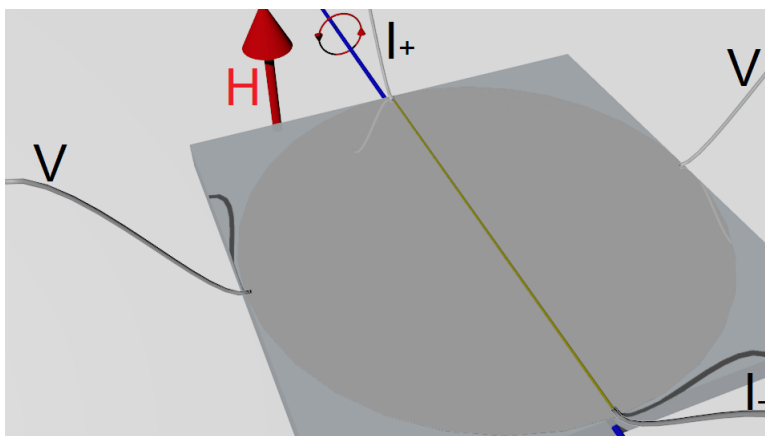


Figure 3.10: The geometry of anisotropy measurements showing the axis of rotation (blue), applied magnetic field, H , (red) and average current path (green).

The main method employed to measure anisotropy in thin films used measurement of the AHE voltage to ascertain magnetisation, akin to the measurements done by Moon et al.[95]. Four contact points were wire bonded onto the sample at the centre of each edge, as close to the edge as possible whilst maintaining good contact with the film, as seen in Fig. 3.10. The sample was placed on a rotatable stage with the axis of rotation in the plane of the film and a magnetic field applied perpendicular to the axis of rotation. A current was applied across the contacts at the sample extremes along the axis of rotation; to get a true measurement of AHE, the path between the contacts must be parallel with the axis of rotation, else the effective strength of the applied field perpendicular to the average current path would change with rotation angle. The voltage is measured across the two contacts at the sides; again, these need to be perpendicular to the average current path, else they'd pick up part of the applied voltage. Ideally these measurements would be done on Hall crosses, thus ensuring perpendicularity, but the method is durable enough to be accurate with sheet films if care is taken in the bonding.

To perform the experiment, the magnetic field was applied at several

small angles around the sample normal. The field magnitude was kept small compared to the anisotropy field; this was such that the magnetisation shift would be small and high order terms in the expansion of the angle cosine could be neglected. The anisotropy field was estimated from in-plane (IP) laser MOKE scans, though since the magnetic field was insufficient to saturate most of the samples along their hard axes, the highest applied IP field was taken as a minimum value for effective anisotropy field. At each field, the current was applied in a positive and then negative direction four times and the transverse voltage measured for each. The switching of current sign cancels contribution from contact resistances and the repeats serve to reduce uncertainty in the measurement. The voltage is brought about by the OHE, from the applied magnetic field, and the AHE from the magnetisation of the sample. Moon et al.[95] considered the OHE to be negligible compared to the AHE in this configuration, but to confirm this, several applied magnetic field strengths were used; since the OHE varies linearly with field strength, it is then possible to differentiate between OHE and AHE. Since the AHE is directly proportional to the sample magnetisation, the angle of magnetisation could be found for each applied field angle, yielding the anisotropy of the sample.

3.6 Vibrating sample magnetometry

VSM is another technique used to measure a sample's magnetisation for a given applied field. The sample is placed in a uniform magnetic field to magnetise it and vibrated in a direction perpendicular to the field. Pickup coils nearby detect the changing stray field from the moving sample, converting it into an electrical signal. This signal is put through a lock-in amplifier, which amplifies the components of the signal which are in phase with the reference signal, in this case the frequency of sample vibration, which cuts out the majority of random noise. The resulting signal is directly proportional to the magnetisation of the sample, allowing its absolute magnetisation to be found once the system is calibrated for samples in a defined position. The system used here was encased in a vacuum jacket with a heater and flow of

He to control the temperature. Liquid He was also used to cool the superconducting magnets, allowing high fields (up to 7 T) to be applied. This was more than sufficient to saturate all of the samples used in this project along their hard axis.

Whilst VSM is a powerful technique, it becomes less effective for OOP-magnetised thin films. This is because for such a sample, the only reason the stray field is not cancelled by the demagnetising field is because of the sample's finite size, since for an infinite film the stray field is entirely cancelled. Thus what stray field there is is quite small and so the measurements are quite prone to noise. It is for this reason that, whilst the saturation magnetisation has been measured by this method, the hard-axis loops obtained were for the most part insufficient to extract a reliable value for anisotropy.

3.7 Kerr microscopy

Whilst the laser MOKE magnetometer can measure the relative change in magnetisation and VSM can measure the average magnetisation, both for the entire film, for domain imaging, a Kerr microscope was employed. The resolution, down to the order of μm in our system, is not as high as some other techniques such as spin-polarised scanning electron microscopy or magnetic force microscopy, however, it does enable quick dynamic imaging of magnetic domains. An Evico brand Kerr microscope was used employed in this thesis, used in polar mode, mostly at 10x magnification. The mechanism is the same as for the laser MOKE, except that instead of a laser, light from a light emitting diode is polarised and focused onto an area of the sample that is viewed under a microscope. The image, after being put through an analyser, is either sent to an eyepiece or into a camera. A magnetic field can be applied through the use of several magnets and coils: the most used setups were the large OOP magnet for imaging domains in samples with high coercivity; and an IP magnet with a sample holder which could be replaced by a small, bespoke OOP coil, which was used for DMI measurements.

3.7.1 Bubble domain expansion

The main method employed for measuring DMI is the bubble domain expansion technique[2]. This involves nucleating a domain in the film which, for most of my samples, appears as a fairly round bubble when viewed by Kerr microscopy. This bubble is then expanded through application of an OOP field under various IP fields and a difference image captured, subtracting the image before the pulse from the image after. The IP fields either enhance or diminish the effective DMI field in the domain wall, depending upon its orientation, and so an asymmetry is seen.

3.7.2 Python fitting software

In order to analyse the vast number of difference images produced by Kerr microscopy, an automated system of extracting the distances moved by domain walls was needed. For this, Python was used to find a bubble domain centre and search for contrast changes along horizontal lines in each direction parallel to the applied IP field, over a small band close to the bubble centre. Area averaging and checks further along the path were employed to increase reliability and decrease the chances of confusion by defects. Once two changes in contrast had been found, the distance between them was found and averaged over all the paths. If only one contrast change was seen in a path, the domain wall was assumed to have expanded beyond the field of view and the path discounted, and if this occurred for too many paths in either direction in an image, that direction for that image was discounted. Thus, for each image, a value of domain wall movement distance was obtained in both directions parallel to the applied field. For each sample, for each IP and OOP field configuration, at least three images were taken and averaged, before being combined with the OOP field pulse duration to provide the domain wall velocity. In this way, the domain wall velocity data was accrued.

3.7.3 Domain wall annihilation

When the DMI is strong enough and Néel components are stabilised in domain walls, as domain walls meet they do not immediately annihilate but instead form Voronoi-like networks of domain wall pairs [96]. As the domain walls in a pair have the same chirality, a large field is required for them to annihilate with each other. This state is particular to walls with a Néel component due to the magnetic charge build-up across the wall, a feature lacking in pure Bloch walls except at the ends of the walls. This build-up keeps the walls in a 360° domain wall configuration until the structure of the domain wall can be reconfigured. This means that during an OOP field sweep, if the maximum applied field is not sufficient to provide such a force, then on the return sweep domains will expand from these pre-existing domain walls, effectively lowering the coercivity. By measuring the coercivity for a variety of maximum fields one can see a saturation point when all walls have been annihilated. The field needed to annihilate these walls is related to the Néel wall stability, and hence the DMI. To find this relation, however, simulations must be carried out and, without detailed information on the sample's defect density, a smooth wall is used giving a lower bound on the strength of the DMI.

3.7.4 Other DMI measurement techniques

Alongside these DMI measurement techniques, there are several other possible methods. Current-induced domain wall motion can be used to propagate domains down thin wires under applied IP magnetic fields [97]. This has the advantages that only one magnetic field direction need be applied, samples with high coercivity can be studied more easily and multiple walls can be measured simultaneously. It does require that the samples are patterned into wires, however, and introduces complications when considering the effect of an IP field on the operation of the SOT driving the DW motion.

A recently proposed method of measuring DMI is by using domain nucleation in thin films patterned into triangles [98]. The coercivity is then found under various applied IP fields, aligned along a symmetry axis of the

triangles. The DMI in the sides perpendicular to the applied field will affect the OOP field needed for nucleation in a different manner to those on the slanted sides, shifting the switching field. This shift depends upon the DMI in the samples. Since this method is based upon nucleation rather than propagation, the possibility of chiral damping affecting the measurements is removed; however, a lot of the difficulties of the bubble expansion technique remain, as well as the need to pattern the samples.

Chapter 4

Sample deposition and characterisation

In this, the first of the experimental chapters, the link between the growth and the structural and magnetic properties of Pt/Co/Pt is explored. X-ray diffraction shows the samples to be epitaxial, whilst X-ray reflection allows the interfacial disorder to be measured. In the range of substrate temperatures during deposition from 300°C to 100°C, a peak is seen in total interface disorder, at around 250°C, due to competition between increasing intermixing with increasing temperature and decreasing roughness at high temperatures. The coercivity is seen to increase with deposition temperature whilst the saturation magnetisation and anisotropy remain constant for the standard deposition, varying the Co/Pt bilayer from hotter deposition to colder. Varying only the top Pt layer or reversing the deposition temperature order causes the anisotropy to increase with deposition temperature, an effect removed if both are done simultaneously.

4.1 Introduction

Of all the multilayers that can exhibit magnetisation out of the plane of the film, those with Pt/Co layers have been amongst the most studied[32, 33, 26, 99]. There are several reasons for this, as discussed in the literature

review (section 2.1), including their close lattice constant agreement, their high perpendicular magnetic anisotropy (PMA) and Pt's high spin-orbit coupling (SOC)[100, 101]. In recent years, these properties, particularly the latter two, have led to studies focussed on the potential for narrow domain walls and very fast current-induced domain wall motion[102, 70].

Their close lattice parameters (0.5% lattice mismatch[103, 104]) allow epitaxial samples to be grown, particularly when using an Al_2O_3 substrate (1% lattice mismatch[105]) to provide the initial crystallographic orientation. This means that atoms on each layer match with positions of those on the layer beneath, providing a nearer-to-model system with fewer grain boundaries than polycrystalline samples, hence they have been the main focus in this project. Being a single element, Co also removes some of the complications that an alloy ferromagnet can raise, such as a change in concentrations from diffusion.

The PMA in the bilayer is due to the Pt 5d electron orbitals hybridising with the 3d orbitals of Co at the interface[39, 33, 106, 107], which brings the magnetisation out of the plane of the sample for thin enough Co layers[108]. The resulting perpendicular domains have thinner domain walls than those in the plane of the film and are in Bloch or Néel formations, or a superposition of the two. In the last five years, Pt/Co has gained even more importance with the realisation of the role that the Dzyaloshinskii-Moriya interaction (DMI) plays at the interface between ferromagnets and materials with high SOC[109], such as Pt/Co[110, 111, 25]. DMI can determine the structure of the domain walls, as well as affecting how they behave under driving forces, such as external magnetic fields and currents. The potential for epitaxy enables these effects to be studied and linked to crystal structure and interface morphology, as has been done here.

The epitaxial growth is building on work performed by Andrei Mihai [55] but has been expanded to cover a larger set of samples and a wider deposition temperature range. We add here a study of the interface morphology, and in Chapter 5 measurements of the DMI in Pt/Co/Pt.

4.2 Sputtering gun stability

It was found during this project that the stability of the plasma is linked to the base pressure; an effect not much discussed in literature, if at all. As the base pressure varied in the chamber between growth runs, the working gas pressure or gun power needed to be adjusted to maintain a stable plasma. In a growth with a lower base pressure, the plasma was less stable, needing a higher working gas pressure, as seen in Fig. 4.1. The effect was almost negligible at high base pressures, though this is likely due to the method that a minimum working pressure was used and was changed (increased) only if the plasma lost stability. At low base pressures, the effect became more pronounced, though with considerable spread and a distinct outlier showing that, as expected, more factors were affecting the plasma stability than just the initial base pressure. The effect could be explained by the contaminants in the chamber slightly decreasing the resistance of the Ar working gas to ionisation. It was seen that, whilst the plasma's stability during deposition changed, the stability during the presputter remained almost constant. The differences between these two scenarios were the elapsed run time at which each occurred and the position of the shutter wheel. The shutter wheel only had the sputtering aperture over the gun during deposition, giving the plasma and sputtered atoms more freedom of movement, as well as introducing an additional magnetic field which distorted the plasma. The deposition also occurred after the presputtering, by which point the base pressure had decreased beyond the initial value due to gettering. If chamber temperature had an effect on the plasma, it was below noise in this study.

4.3 X-ray characterisation

In order to assess how varying the growth parameters affected the structure, a technique was required to probe the samples' interiors. Ideally this technique should be non-destructive such that the sample may be used for further study. Since the growth parameters varied subtly between growths (or not so subtly in the case of base pressure), and even within one vacuum

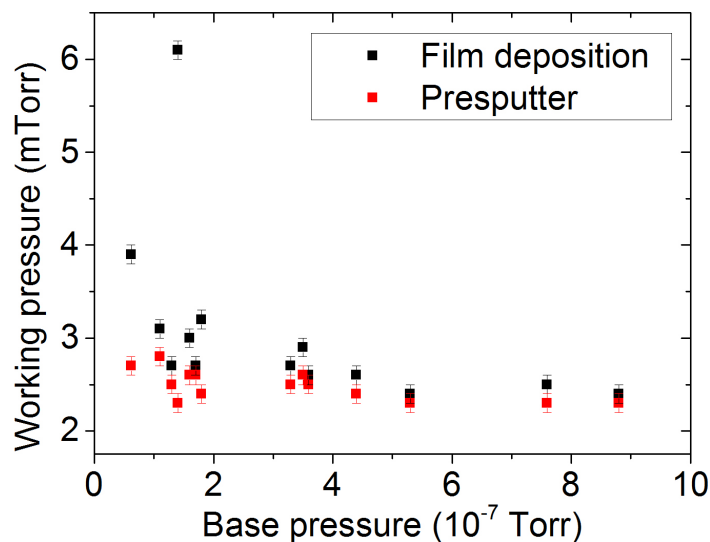


Figure 4.1: The working pressure used for a stable plasma for a given initial base pressure, both when depositing and when presputtering.

cycle nominally identical samples differed from each other, the characterisation had to be sample specific. A technique fulfilling these requirements is the use of electromagnetic radiation in diffraction or reflection, as discussed in the methodology (section 3.3), with radiation in a specific X-ray regime being chosen due to its wavelength ($\lambda_{\text{CuK}\alpha} = 0.154 \text{ nm}$) being of a similar length scale to the lattice constants of the film. This similarity allowed diffraction from the crystal at discernible angles. This is a technique widely used in thin film characterisation[89, 112, 113], particularly in multilayers where the interfaces are important.

4.3.1 High angle X-rays

Initially, high-angle scans were taken to assess the crystal orientation within a sample from set type A, Pt/Co/Pt, as shown in Fig. 4.2. Two sharp, very high-intensity peaks were seen at around 41.7° and 90.7° in 2θ which were from the highly-ordered substrate. It could be seen that these had double peaks, coming from the use of both $\text{CuK}\alpha_1$ and $\text{CuK}\alpha_2$ wavelengths. In order to remove this effect, a 4-bounce monochromator may be employed

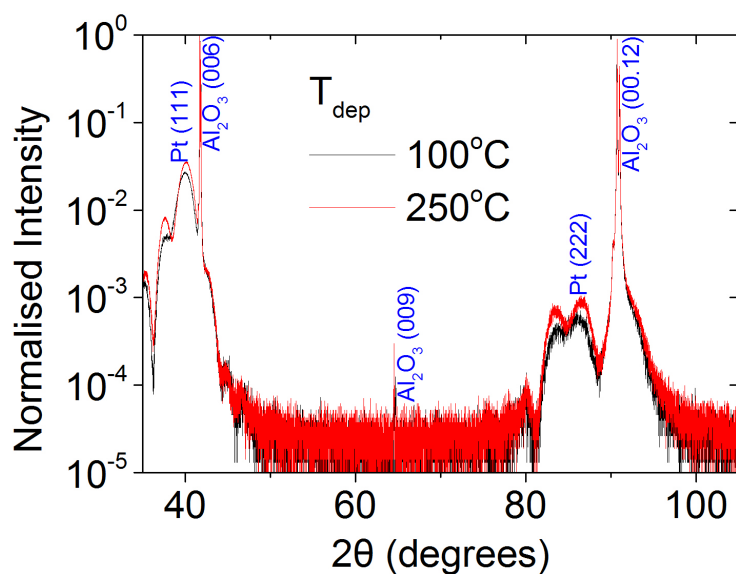


Figure 4.2: High-angle X-ray diffraction scans of Pt(30 Å)/Co(7 Å)/Pt(10 Å), deposited at 100°C and 250°C.

which bounces the emitted radiation between crystals four times, removing one of the wavelengths (usually $\text{CuK}\alpha_2$) through destructive interference. Such a monochromator was used in about half of the X-ray measurements undertaken, but the difference seen in the samples used in this project was minimal. One could also see the usually-forbidden (0009) peak from the sapphire substrate at $2\theta = 64.5^\circ$ due to multiple reflections[114].

As expected from literature[115, 107], the Pt (111) and (222) peaks were clearly visible near the substrate peaks. They were wider and less intense than the substrate peaks due to the Pt layers being a lot thinner and possibly less ordered. Another consequence of multiple reflections are the Kato fringes seen centred on the substrate peaks[116]. These are analogous to the Kiessig fringes seen at low angles and are caused by reflections off the interfaces between layers. The fringes on the lower-angle side of the Pt peaks were seen to be of anomalously high intensity, especially for the (222) peak. This was most likely due to a slight discrepancy in crystal axis matching between the seed and top Pt layers, caused by the separation due to the Co

layer. This could lead to a deviation from the standard lattice spacing of 226.5 pm[117], and so a different angle of diffraction. The higher-angled Pt (222) peak came from a lattice spacing of 224.8 ± 0.4 pm and 226.1 ± 0.5 pm for the sample grown at 250°C and 100°C respectively. Similarly, the lower-angled Pt (111) peak led to a spacing of 224.6 ± 0.4 pm and 225.5 ± 0.4 pm for the sample grown at 250°C and 100°C respectively. Thus both samples had lattice spacings smaller than bulk Pt as they were conforming to the sapphire lattice spacing, with more relaxation seen in the sample grown at the higher temperature due to the enhanced atomic mobility. Due to the Co layer disrupting the structure, if one takes the two prominent Pt (222) peaks to be from the Pt layers on either side of the Co, there would have been a 3% and 2% lattice mismatch for the 250°C and 100°C samples, respectively, which is larger than the nominal mismatch between the Pt and Al₂O₃ (1%) and the Pt and bulk Co (0.5%). However, these values were skewed by the Kato fringes from the substrate and so were likely far closer to the bulk lattice spacings. Without simulations to model this, more accurate values were not available. It is possible that the Pt layers also contributed Kato fringes, as seen in work by Hatwar et al.[118], though the samples they used were polycrystalline superlattices of Co(0.3 nm)/Pt(0.8 nm) on glass so had more interfaces to contribute to the effect. The strain from the Co layers also explained why their (111) peak was shifted to slightly higher angles, as demonstrated by Mihai et al.[55] on epitaxial samples.

The Co peaks themselves were of such low intensity compared to the Pt[119], and at about the same angular position, that the Pt dominates and the Co peaks cannot be seen. No peaks other than those expected for epitaxial (111) Pt could be seen, however, leading to the conclusion that the samples were, indeed, epitaxial in nature.

4.3.2 Low angle X-rays

At low angles, the focus is shifted from the crystal structure to the layer structure of the thin film. The reflections from each interface interfere, causing Kiessig fringes, from which one can extract the layer thicknesses,

electron densities and interface disorder. This is done by fitting the data with a model of the system, in this case using Bede REFS[120]. Figure 4.3 A shows two typical examples of this fitting, in which there can be seen some discrepancy between the model and the data. There are several possible reasons for this discrepancy, one of which is that when fitting the data the model fell into a local minimum. If the barrier in goodness of fit is too large then the model stays in the local minimum and will not converge to a more accurate set of parameters. However, due to the size of the deviations, Bede REFS' tendency to overcome such obstacles and the deviations being of a similar nature for various scans, I felt this was unlikely. Furthermore, changing the starting parameters resulted in very similar outcomes. Another possibility is that the model itself, whilst reflecting the nominal structure of the system, was missing a key component of the actual structure. This is often due to an oxide layer forming or the disorder or alloying at the interface being greater than can be accounted for by the layers' interface disorder parameter. Both of these necessitate an additional layer in the model which brings more parameters into the fitting, allowing more degrees of freedom and decreasing the reliability of the existing parameters. Since addition of these layers into the model did little to improve the discrepancies, it was felt that a model with just the bare minimum of layers would give the most accurate interpretation. This then leaves the possibilities that the fitting process is too simplistic and further terms were needed to account for the discrepancy, or that there was an unforeseen extra layer which had not been tested in the model.

There can also be seen a difference between the scans of the samples at different deposition temperatures. The difference most easily seen is that between the angular separations of the Kiessig fringes, which is due to a slight change in overall thickness of the films between the samples. Whilst the difference in the scan is clear, the actual thickness change was minimal and, from looking at individual layer thicknesses, seemed to mostly come from the Pt, where constant thickness was less crucial than the Co. When looking at thickness changes across all samples, no trend could be found with any other parameter, emphasising the stochastic nature of sputtering

in such a chamber as used here.

Whilst it is theoretically possible to extract values of interface disorder, hereafter termed σ , layer thicknesses and electron density for the individual layers, in practice these values come with a high degree of uncertainty, especially with σ . This uncertainty can be reduced somewhat by considering the overall interface disorder in the structure, simplistically by taking an average for the interface disorder of the Pt/Co/Pt trilayer. This was done for all type A samples, and its variation with deposition temperature is shown in Fig. 4.3 B. There is a fairly well-defined peak at 250°C which was a result of competing high-mobility mechanisms. Initially, the increased mobility led to high intermixing of the layers at the interface, increasing the disorder. At high deposition temperatures the mobility was sufficient to allow the atoms to smooth out at the interface, decreasing the roughness sufficiently for the overall disorder to decrease. Above 400°C one can see a rapid increase in interface disorder, which was thought to be due to either a phase change or from intermixing becoming so severe that the thin Co layer tended towards a CoPt alloy. The latter could have been the reason for the former and was supported by analysis of the σ values for the individual layers. One sees a general increase of interface disorder about the Co, whilst the top Pt surface becomes more ordered, as seen in Fig. 4.3 (c). This would suggest that the intermixing was the main contributor towards disorder, with the roughness decreasing, since the top Pt surface was unaffected by intermixing. Since the individual layer analysis in this case was from only three samples for each temperature with sizeable spread of data it must be taken to be only indicative.

Though there are few cases in literature dealing with the effect of substrate temperature on Pt/Co growth (for example, Mathet et al.[26]), and none looking specifically at the interface quality, Belien et al.[121] have investigated these effects in Fe/Cr superlattices grown by molecular beam epitaxy. Interestingly, they report the opposite effect, with their minimum disorder, when grown on a Cr seed layer, in the same temperature regime as the maximum disorder found in this study. This minimum shifted if no Cr seed layer was used, however, indicating that the coincidence of the

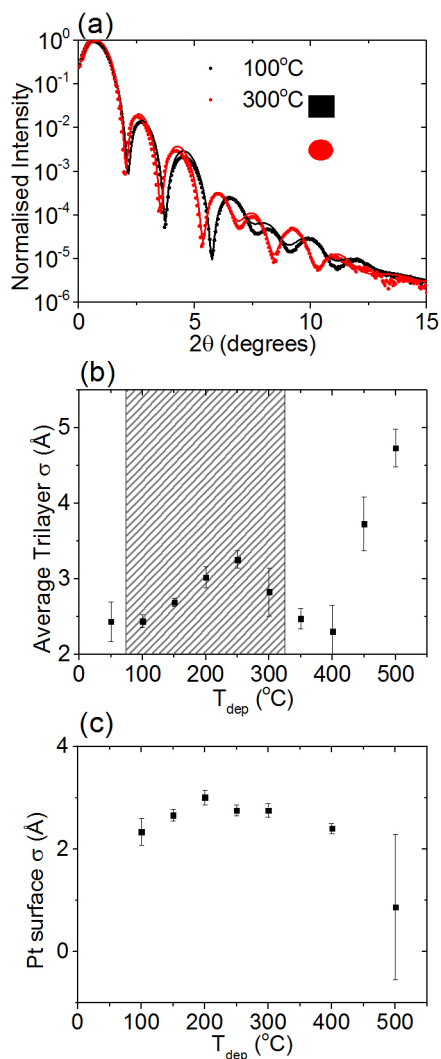


Figure 4.3: (a) Low-angle X-ray reflection scans and (b) the corresponding averaged disorder for set type A, Pt(30 Å)/Co(7 Å)/Pt(10 Å) deposited from high to low temperatures. The lines of best fit in (a) are from modelling the samples in Bede REFS and the shaded area in (b) is the main region of interest. (c) shows the sigma value for purely the top Pt surface. Error bars are from statistical analysis.

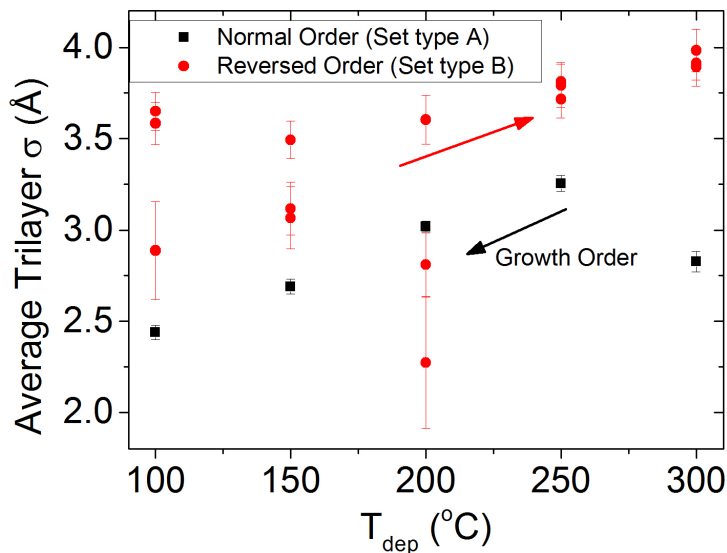


Figure 4.4: Low-angle X-ray reflection scans comparing set types A and B, Pt(30 Å)/Co(7 Å)/Pt(10 Å) deposited from high to low and low to high temperatures, respectively.

maximum and minimum was just that, a coincidence. Due to the differing material system and growth technique used, however, it was difficult to compare the two findings as the growth mechanics needed only to change subtly to bring about the changes seen.

To separate the contributions of T_{dep} and time of deposition, a sample batch of set type B was compared to those from A, Fig. 4.4. There was considerable sample spread in type B, especially at low temperatures, either from the stochastic nature of these growths or due to the fits being trapped in local minima. Nevertheless, the overall trend was that of an increase in average interface disorder with increased temperature, by a similar amount as for set type A. The σ values being higher than their set type A companions was believed to be due to the base pressure for that growth being towards the higher end of the scale (3.5×10^{-7} mTorr), together with the interface between the Pt seed layer and the Co being exposed for longer in the high temperature samples. Towards the lower temperatures there appeared to be a split, with some samples following the almost linear trend, whilst others

tended towards higher σ values. The split could, again, have been from the stochastic nature of the growth, with subtle variations in substrate temperature, substrate cleanliness and growth environment, despite measures to counter these changes. When assessed over all samples, however, there was no noticeable trend above noise between the position of the sample in the chamber and its structural properties.

4.3.3 Rocking curves

Besides analysis of the top Pt surface disorder, another more reliable method of distinguishing between roughness and intermixing is the use of rocking curves. By varying ω (the sample angle) whilst keeping 2θ (the detector angle) fixed, the off-specular reflection can be seen, which is due to the roughness without a contribution from the intermixing. The typical form of this scan is a peak with shoulders as seen in Fig. 4.5 (a). If these data are modelled, one is able to extract quantities such as the overall roughness, the degree of roughness correlation between interfaces and the lateral roughness correlation length[122, 89, 113]. Since a key aspect of these models is related to the shoulders, they need to be well-defined to enable the extraction of accurate values. The shoulders in the data from samples in this project, however, were not sufficiently well-defined and so models were not adequate to describe the system. Nevertheless, by analysing the shape of the curves, overall values of roughness could be obtained.

Rocking curves were taken at the first and second Kiessig fringe maxima so as to have sufficient intensity for the shoulders to be above noise level; it was found that for the third fringe and higher no shoulders were seen or they were too weak for analysis. Rocking curve data taken at the first and second Kiessig fringe displayed pronounced Yoneda wings[123] as the angle of the incident or reflected beam passed through the critical angle for total internal reflection. It can be seen in Fig. 4.5 (b) that the full width half maximum (FWHM) of the diffuse area under the curves stayed constant which one would expect if the drop-off of the diffuse shoulders was dominated by the Yoneda wings, where the half maximum in FWHM was defined by half the

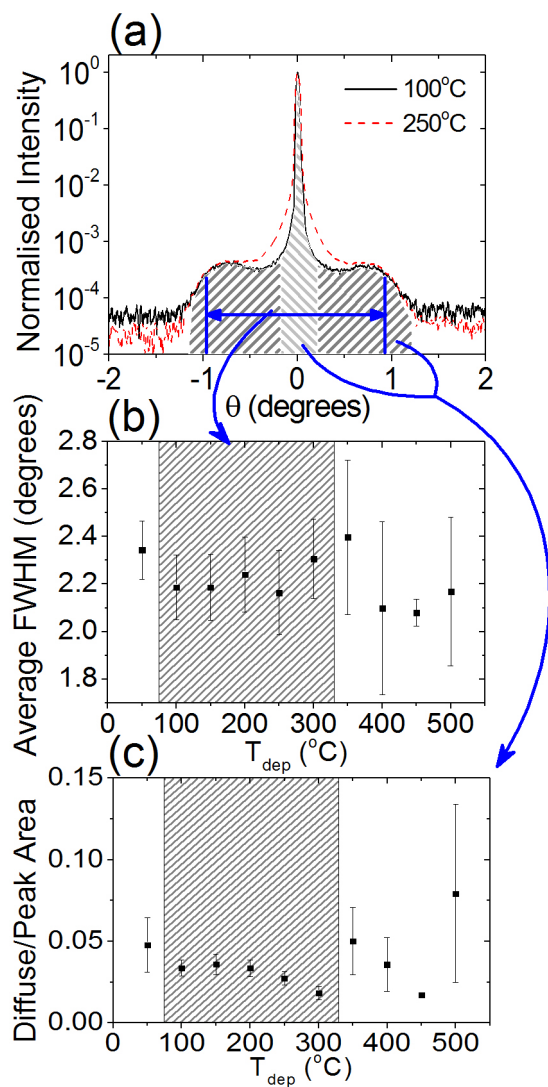


Figure 4.5: (a) Theta rocking curves on the first Kiessig fringe for set type A, Pt(30 Å)/Co(7 Å)/Pt(10 Å) deposited from high to low temperatures. (b) The extracted average full width half maximum and (c) the ratio of diffuse to peak area against deposition temperature, T_{dep} . The shaded section shows the main region of interest.

distance in the log scale between the plateau and the background. This was due to the critical angle for total internal reflection being dependent solely upon the refractive indices of the layers which should have remained fairly constant with deposition temperature, given the high quality of the films in the range studied[124]. The possible dip in FWHM at higher temperatures could have been from excessive intermixing changing the refractive indices. It is possible that the diffuse shoulders continued beyond the Yoneda wings seen in Fig. 4.5 (a), but they could not be seen due to lack of intensity or due to the sample horizon, which is where the sample rotates far enough that the source or detector effectively goes behind it. The scans came close to seeing beyond the wings at the first Kiessig fringe, but the intensity dropped to noise before this point was reached.

Besides the FWHM, another feature of X-ray rocking curves is the ratio of the area under the diffuse shoulders to that under the specular peak. This gives an estimate as to how the overall roughness varies between samples since, as the samples become rougher, more intensity is lost from the specular peak to the diffuse shoulders. Due to the lack of a fitting model, a quantitative value of roughness could not be reliably obtained, but the trend between samples was nevertheless quite clear, at least in the main region of interest. As the deposition temperature was increased, the sputtered atoms gained more mobility, allowing them to settle into smoother layers, decreasing roughness and decreasing the ratio of diffuse to specular as observed in Fig. 4.5 (c). Beyond the main region of interest, fewer samples were grown so, due to sample spread, there was a higher uncertainty associated with those data points. Consequently, whilst the trend appeared to change dramatically from that of the main region of interest, this could have been from an anomalous sample or sample batch and not represent the overall trend; especially since the jump at 350°C was not seen in other sample properties.

4.4 Magnetic characterisation

To assess the samples' magnetic properties, magnetic characterisation was undertaken. Since the magnetic properties can be very sensitive to layer

and interface morphology, they can be a practical tool to indirectly probe the film structures around the magnetic Co layer, although interpretation of results is often non-trivial.

4.4.1 Magneto-optical Kerr effect

A powerful technique for measuring magnetic properties of a sample utilises the laser magneto-optical Kerr effect (MOKE). This uses the change in polarisation of reflected laser light to assess changes in magnetisation over a wide area of a sample. When measured during a sweep of a magnetic field applied along the easy axis, magnetic hysteresis can be seen, from which the coercivity and exchange bias can be extracted. Analysis of the transition widths of the hysteresis loop also gives insight into the method of the magnetisation switching process.

The polar MOKE magnetic hysteresis loops in Fig. 4.6 were all centred on zero applied field, showing there was no exchange bias. This result was to be expected in a system with no break in symmetry for magnetisation in the direction perpendicular to the plane. The transition width of the loops normalised by the coercivity remained consistent within most of the region of interest, showing that the switching mechanism did not alter significantly. The loop for 250°C displayed slightly sharper switching, with a normalised transition width of 0.22 ± 0.05 compared with 0.4 ± 0.1 for the samples deposited at other temperatures. This indicated subtly faster magnetisation reversal, possibly linked to it being at a deposition temperature at the peak in interface disorder where annealing effects just started to dominate. The rounded corners indicated initial switching by nucleation of reversed domains, with the magnetisation gradually decreasing as the applied field increased beyond that needed for nucleation of reverse domains at progressively more nucleation sites. The steep sides of the loop indicated a rapid transition to switching by domain wall propagation within fields one fifth of the coercive field higher than are needed for nucleation. This was confirmed by wide-field Kerr microscopy as discussed later in Chapter 5. The coercivity was seen to increase monotonically with deposition temperature

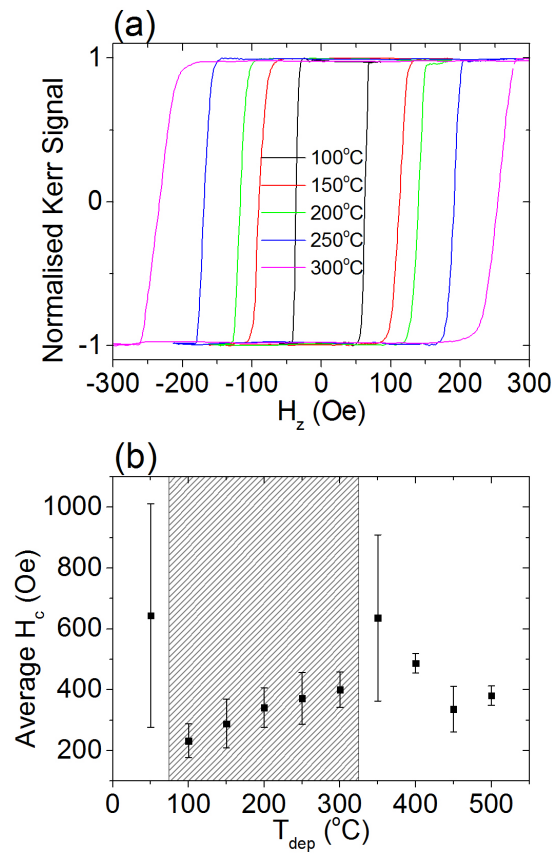


Figure 4.6: Polar magneto-optical Kerr effect hysteresis loops of sample set type A, Pt(30 Å)/Co(7 Å)/Pt(10 Å) deposited from high to low temperatures.

in the main range of interest, continuing up to 400°C. Above this point, the trend was less well defined, dipping at 450°C. These high- T_{dep} samples were outside of the region of reliable structural characterisation and so assessing how the trend was linked to changes in structure was beyond the scope of this project, however insight gained from Fig. 4.3 (B) allows postulation that such a trend was linked to the formation of a CoPt alloy. The trend up to 400°C could be understood by an increase in intermixing at the sample interfaces causing a higher number of pinning sites, but with nucleation sites with low switching fields being lost from annealing. Thus a higher field was needed to begin switching, and switching took place over a wider applied field range as the domain wall propagation was hindered, leading to an increased coercive field and more rounded corners.

If one compares these results to another method of structural alteration found in literature, that of ion irradiation, one sees a decrease in coercivity with interface disorder, as shown by Ferré et al.[125]. They considered the disorder induced by ion irradiation to be predominantly from intermixing, which would contradict the findings inferred in this project. One explanation is that the samples used by Ferré et al. were polycrystalline with thinner Co, which may well have changed the relative contributions of the different forms of disorder. The results in this project are supported by those of Mathet et al.[26], in which a higher growth temperature led to a higher coercivity in epitaxial Pt/Co films.

MOKE measurements can also be used as a gauge of saturation magnetisation. Whilst an absolute value cannot be obtained, the relative values can be extracted by looking at the change in Kerr intensity. This method relies upon the angles of the polariser and analyser remaining unchanged, with the polariser providing p-polarised light and the analyser typically between one and two degrees different in this case, and the samples being equally well aligned. Whilst these are reasonable assumptions when comparing samples of the same batch (measured in the same session), one cannot compare between batches due to the variability of the analyser. It was found that even within a batch, the overall Kerr intensity changed due to slight differences in sample alignment. Taking this into account by taking the change in Kerr

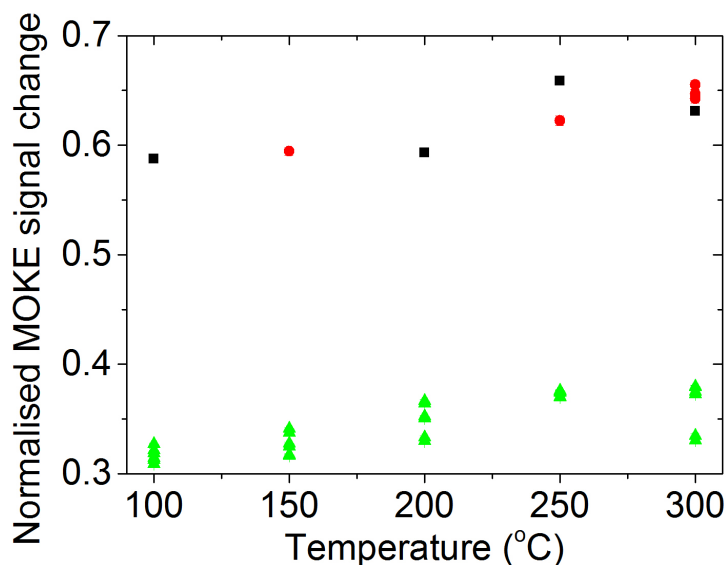


Figure 4.7: Variation between set type A samples with different deposition temperatures of the change in signal intensity using the laser magneto-optical Kerr effect. The change in MOKE signal between saturation of the magnetisation in each direction has been normalised by the average of the two signals. The colours represent samples from deposition runs, and so differed in base pressure.

intensity to vary proportionally with overall intensity, one sees in Fig. 4.7 an indication of a relatively constant value of magnetisation within each batch.

4.4.2 Anisotropy measurements

There are several methods available for extracting the effective anisotropy of thin-film magnetic samples. The simplest, perhaps, is to use the MOKE magnetometer to measure how the magnetisation changes with a field applied along a hard axis of the sample. The magnetisation along the hard axis should increase with field strength as the moments in the sample are pulled into alignment. At some field value, all the moments will be fully in alignment and the magnetisation will saturate. The field value at which this occurs is the anisotropy field. This method, however, relies upon the field being applied exactly parallel with a hard axis and of sufficient strength to

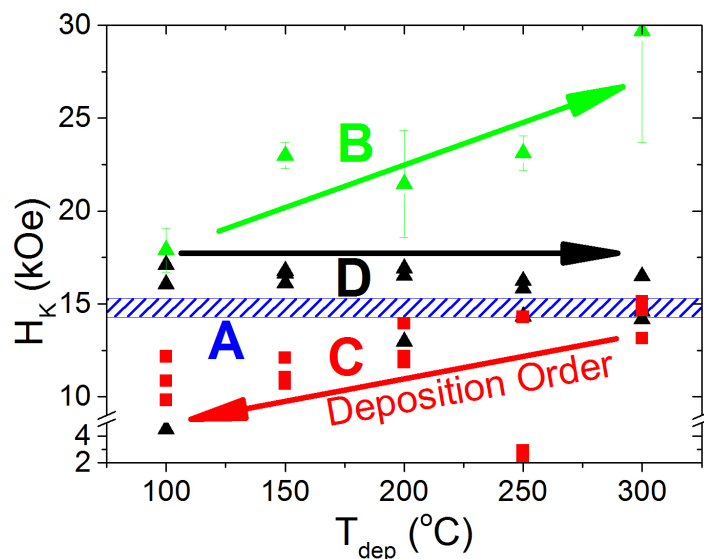


Figure 4.8: Anisotropy field data obtained from the AHE analysis method[95] for Pt/Co/Pt films with layers deposited at different temperatures, following the scheme outlined in Fig. 3.1.

exceed the anisotropy field. Most samples in this study were found to have anisotropy fields greater than one tesla, higher than the field available with the electromagnets used with our MOKE setup. An alternative is to use a vibrating sample magnetometer (VSM) to measure the magnetisation, with its superconducting magnets allowing much higher fields. However the low volume of sample meant signal-to-noise ratios were insufficient to extract reliable anisotropy field values. A third method is to use changes in the anomalous Hall effect (AHE) as an applied field is rotated around a hard axis[95]. Whilst this technique is indirect, it has the advantage that the applied field can be considerably smaller than the anisotropy field, as described in the methodology, section 3.5. The results of this are seen in Fig. 4.8.

For the majority of samples of type A (Co/Pt deposited as a function of decreasing substrate temperature), the anisotropy field remained confined within the range 14.7 to 15.2 kOe, as indicated by the shaded region in Fig.

4.8. The spread of values showed no trend when plotted against structural properties of the samples, showing that the cause of the spread was smaller than the limits of uncertainty or was due to structural properties not yet measured. Samples of type B (Co/Pt deposited as a function of increasing substrate temperature), however, showed an increase of anisotropy with substrate temperature, most likely due to a lower base pressure at deposition improving the order of the interfaces. The anisotropy field also increased with deposition temperature for samples of type C (top Pt layer deposited as a function of decreasing temperature) which, since the lower Co interface was nominally identical between samples of this type, showed that the top Co interface had a higher anisotropy field contribution at higher substrate temperatures. The final type, D (top Pt layer deposited as a function of increasing temperature), showed little change of anisotropy with temperature, seemingly because the annealing the samples experience cancelled out the improved order of the top Co interface. Thus these data showed that both interfaces contributed to the anisotropy of the sample, with the contributions being affected by both deposition temperature and annealing. The lack of individual substrate temperature control meant that effects from the deposition temperature could not be fully separated from effects due to the changing growth environment with time without annealing the lower temperature samples, however a new growth system is currently in development at Leeds which could allow this to be done.

Comparing with literature, Kim et al.[126] found an increase of anisotropy with interface roughness, though this was achieved via changing the deposition pressure in polycrystalline samples and the amount of roughness found exceeded that found in this project by up to a factor of five. Bandiera et al.[127] used annealing to affect all the interfaces in a polycrystalline Pt/Co multilayer and found the anisotropy to change little up to 300°C. Preventing intermixing through the use of a thin Cu layer increased anisotropy, particularly for thin Co layers, showing the effect of this type of interfacial disorder. Since the Co layer was very thin in the samples of this thesis, the annealing it experienced in set types C and D could have been far more effective at altering the interfacial anisotropy, possibly explaining the differences in

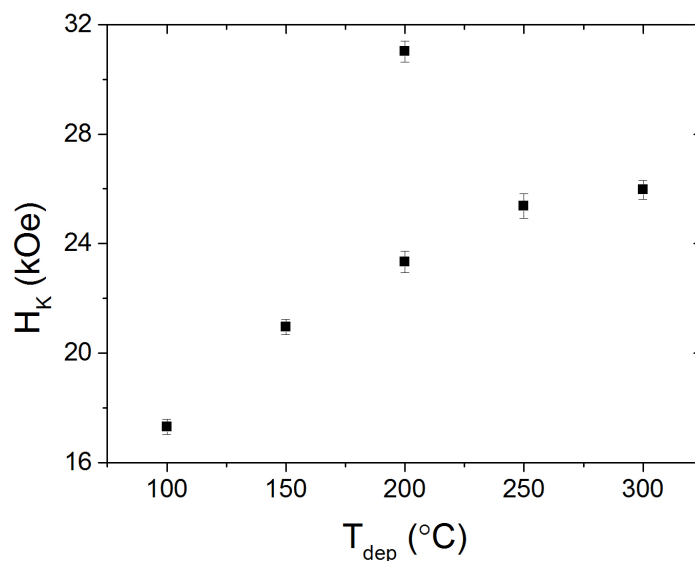


Figure 4.9: Anisotropy field data for the batch AW240815, taken using the AHE analysis method[95]. Samples in this batch were Pt/Co/Pt films grown on a substrate wafer cut in the labs, as opposed to pre-cut by the suppliers.

behaviour of anisotropy with deposition temperature. Alternatively, factors such as impurities could have been playing a significant role.

Sample batch AW240815, set type A, appears as an anomaly in this project, see Fig. 4.9. Its growth differed from other batches due to the substrate being cut from a wafer, rather than being received pre-cut from the supplier. To protect the substrate surface in such an operation it was covered in resist, and it is in the removal of such a layer that differences arose. Despite being cleaned in acetone and then isopropanol in a sonicator, it is likely that residual resist remained. This supposition is supported by the disorder in the Pt seed layer being larger in these samples than for other batches and led to trends in other properties that differ from the norm. Of particular interest was the far higher anisotropy fields compared with other set type A samples, which were likely as a result of greater intermixing at the interfaces[128], and the significant change with T_{dep} indicating that such interfaces were more sensitive to the growth temperature, possibly due to

a lower base pressure removing some of the effects of contamination or a smoothing out of interfaces by annealing of an initially highly disordered state.

4.4.3 Vibrating sample magnetometry

Whilst IP VSM MH (magnetisation against applied magnetic field) loops have proven too noisy for reliable extraction of sample anisotropy, OOP loops were still able to provide a value for saturation magnetisation, M_s . MOKE loops have shown that, within batches, M_s of samples varied little, but VSM enabled comparison between batches. Figure 4.10 shows comparison between example batches grown at a variety of base pressures. There was on the order of 10 μemu of noise and 30 μemu of drift associated with these measurements, emphasising their difficulty. Overall, however, the measurements tended towards the same value for saturation magnetisation ($90 \pm 10 \mu\text{emu}$, or $2.6 \pm 0.3 \text{ MA/m}$ in SI units), as expected for samples with nominally identical thicknesses of Co. This value was about twice those found elsewhere in literature for Co[2, 15, 129], however it did not take into account the induced magnetisation in the Pt layer, which can be substantial[130, 131]. Thus even though these scans could not be used to reliably provide the absolute saturation magnetisation of the samples, they still showed that the relative saturation magnetisation between samples was constant.

4.5 Sustainability

Following a cut of 40% of China's rare earth supply in 2010, the availability and sustainability of materials has become a more significant factor in research, especially where applications are the main concern. If supplies of a vital element run low or increase in price, the cost of an emerging technology could become prohibitive. Thus efforts have been made to ensure that materials used are from reliable sources. Material from less stable regions of the world not only has a higher chance of suddenly becoming scarce, but also has ethical problems with unknown amounts of it coming from unregulated

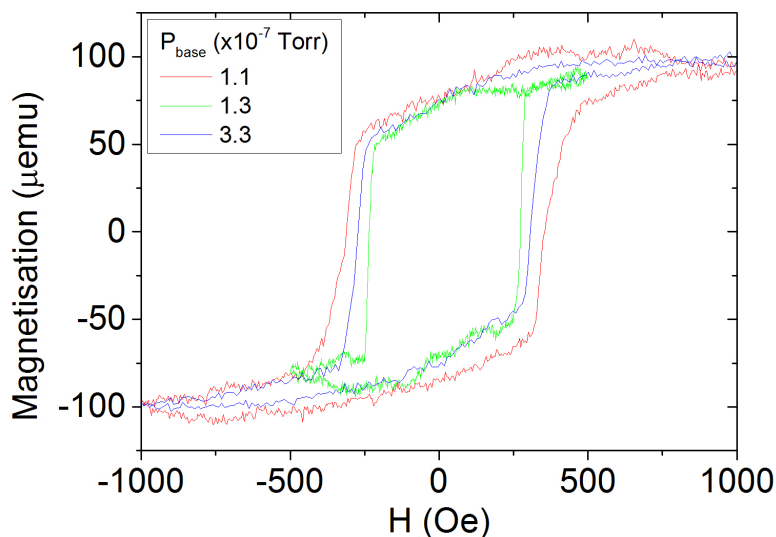


Figure 4.10: OOP MH loops of Pt/Co/Pt samples taken at 295 K using VSM.

mines. These damage the environment and can use forced labour.

Analysing the elements used in this project, aluminium has a low supply risk, coming mainly from Australia and Brazil, whereas cobalt, platinum and iridium have riskier supply lines. Platinum and iridium are mainly mined in South Africa and Russia, which are fairly stable, but are of low abundance. Manganese is of high enough abundance that, whilst it comes mainly from China and South Africa, it has a lower supply risk. The most concerning element is Co, coming mainly from the Democratic Republic of the Congo (DRC) and China, both known to have unregulated mines and with a very low political stability in the DRC. The use of Co may cause future problems unless an alternative source is found; however, for the properties needed, there is very limited choice.

4.6 Conclusions

In this chapter, the growth and subsequent characterisation of epitaxial Pt/Co/Pt samples were investigated, with the focus being on using sub-

strate temperature during deposition to affect the samples' interface disorder and, hence, magnetic properties. Throughout the range of substrate temperatures used, the sample was seen to remain epitaxial in nature, without excessive alloying. The overall interface disorder was seen to change with deposition temperature, peaking at 250°C, with a significant rise in disorder for samples grown above 400°C. When grown in reverse order, from the colder to the hotter samples, an increase in disorder with temperature was seen up to 300°C, albeit with significant spread at the lower temperatures. Using X-ray rocking curves of the standard-order samples, the roughness was seen to be steady for lower temperatures, decreasing above 200°C, indicating that an increase in intermixing, followed by a decrease in roughness was responsible for the peak in overall interface disorder.

In terms of magnetic characterisation, the coercivity steadily increased with deposition temperature in the main temperature range of interest, akin to the inferred behaviour of intermixing. The anisotropy, however, was seen to remain roughly constant for the standard sample type, as well as for samples with only the top Pt layer deposition varied, in an order from colder to hotter. For samples with either only the top Pt layer deposition temperature varied in the standard order, or both Co and Pt layers varied in reversed order, the anisotropy was seen to increase with deposition temperature; indicating that both interfaces contributed to the anisotropy, but were affected differently from the post-growth anneal to which the reversed-order samples were subjected. Both MOKE measurements and VSM measurements indicated that saturation magnetisation was constant between samples. Finally, sustainability was looked into, with Co being found to be of concern due to low political stability of the DRC government.

Chapter 5

Magnetic field-induced domain wall motion in Pt/Co/Pt

This chapter builds on the characterisation work in Chapter 4 to assess how the structural properties of the samples affect their net Dzyaloshinskii-Moriya interaction (DMI). This was done by measuring the domain wall velocity of expanding bubble domains under applied magnetic fields. The resulting velocity data were analysed with respect to three possible models, with the most basic being sufficient to describe the standard parabolic velocity-field graphs acquired. The extracted DMI field values were seen to have moderate linear correlation with the relative disorder of the top and bottom Co interfaces, indicating that the DMI contribution is highly sensitive to the interfacial disorder. Upon increasing the deposition temperature, one saw an increase in the DMI field which, when combined with the link between deposition temperature and interface disorder found in the previous chapter, indicated that the deposition temperature was affecting the levels of disorder at either Co interface differently. A high base pressure during deposition, however, was seen to reduce this effect dramatically. This opens the possibility of being able to control the net DMI in this nominally-symmetric structure by varying the deposition temperature, at low enough

base pressures.

5.1 Kerr microscopy

A consequence of growing epitaxially is that samples are inclined to have few defects; that is, points in the film where the atoms do not conform to the regular pattern, be it from strain, vacancy or impurity. This high level of order allows domain walls in the thin magnetic layer, once nucleated, to propagate smoothly, not hindered by severe grain boundaries. Defects and dislocations still occur, however. The former can be useful, if sufficiently dispersed and of sufficiently deep potential, as the disruption to the crystal lattice can reduce interfacial coupling, and hence the anisotropy, and so act as points of nucleation. The latter, though, defined as lines of disorder along the sample plane, can become very disruptive if the dislocation density is sufficiently large, since then severe pinning can occur[132, 133], acting as a barrier to further propagation. Due to the nature of sputtering there will be many smaller defects, causing wells in the potential landscape too shallow to act as nucleation sites, but in which domain walls can be pinned. For a low driving force, the wall moves by hopping from one site to the next, a method of movement in the velocity range known as the creep regime[40]. It is this regime which was the focus of this analysis.

5.1.1 Domain wall velocity measurement

The main method for extracting domain wall (DW) velocity in these samples was via bubble domain nucleation and propagation. The largest obstacle in this method is finding a reliable nucleation point that satisfies several criteria: it must consistently nucleate a bubble domain of an approximately constant size given a magnetic field pulse of fixed strength and duration; it must be in a homogenous environment, so should expand symmetrically under a pure out-of-plane (OOP) field without hindrance from sites of weak anisotropy, such as due to strain from substrate roughness or thickness variation; it must be far enough from other nucleation sites that the domain can

expand without colliding into another reverse bubble domain. The first criterion can be relaxed such that a reversed domain is nucleated at least half the time, with the pulse varying in length to give the approximate size. The second is more stringent, although some hindrance of the walls expanding perpendicularly to the applied in-plane (IP) field was allowed so long as it was far enough from the parallel-to-field expanding walls to not affect them. This was because the majority of analysis was performed on the parallel-to-field expanding walls. Similarly if the third criterion was not met for the perpendicular-to-field expanding walls, then this too was allowed.

To enhance the reliability of image analysis, where possible the contrast of the Kerr microscope was set such that the bubble domain saturated the difference image. Thus, by searching for saturated (white or black pixels), my python program was able to calculate how far the bubble domain had expanded. For samples with IrMn atop the Co, as seen in Chapter 6, the contrast change was lessened, leading to less clear definition of the distance moved (see Fig. 5.1). Despite this, the extraction program was able to accurately ascertain the contrast changes for most measurement lines, mostly due to averaging of the surrounding area.

5.1.2 Magnet Design

In order to have both in-plane and out-of-plane magnetic fields applied to the sample for the bubble domain expansion experiments, an additional magnet needed to be added to the setup. Since a larger field was required in the IP direction than OOP, the IP electromagnet that came with the kit was retained and an OOP electromagnet was designed. The specifications were that it needed to fit between the coils and pole pieces of the IP magnets, provide a sufficiently large field to nucleate and propagate domains in the sample and support the sample without affecting it. After moving the IP pole pieces back such that they were flush to the IP coil housing, the OOP coil could be at most 5 cm in diameter. A previous coil had been made for such conditions, however whilst it fulfilled the first two conditions, at the fields needed for the samples in this project it tended to overheat and

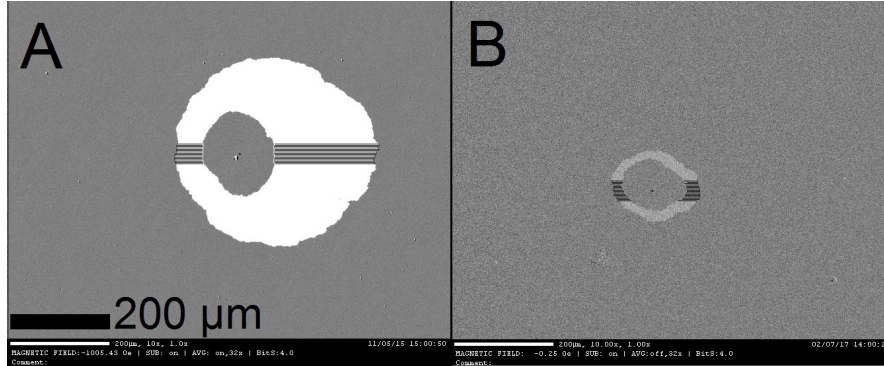


Figure 5.1: An example of contrast in difference images from Kermit, the Kerr microscope used in this project. A is from a standard Pt/Co(0.7 nm)/Pt(3 nm) sample where the contrast saturates the display range. B is from Pt/Co(0.7 nm)/IrMn(2 nm)/Pt(5 nm) at optimal contrast. The horizontal black lines represent the measurements of domain wall movement made on the image by the extraction program, as described in Section 3.7.2.

there was a noticeable temperature change of the sample, seen by increased domain wall velocities. Thus the design was replicated but with the inside of the coil housing hollowed out and water-cooled, as displayed in Fig. 5.2. Calculations performed on the heat generation and field strength allowed optimisation of the wire width to the available power supply. After fabrication, it was found that the water-cooling system was highly effective with no change seen in temperature at the position of the sample, even at high powers. At such powers, however, the heat from the outer coils could not be adequately conducted inwards to the cooling system, despite the coating of thermally-conductive varnish on each layer of wire coils. This meant that running the coil at high power for a long duration could damage it and so the maximum sustainable field that it could output was 300Oe, still sufficient for most Pt/Co/Pt samples.

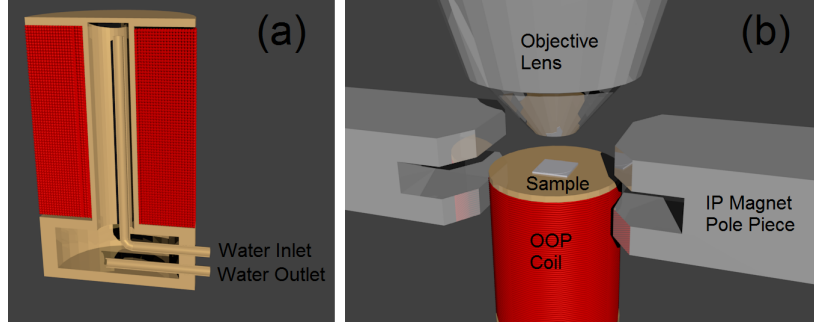


Figure 5.2: (a) A cross-section of the water-cooled homebuilt out of plane (WHOO) coil. The red sections are the cross-sections of the wire coils. (b) A schematic of the WHOO coil and in-plane electromagnet positions in relation to the sample and Kerr microscope.

5.2 Creep Regime Test

In order to use the creep regime model, first it must be confirmed that the field used to propagate the domains is in the creep regime. This follows the model set down earlier, Eq. 2.2, linking domain wall velocity, v with OOP field, H_z , and domain wall energy density, ϵ . By taking measurements with no IP field, ζ simplifies to ζ_0 and provides a simple way to extract ζ_0 and v_0 . Thus for the model to hold, there must be a linear relation between $\ln(v)$ and $H_z^{-1/4}$.

Figure 5.3 shows this linear relationship, and so confirms that the creep regime held over a wide range of OOP fields, with parameter values similar to those found by Lemerle et al.[52] in high-quality polycrystalline samples. For most of the study, the OOP field pulse strength was kept constant for each sample, at a value near the centre of the tested region. Since the IP field would be varied in the measurements of DMI, the OOP field was also varied with a constant IP field applied, and the logarithm of the velocity was found to vary linearly with $H_z^{-1/4}$, as seen in Fig. 5.4, indicating that these values of H_z are still in the creep regime. The extracted values of v_0 and ζ were found to be: 24.30 ± 0.06 m/s and $(4.412 \pm 0.007) \times 10^{-20} \text{T}^{1/4}$ for no IP field; 24.24 ± 0.07 m/s and $(4.354 \pm 0.009) \times 10^{-20} \text{T}^{1/4}$ for an IP field of

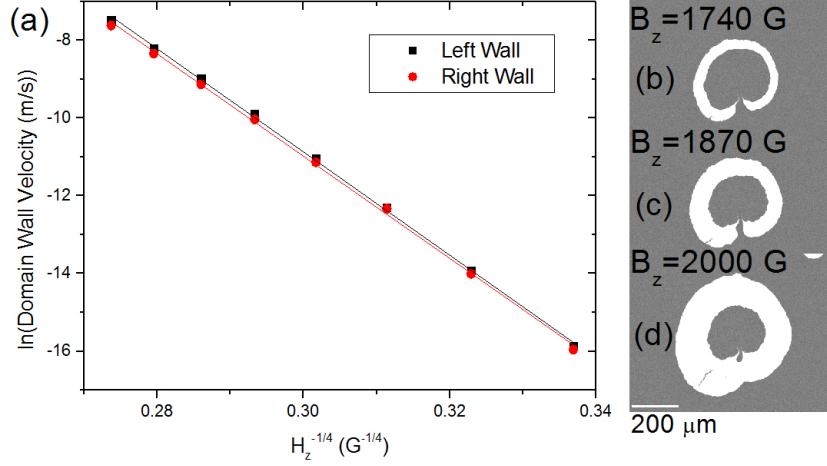


Figure 5.3: The relationship between domain wall velocity and OOP field with zero applied IP field. The linear relationship seen is consistent with motion in the creep regime.

300 Oe in the direction of DW propagation; and 23.2 ± 0.3 m/s and $(4.17 \pm 0.03) \times 10^{-20} T^{1/4}$ for 300 Oe antiparallel to the DW propagation. These showed that, in the range of IP fields used, the characteristic velocity, v_0 , stayed constant whereas the scaling constant, ζ , varied. This agreed with the theory, since the ζ is dependent on H_x via the DW energy density, whereas v_0 is dependent upon the pinning site density and attempt frequency, neither of which are explicitly linked to H_x . The characteristic velocity has been shown to vary with IP field[134], but at field values higher than necessary to find the DMI field. The difference in ζ with regard to the DW propagation direction is an indicator of the asymmetry induced by the DMI, and the overlap between data when the DW propagation direction and the applied IP field direction were reversed shows that the system had been correctly aligned.

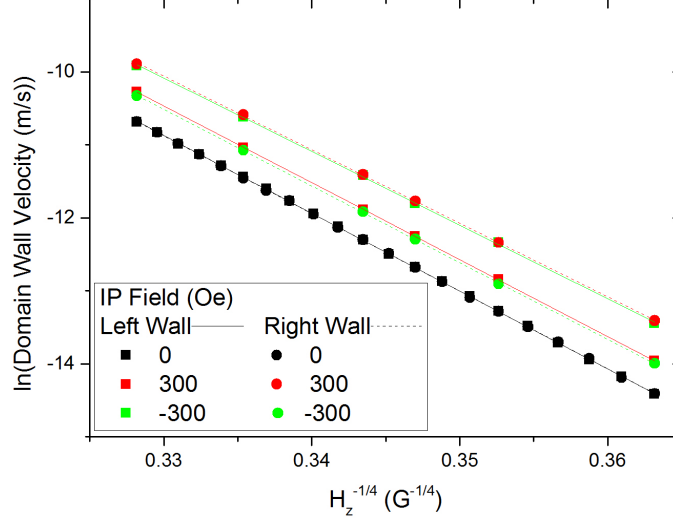


Figure 5.4: The relationship between domain wall velocity and OOP field with varying IP fields.

5.3 In-plane field dependence of domain walls velocity

Since the DMI appears as an asymmetry in the domain wall energy density, in order to ascertain a value for it, the domain wall energy density must be altered. The simplest way to do this is by applying an IP field to bring forth the asymmetry in the domain wall structure. The effect on the velocity of the domain walls due to an applied IP field is seen in Fig. 5.5. Under a constant IP field, the distance covered by the domain walls when propagated by an OOP field pulse can differ greatly between the left- and right-moving domain walls, shown in Fig. 5.5 (a) to (d). When measured under a variety of IP fields, the asymmetry became clear. The data in these graphs formed uniform parabolas, as expected from Eq. 2.2. A slight kink in the gradient on a logarithmic scale was seen at the applied IP field needed to fully stabilise a Néel wall structure. An asymmetric shift of minima was seen for the oppositely-moving DWs in samples deposited at high and low temperature, with the shift being in opposite field directions.

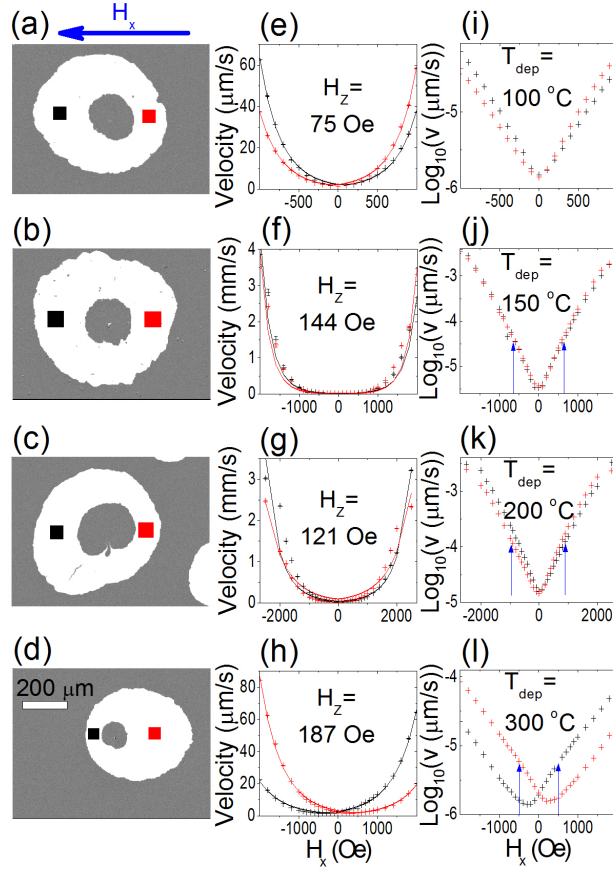


Figure 5.5: (a) to (d) Differential mode Kerr microscope images of bubble domains used to determine domain wall displacements in a field of $H_x = -1000$ Oe, for a set of Pt/Co/Pt films grown at low base pressure (1.1×10^{-7} Torr) and deposition temperatures indicated for each row. (e) to (h) DW velocities fitted by Eq. 2.2, and (i) to (l) the logarithm of DW velocity, as a function of H_x . H_z is the out-of-plane pulsed field used to expand the domain. Black and red correspond to the left- or right-moving wall of the domain, respectively, and the blue arrows indicate the domain wall anisotropy field.

5.4 Analysis models

DW velocity vs applied IP magnetic field data can vary drastically from the symmetric parabolas most commonly seen in the absence of DMI, with some extreme examples demonstrated particularly well by Lavrijsen et al.[19]. It is for this reason that several models have been created to explain these deviations. The basic model modifies the DW energy density based on its configuration, the universal creep law model empirically unifies the creep-depinning transition amongst all material systems and the rough wall model deals with how variations in the DW direction affect its energy density.

5.4.1 Domain wall energy variation model

This model, as compiled by Je et al.[18], modifies the basic creep law by including the effect of an IP field on the domain wall energy, as shown in Section 2.2.1. Since the DW energy determines how easily a pinning site can be passed, the depinning energy in the exponent is multiplied by a ratio of the DW energy with an applied IP field to that without an applied IP field. The domain wall energy is then modelled as a change from the pure Bloch wall due to a perturbing IP field constituting the applied IP field and the effective DMI field. With no DMI, the DW energy, and hence the DW velocity, is symmetric about zero applied IP field. When a net effective DMI field exists in the structure, the velocity curve is offset from zero applied IP field, although the velocity is still symmetric about the minimum velocity. This was seen to describe most data for Pt/Co/Pt samples very well, as seen in Fig. 5.5 and in the appendices, Fig. A.1. Data from samples of each deposition temperature subscribed to the basic parabola, indicating that the majority of the physical mechanisms were being described by the model. The shift in applied field value of the minimum was small for samples grown at 150°C and 200°C, and larger for those at 100°C and 300°C, though in opposite directions. This showed that as the deposition temperature increased, the net DMI moved from a negative value, through negligibility, to a positive value.

The agreement between the model and the data for Pt/Co/Pt was brought

about with, for most fits, two free parameters, in Eq. 2.2. The saturation magnetisation and exchange constant were taken from literature as 1.1×10^6 A/m and 16×10^{-12} J/m respectively [2, 40, 129]; and the characteristic velocity, v_0 , and the scaling constant, ζ_0 were taken from fits of the DW velocity against OOP field. This left just the effective anisotropy and the effective DMI field as fitting parameters. In this model, the effective anisotropy controls the DW energy of a Bloch wall, as well as (inversely) the amount to which the energy changes with IP field. The effective DMI field solely controls the shift of the curve along the IP field axis- the only asymmetry between oppositely moving DWs seen in the model.

There was, however, a discrepancy between the value obtained for the effective anisotropy from fitting this data and the value obtained through other measurements by up to a factor of seven, the measured being larger than those from fits. There could have been several reasons for this disparity, the first being the region that was being measured. Most measurements of the anisotropy of the sample were taken over the entire sample, whereas the values from model fitting were taken at the domain wall via its movement through the sample. If there was a significant variation in anisotropy across the sample then it is likely that nucleation would have occurred more readily at sites of lower anisotropy, biasing the anisotropy from the fits towards lower values. A second reason could have been from a change in local anisotropy from the formation of the domain wall itself, although the overall effect should have been too small to make such a difference. Thirdly, the applied IP field could have had some small effect, although at its maximum its magnitude was at most a quarter of that for the measured anisotropy field and so any change from domain tilting should have been negligible. Finally, there was some possible disagreement between saturation magnetisation values obtained from VSM to those expected from literature. This has been attributed either to a neglect of the induced magnetisation in the Pt, or to miscalibration of the VSM for samples such as those used here. The saturation magnetisation was needed to convert the measured anisotropy field to the anisotropy energy obtained from the fits. Even if the measured saturation magnetisation value were accurate and used, it still could not have

explained the decreased value of anisotropy from the fits, however, because the saturation magnetisation values measured would have led to even lower anisotropy field values.

Ultimately, since the anisotropy does not affect the asymmetry, the values obtained for the effective DMI field should still have been accurate within the model. This did, however, throw doubt upon the validity of the model, and could mean that the effective DMI field values may not simply be taken from the minimum in DW velocity if there are other contributors to the asymmetry.

5.4.2 Universal creep law model

Recently, a modification to the creep law has been proposed[57] which aims to unify all creep motion to a universal model. As described in Section 2.2.3, this involves changing the exponent such that at low fields it approximates to the usual creep law, but at fields approaching the depinning field, H_d , the energy term vanishes. The proposed model for DW velocity is thus

$$v(H, T) = v_0(H_d, T) \exp[-\Delta E / (k_B T)] \quad (5.1)$$

with

$$\Delta E = k_B T_d [(H/H_d)^{-\mu} - 1] \quad (5.2)$$

where H is the applied magnetic field, T is the temperature of the system, v_0 is the characteristic velocity, H_d is the depinning field, T_d is the depinning temperature and μ is the creep exponent, usually taken to be 1/4. It is the addition of the -1 term in ΔE which separates this model from the basic creep law; however, since that term does not depend on H it can be absorbed into the characteristic velocity, giving a modified characteristic velocity of

$$v_1 = v_0 \exp[E / (k_B T H_d^{1/4})]. \quad (5.3)$$

Previously it has been seen that both the DW energy and characteristic velocity change with high IP fields[134]. The DW energy is expected to

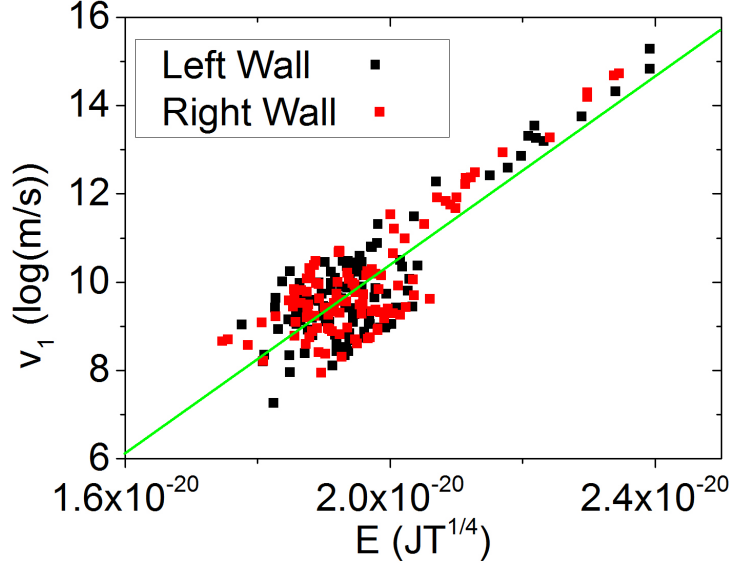


Figure 5.6: The dependence of the modified characteristic velocity on the exponent, from Eq. 5.3. The green line represents a line of best fit.

change, but not so for the characteristic velocity. With the modification of this model, it is clear to see that the modified characteristic velocity depends upon the DW energy and so should also change with IP field. To test this relationship, one can plot the modified characteristic velocity against the DW energy term, both extracted from experimental data, as shown in Fig. 5.6.

Figure 5.6 shows a linear dependence of v_1 with E , though with bunching of points towards the lower E values. Upon investigation, it appeared that the bunching was from one direction of applied IP field which, from symmetry arguments, led to the initial conclusion that, despite efforts otherwise, there existed misalignment of the IP field with respect to the sample. This would have the effect of introducing an addition to the OOP field, shifting the value of v_1 , but not altering E . This shift would depend upon the IP field, and so whilst it is feasible to think that the misalignment exactly cancelled any change in v_1 , one would expect the value of E to change with IP field as per normal, leading to a linear, flat dependence in Fig. 5.6. Thus,

no explanation for the lack of E dependence on IP field for just one direction of IP field was readily apparent.

Looking at the section of Fig. 5.6 with significant change in E, the trend was linear in the semi-log scale, in keeping with the model. Thus by taking the gradient of this line, $1/(k_B T H_d^{1/4})$, one could find the depinning field of the sample, H_d . In this case, H_d came out as 26 ± 4 Oe, which was far too small, as one can see from Fig. 5.3 and 5.4. This could be due to the model making assumptions which were not applicable for this system, although none are apparent, except for those unknown factors that are causing the bunching of points for one direction of IP field, or from H_d changing with IP field, meaning that extraction of H_d from this method was not possible. One way to test this was to increase the OOP field until the DW velocity no longer subscribed to the creep regime at various IP fields, however, even at the highest OOP fields attainable from the equipment, 300 Oe, the Pt/Co/Pt systems maintained their conformation to creep regime behaviour. Comparing the H_d value from this project to that estimated by Diaz Pardo et al.[135] for polycrystalline Pt/Co/Pt thin films at room temperature, 57 mT, it was found to be about a factor of twenty smaller, further indicating that in these samples, H_d could not be taken as a constant with respect to applied IP field.

5.4.3 Rough wall model

It is clear from DW images that, in most cases, they are not entirely smooth. Thus, even when taking a small arc of a bubble domain moving parallel to the applied magnetic field, there will be a variation in DW angle. This variation means that the effective DMI field (taken to be parallel to the DW normal) will deviate in direction from parallel to the applied field. As discussed in Section 2.3.2, Pellegren et al. [73] take this into account in their modified creep law model. This model modifies the DW energy term in the DW energy variation model as such:

$$\sigma = \sigma_{\text{basic}} + \sigma_{\Theta\Theta} - [\sigma_{\Theta\phi}^2 / \sigma_{\phi\phi}] \zeta(L/L_{\text{ex}}) \quad (5.4)$$

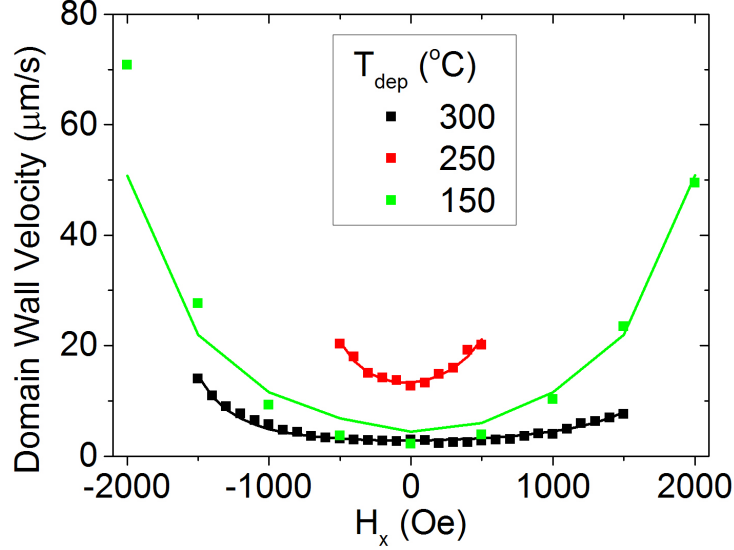


Figure 5.7: The extent to which the Sokalski model (solid lines) describes how the domain wall velocity varies with IP field (points).

where

$$\sigma_{\text{basic}} = \sigma_0 - \pi D \cos(\phi - \Theta) - \pi \delta \mu_0 H_x M_s \cos(\phi) + (\ln(2)/\pi) t \mu_0 M_s^2 \cos^2(\phi - \Theta) \quad (5.5)$$

and

$$\zeta(l) = 1 - (3/l^3)(l - \tanh(l)) \quad (5.6)$$

in which parameter subscripts refer to derivations with respect to those parameters, D is the Dzyaloshinskii-Moriya constant, Θ and ϕ are the azimuthal angles of the DW normal and internal magnetisation, L is the length of the DW segment and $L_{\text{ex}} = \delta \sqrt{\sigma_0 / \sigma_{\phi\phi}}$.

As one can see in Fig. 5.7, the model fitted well for one sample at 300°C, but deviated significantly for a sample at 150°C. This could have been down to the fitting procedure getting stuck in a local minimum, or from the model not representing the sample. To ascertain which, many more fittings were needed, however, due to time constraints, this was not possible. This came from the model needing to know the equilibrium magnetisation angle, which

was found numerically, meaning that the domain wall energy must be found for each angle of magnetisation direction, for each IP field, for each iteration of the fitting method.

5.4.4 Model Summary

Each of the three models presented have their advantages and disadvantages. The basic DW energy variation model is fairly intuitive, fast to fit and gave a good description of my data for low IP field strengths. Its main downside is the deviation of the data at high IP fields, showing that it did not entirely capture the physics of the situation, with the missing term, or terms, giving a larger contribution at higher IP fields.

The universal creep law, whilst encapsulating the behaviour of multiple systems, is less intuitive, being phenomenologically derived. Along with the basic DW energy variation, it is fairly easy to implement, although for applied OOP fields much smaller than the depinning field, their results have a negligible difference.

Since it builds on the other two models, adding more detail to the mechanisms, the rough wall model has the promise of describing the physics of the situation to a much greater degree, especially at high IP field values, and has already been successful at fitting some of the more peculiar velocity behaviour. Its main downside, however, is the need to calculate the magnetisation direction within the DW for each IP field value at each iteration. This made fitting slow and seemed to leave the software more vulnerable to getting stuck in local minima. As such, due to the success of the basic DW energy density model to fit the majority of my data, it was this basic model which was used in subsequent analysis.

5.5 Dzyaloshinskii-Moriya interaction measurement

Having extracted values for effective DMI field from samples grown at different deposition temperatures and base pressures, one can now see how the DMI is affected by such. This was combined with the structural information

taken for the samples to further the goal of understanding how the structure of the sample affects the DMI strength.

Figure 5.8 shows H_{DMI} for the sets of films grown at a range of base pressures from $(0.6\text{-}3.3)\times 10^{-7}$ Torr plotted against the normalized difference in σ for the upper and lower Co interfaces. The difference in σ was a measure of the difference in disorder of the upper and lower Co interfaces. Measuring the net DMI field for several sets of samples permitted a correlation to emerge, as the DMI is exquisitely sensitive to the difference in quality of the upper and lower Co interfaces. The difference in σ was normalised by the total σ to highlight any dependence on the interface quality difference, independent of any changes in total σ , since a change in σ was likely to have a greater effect on more ordered systems than more disordered ones.

Figure 5.8 shows that the net DMI in epitaxial Pt/Co/Pt increased from zero to positive values when the quality of the top interface decreased relative to the bottom, and decreased from zero to negative values when the quality of bottom interface decreased relative to the top. A linear fit to the data yielded a Pearson's r correlation coefficient of 0.52. This indicated a moderate correlation[136] between net DMI and relative interface quality, in spite of the scatter. This scatter could arise mainly from fluctuations in the base pressure and deposition temperature when growing and from the uncertainty in σ for individual interfaces. While the scatter meant we did not have perfect control over the properties of a film using this method, there was sufficient correlation that the majority of data points were fairly close to the fitted line. Sensitive interface effects were particularly difficult to control when, as here, there was more than one interface to consider. Given this, the correlation gets a long way towards understanding and separating the relative effects of the two interfaces.

Batch AW240815, with a base pressure of 0.6×10^{-7} Torr, was included here, despite the deviation in its substrate preparation, to illustrate that it still followed the same trend, albeit with considerable scatter. This was to be expected, since its substrate preparation should only have changed the σ values and it was these values that were taken as the independent variable. Thus the dependence of H_{DMI} on $\Delta\sigma$ should have remained unchanged.

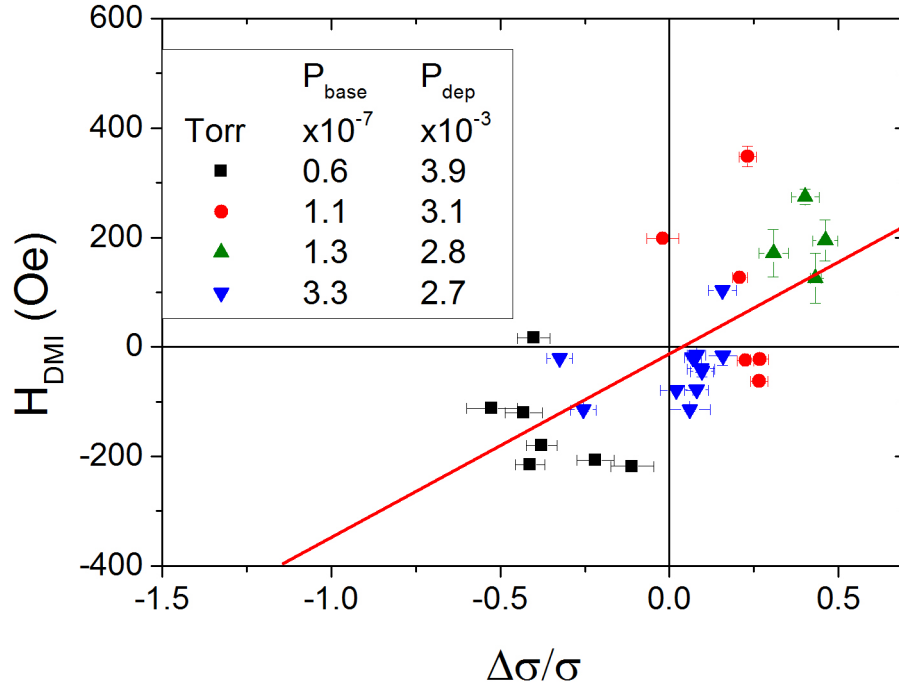


Figure 5.8: Net H_{DMI} as a function of $\Delta\sigma/\sigma$, the difference between the top Co interface σ and the bottom Co interface σ for epitaxial Pt/Co/Pt deposited at temperatures in the range 100-300°C, normalized by the total σ . A positive (negative) $\Delta\sigma/\sigma$ corresponds to the lower (upper) Co interface being a higher quality than the upper (lower). The errors associated with $\Delta\sigma/\sigma$ relate to the suitability of the σ values to the fitted X-ray reflectivity models so act as a lower bound of uncertainty due to the deviations of the fits. The solid line is a linear fit to the data.

The conclusion that may be drawn from Fig. 5.8 is that the net DMI field in epitaxial Pt/Co/Pt can change by up to 400 ± 100 Oe depending on the deposition conditions. For less ordered, polycrystalline Pt/Co/Pt, therefore, it is no surprise that larger DMI fields may be obtained, e.g. Franken et al[14] obtained $H_{\text{DMI}}=370 \pm 10$ Oe in a polycrystalline stack with a thinner Co layer (4 Å) and Hrabec et al.[2] obtained $H_{\text{DMI}}\sim 1000$ Oe for films with a similar Co thickness but polycrystalline and with a different Pt thickness. Naïvely mapping $H_{\text{DMI}}\sim 1000$ Oe onto Fig. 5.8 yielded a difference in $\Delta\sigma/\sigma$ of -2.5, which would have meant that the difference in interface quality was greater than the total interface quality, and suggested that there was another factor at work here, possibly related to the polycrystallinity.

A further study in into DMI change with interface morphology used ion irradiation of polycrystalline Pt/Co/Pt and was carried out by Balk et al.[137]. They found that the DMI field could be changed and its sign reversed depending on the level of irradiation it was subjected to. They also found the coercivity decreased with increasing ion dose and attributed these effects to the removal of the top interfacial Pt and an increase in interface roughness, respectively. By increasing the disorder primarily of the top Co/Pt interface, the DMI field was made positive in sign, as seen in this project. They also, interestingly, showed velocity-field graphs with the peculiar behaviour of pronounced kinks and peaks, which did not appear in the epitaxial Pt/Co/Pt samples of this project.

For samples of type A where growth was initiated at base pressures at the lower end of the range studied here, H_{DMI} increased monotonically as a function of T_{dep} in a roughly linear fashion, as shown in Fig. 5.9. As the base pressure increased, the temperature had less influence on the interface quality and thus the range of H_{DMI} values decreased and became less obviously linear in temperature. Using the prior finding that the lower Co interface contributes a positive H_{DMI} [2], and the conclusion that a higher quality (smaller σ) interface contributes a larger H_{DMI} , the increase of H_{DMI} with T_{dep} may be interpreted as follows. As T_{dep} increased, the quality of both interfaces, but particularly the upper, decreased until annealing dominated and their quality improved. This difference in interface quality

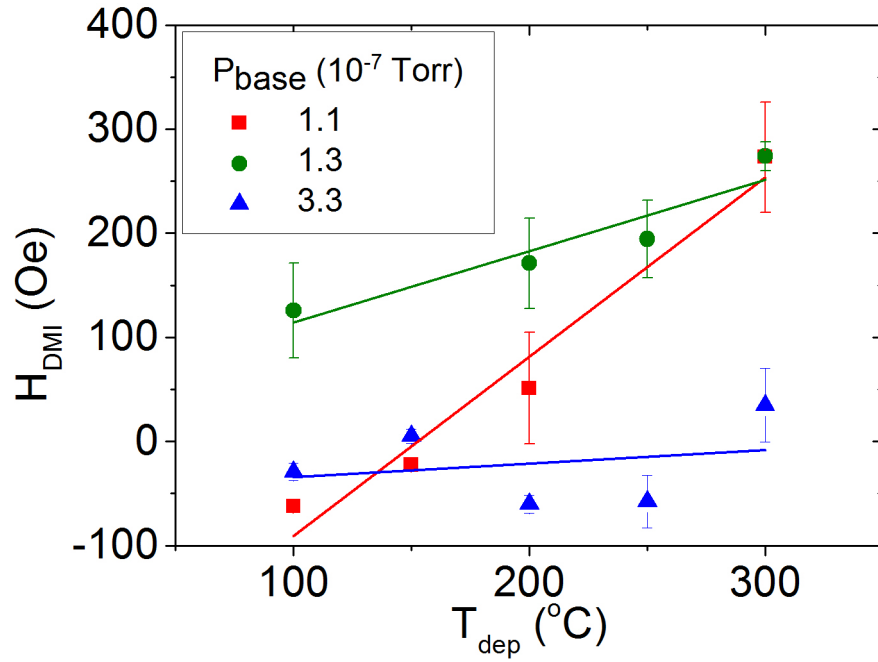


Figure 5.9: Net H_{DMI} as a function of T_{dep} for epitaxial Pt/Co/Pt where growth was initiated at various base pressures. The solid lines are linear fits to the data. The error bars are the larger of either statistical standard error or error in velocity vs H_x fits.

introduced structural inversion asymmetry, necessary for a net DMI field to occur, increasing as the contribution from the top interface was reduced, as seen in Fig. 5.9. As the Co interfaces became of a similar quality, the DMI contributions from the top and bottom cancelled, causing no net DMI. If the bottom interface was of a lower quality than the top, the dominant contribution switched and the effective DMI field became negative. This showed that if the base pressure is at the lower end of the range studied here, substrate temperature may be used to linearly adjust the DMI.

5.6 Conclusions

In this chapter, the experimental challenges and solutions to measuring magnetically-induced magnetic domain wall motion have been presented, with the limitations of the bubble expansion technique being made clear. This technique has been used to show that, for the range of magnetic driving fields used, the DW motion was in the creep regime, and remained in the creep regime even with the application of an IP field. The exponential scaling factor was seen to change, even with small IP fields (~ 300 Oe), due to the change of DW energy density.

Three of the most common models were then investigated by fitting them against the acquired velocity against IP field data. The basic creep law with varying domain wall energy density fitted the data well, for the low IP field strengths, with deviations at higher fields for but a few samples. Upon using the universal creep law with the exponential scaling factor modified in a similar way to previously, no difference was seen between the fits produced and those of the basic model. This could be explained by the applied OOP field being well below the depinning field, in which case the universal creep law model tends towards the basic creep law. A model incorporating rough domain walls was also investigated, though due to the increased complexity, the fits were often considerably worse than the basic model. Since the data used here had none of the peculiarities which the rough wall model was developed to address, the basic model was deemed most appropriate in this case.

The DMI field extracted from fitting the DW velocity against IP field was plotted against structural data, namely the difference in interface disorder between the top and bottom Co interfaces. Though significant spread was seen, a linear correlation could be deduced with a correlation coefficient of 0.52, indicating moderate correlation. This link showed how important the disorder at the interface is for DMI strength, allowing the net DMI to vary considerably and even change sign in these nominally symmetric stacks. Since the interface disorder was linked to the deposition temperature in Chapter 4, the DMI field was also plotted against deposition temperature, showing a rise in positive DMI field strength with deposition temperature. This rise was seen to be more pronounced in sample batches where the base pressure was lower, indicating the effect that impurities have upon the DMI strength.

Chapter 6

Magnetic field-induced domain wall motion in exchange biased systems

This third experimental chapter focuses on Pt/Co/Ir₂₀Mn₈₀ stacks with and without an exchange bias. Antiferromagnetism has received a lot of interest in recent years, from exchange biasing systems[138] to eliminating stray fields in synthetic setups[139], as well as boosting SOT efficiencies in ferromagnet (FM)/antiferromagnet (AFM) bilayers[140]. Thus, if the combined efficiency of enhanced SOT and Néel walls from the Dzyaloshinskii-Moriya interaction (DMI) is to be used, it is necessary to know how an AFM affects the DMI in a magnetic multilayer. This chapter begins to explore this, optimising the growth parameters to produce samples with coercivities low enough to be measured in our experimental setup. Two thicknesses of IrMn were used, samples with the thicker exhibiting an exchange bias, ones with the thinner not providing one. Kerr microscopy showed the samples with an exchange bias to reverse their magnetisation via mass nucleation of small, rough domains, unsuitable for DMI measurement using the bubble expansion technique. The thinner samples showed highly skewed velocity-field graphs which are not well described at high in-plane fields by any model yet encountered.

6.1 Deposition

The basic set of samples were grown as Pt (3 nm, 550°C)/Co (0.7 nm, 100°C)/ Ir₂₀Mn₈₀ (t nm, 100°C)/Pt (5 nm, 100°C). The deposition temperature and pressure were optimised for low coercivity from a temperature range of 100°C to 300°C and a pressure range of 3.9 mTorr to 6.5 mTorr. The Pt cap was increased in thickness from the 1 nm thick capping layer of Pt/Co/Pt as it was found that the magnetic properties of the earlier samples had changed since they were last measured. This could be from the capping layer being insufficient, allowing the Co layer to become oxidised if the coverage was not 100%, or it could be from room-temperature interdiffusion between the Pt and the Co. To rule out the former, the Pt cap was subsequently increased in the IrMn samples. Comparing samples with different cap thicknesses showed no change in magnetic properties. Since the Pt/Co/Pt samples showed no change over the course of the couple of months each was initially measured after growth, instead changing significantly over the course of two to three years, it is unlikely that any change will be seen in the IrMn samples, even if the cause was room-temperature interdiffusion, since they were measured within four months of being grown.

Since the critical temperature for an exchange bias to appear in IrMn, its blocking temperature, is related to its thickness[141], two thicknesses were grown: 2 nm of IrMn needs temperatures far below room temperature to see exchange biasing, and so was taken as the control set; 5 nm shows exchange biasing far above room temperature and so was used to assess the effect of exchange bias on the system. The general rule of thumb is that the blocking temperature in degrees Kelvin is roughly equal to the layer thickness in nm multiplied by 100[141]. The spin structure of the disordered γ -Ir₂₀Mn₈₀ grown in the (001) direction is shown in Fig. 6.1. The spins are orientated 45° away from the crystal diagonals[82], which leads to a break in cubic symmetry, despite there being no net magnetisation when averaged over several unit cells. When grown on Co with a magnetisation perpendicular to the film plane, it is likely, then, that the spins will take the configuration which is most parallel to the film normal at the interface.

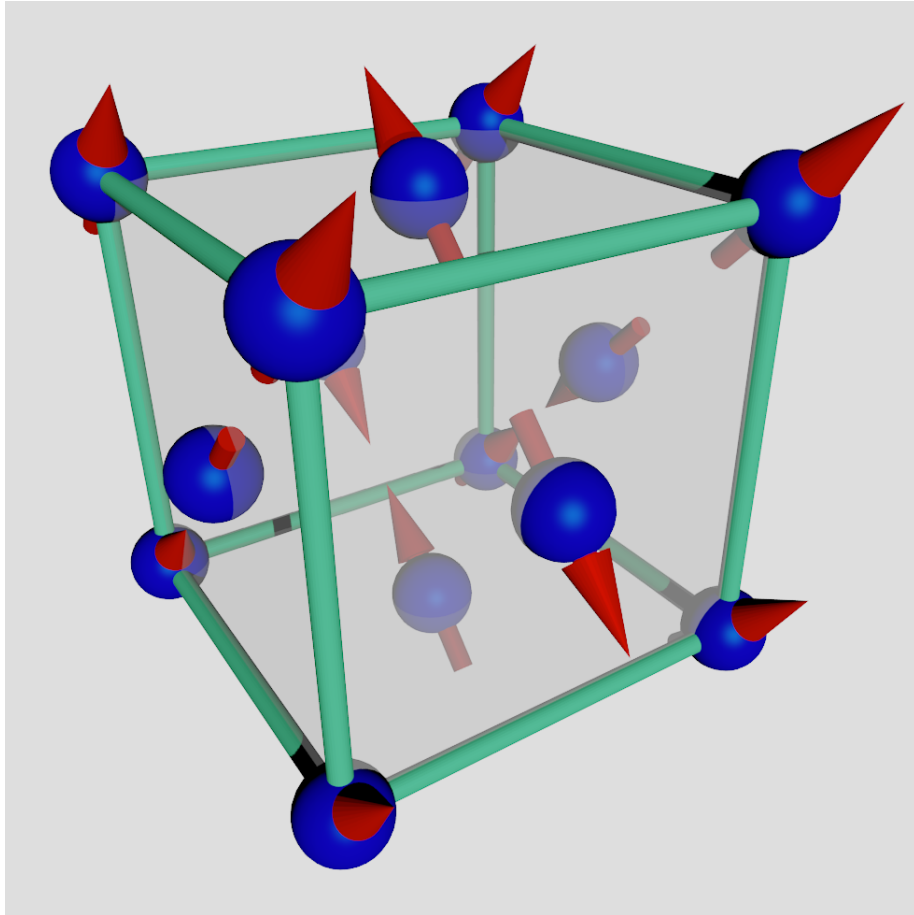


Figure 6.1: Theoretical spin structure of Ir₂₀Mn₈₀ in a disordered state according to Kohn et al.[82]. Each atom (blue spheres) has an 80% chance of being Mn, with a magnetisation as shown (red arrows).

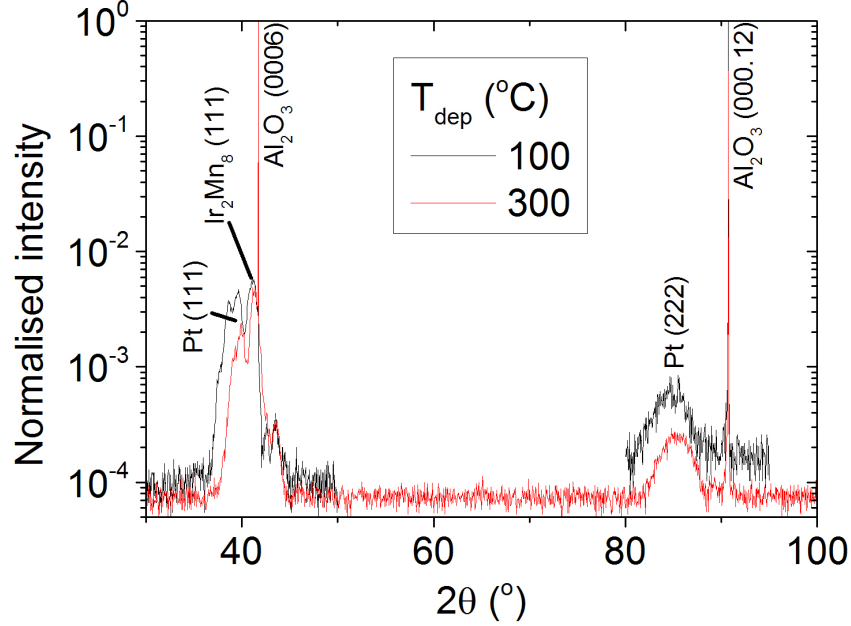


Figure 6.2: X-ray diffraction of Pt/Co/Ir₂₀Mn₈₀/Ta with the Co/Ir₂₀Mn₈₀ grown at a high deposition temperature (T_{dep}).

6.2 Characterisation

Characterisation of these samples was carried out akin to the Pt/Co/Pt samples, mainly using X-ray reflectometry and laser MOKE.

6.2.1 Structural

X-ray diffraction (XRD) and X-ray reflectivity (XRR) data was taken for samples of the basic IrMn stack, though with the deposition temperature of the Co and IrMn varied between 100°C and 300°C, similar to the Pt/Co/Pt stacks of Chapter 4.

As seen in Fig. 6.2, XRD scans showed peaks only where expected for Pt and IrMn (the Co being of too low an intensity to be clearly seen). Thus, these samples were epitaxial up to the sensitivity of these scans. The inclusion of IrMn complicated the scan compared to the purely Pt/Co/Pt stacks, introducing a (111) peak at 41.6°. The Pt (111) peak seen in the

sample grown at 300°C was of a lower intensity than for the 100°C sample, suggesting a lower degree of ordering. Whether this disorder was from the Pt or from the surface of the substrate, leading to lower Kato fringes off the Al₂O₃ (006) peak, was uncertain.

Similar X-ray analysis was undertaken for structures with the Co and IrMn layers grown at 100°C, but at varying thicknesses. The extracted σ values are shown in Fig. 6.3 against the extracted Co thicknesses. Due to the necessity for many variables when fitting the X-ray data, the uncertainty on individual values could, in some cases, approach a similar magnitude to the value. This was seen in a particularly striking manner in the Co thicknesses, in which the extracted value could differ significantly from the nominal, though the nominal is always within uncertainty. Since the thickness of a layer was fairly controllable during growth, it is likely that the values were in actuality fairly close to the nominal and, for clarity, samples shall be referred to by their nominal thicknesses.

Figure 6.3 (A) and (B) show representative fits to the data for thin and thick IrMn layers, respectively. This was carried out in Bede REFS[120] using the logarithm of the mean absolute error as the goodness of fit parameter. One saw relatively good fits, encompassing most of the major features of the scan, only with some deviation in intensity at some of the peaks and troughs of the fringes. Not all fits were so successful, particularly for the sample with 5 nm IrMn, 1.1 nm Co which deviated considerably in some of the trough intensities, hence the large error bars in (C). Figure 6.3 (C) shows that, for the samples with 2 nm of IrMn, the average interface disorder stayed fairly constant, within uncertainty. The 5 nm IrMn samples, however, tended to decrease in average σ as the Co layer became thicker. Due to the sensitivity of the DMI to interface roughness of Pt/Co/Pt seen in Chapter 5, it was thought that a similar effect would be seen in these Pt/Co/IrMn samples. However, there were too few samples of Pt/Co/IrMn to extract statistically significant values from such uncertain quantities as individual interface disorder values.

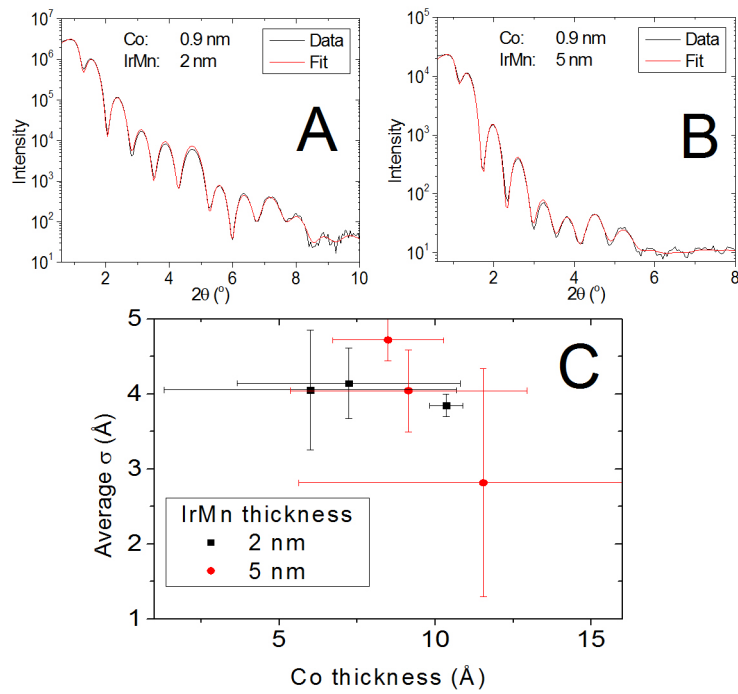


Figure 6.3: Fits and extracted interface disorder of X-ray reflection data of Pt/Co/Ir₂₀Mn₈₀/Pt with the Co and IrMn grown at different thicknesses. (A) and (B) show the fits to the data obtain via Bede REFS[120]. (C) is an average over σ from all relevant interfaces.

6.2.2 Magnetic

Laser MOKE was the main technique used for characterising the magnetic behaviour of the samples. One key aspect of the magnetic behaviour I was looking at was the coercivity. This was because the magnets employed in the confines of the Kerr microscope to carry out the bubble domain expansion method for measuring DMI had a limited strength and so the samples' coercivities needed to be below around 30 mT. To achieve this, sets of samples were grown initially, varying different growth parameters, to optimise the low coercivity.

Similar to Pt/Co/Pt, the deposition temperature can be used as a controlling parameter for the magnetic properties of samples. This is shown in Fig. 6.4 (A) by the change of the MOKE loops with varying deposition temperature- the coercivity and exchange bias changed, but the shape of the loop remained constant with a fairly rapid change of magnetisation direction with applied field, showing that switching by domain wall propagation was dominant.

Figure 6.4 (B) presents the coercive field and exchange bias from the samples shown in (A). There was a fair amount of spread due to the natural variability of sample deposition in the growth environment used, but a clear trend was seen in the coercivity. The coercivity increased with deposition temperature with a Pearson's r correlation value of 0.73, showing strong linear correlation[136]. Since the fast switching in the MOKE loops was indicative of magnetisation reversal by domain wall propagation, the increase of coercivity indicated a general increase in interface disorder as the number of pinning sites increased. This was in line with the change of interface disorder seen in Pt/Co/Pt films in Chapter 4.

The correlation between the exchange bias and deposition temperature had a much greater spread compared to the coercivity, reflected in the lower Pearson's r correlation value of -0.60. This r value also showed that the correlation was of an inverse variety, indicating that the structural changes were more akin to those from working pressure variation than Co thickness variation seen later in Fig. 6.5 and Fig. 6.6, respectively. Numerical

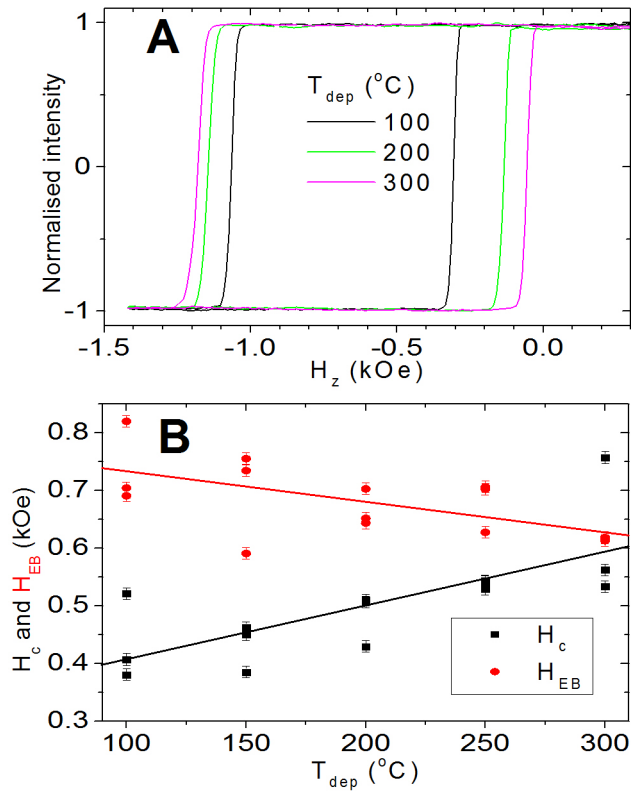


Figure 6.4: (A) Representative MOKE graphs for samples of Pt/Co(0.7 nm)/IrMn(5 nm)/Pt with varying deposition temperatures of Co/IrMn, all grown at a working Ar pressure of 3.9 mTorr. (B) Extracted values of coercivity and exchange bias against the substrate temperature at which they were deposited. The lines show linear fits.

simulations in literature[142] have shown that exchange bias is reduced with increased interfacial disorder, indicating that the Co/IrMn interface becomes more disordered with increased deposition temperature. This, too, agreed with the trend in Pt/Co/Pt. Since the lowest coercivity was seen in the samples grown at 100°C, subsequent samples were grown at this substrate temperature.

The working pressure at which the Co/IrMn layers were deposited also played a large role in determining the magnetic behaviour of the sample. This is seen in Fig. 6.5 for three pressures in the range of 3.9 mTorr to 6.5 mTorr, again for samples with 2 nm and 5 nm of IrMn. In the samples with 2 nm of IrMn, Fig. 6.5 (A), and so no noticeable exchange bias, there was a clear change in coercive field with deposition working pressure. The coercivity slightly increased with pressure between 3.9 mTorr and 5.2 mTorr by 9%, before decreasing by 75% as the pressure further increased to 6.5 mTorr. The large decrease for the higher pressure was likely due to a decrease in kinetic energy of the sputtered atoms, causing less disruption to the existing structure. This trend, however, was in opposition to the findings of He et al.[143] in polycrystalline superlattices of [Co(3 nm)/Pt(15 nm)]₁₇, sputtered at room temperature, where the coercivity was seen to monotonically increase with deposition pressure. This contradiction was not too surprising, considering the sensitivity of the coercivity to structure, as the behaviour was likely to differ considerably between the hot-grown epitaxial samples of this project and polycrystalline structures. Not only that, but the thinness of the Co layer led to any intermixing at the interface having a much larger effect on the overall structure. Finally, He et al. neglected to say what gun power or throw distance they used, making meaningful comparison of results unreliable. To test the reliability of these scans and their tendency towards training, a scan was run on the 5.2 mTorr sample consisting of several sweeps. The result is seen in Fig. 6.5 and showed no significant change between sweeps, indicating negligible training. Since the sample grown at the higher pressure of 6.5 mTorr showed a coercivity low enough to be studied in the bubble domain expansion method, subsequent samples were grown near to 6.5 mTorr.

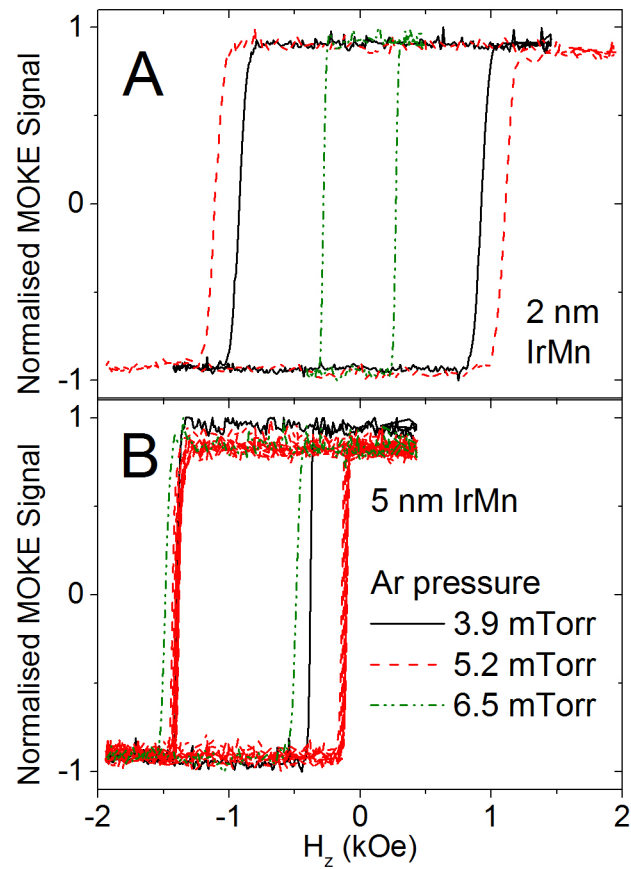


Figure 6.5: MOKE graphs for samples of Pt/Co(0.7 nm)/IrMn/Pt grown at three working Ar pressures. (A) shows samples with 2 nm of IrMn. (B) shows samples with 5 nm of IrMn. The 5.2 mTorr loop in (B) is composed of multiple loops to show repeatability.

A similar pattern is seen in the samples with 5 nm of IrMn, Fig. 6.5 (B), except that the samples grown at 3.9 mTorr and at 6.5 mTorr had equivalent coercivities. The exchange biases seen in these samples followed the inverse of coercivity, with the 5.2 mTorr sample having the lowest. This trend indicated that the interfaces were likely to be less disordered for the higher pressure sample, particularly the Co/IrMn interface responsible for effecting the exchange bias. To keep the comparison between the 2 nm and 5 nm IrMn samples as controlled as possible, both were grown at the same working pressure. For this to be the case, due to the high exchange bias in the high pressure 5 nm IrMn sample, even with a slightly reduced exchange bias, one side of the sweep would always be out of range of the intrinsic Kerr microscope WHOOP coil, and so another means of switching would need to be employed.

Figure 6.6 shows the variation of MOKE loops for Pt/Co/IrMn/Pt with Co thickness. In samples both with 2 nm and 5 nm of IrMn, it was clear that the largest coercivity, H_c , was seen in samples with 0.9 nm of Co, with a slight decrease of about 11% and 15%, respectively, for 0.7 nm and a larger decrease of 58% and 49%, respectively, for 1.1 nm. This peak was seen elsewhere in literature, such as in work by Sort et al.[79], who ascribed it to a change in perpendicular anisotropy. This link between coercivity and anisotropy was strengthened by results seen in this thesis in Fig. 6.7: a peak at 0.9 nm of Co, with a lower value for 1.1 nm than 0.7 nm. In Sort et al.'s paper, the peak in anisotropy was at a slightly lower Co thickness of about 0.7 nm, though with a higher number of data points. The peak was seen in other material systems as well, for instance in Pt/Co/FeMn by Ji et al.[144] where it manifested around 0.9 nm of Co; or in Co on Cu grown by MBE[145] where the coercivity was seen to increase linearly with Co thickness up to 6 monolayers (ML), before falling as the inverse of thickness. The explanation they gave was based upon the increase of the Curie temperature with Co thickness, as seen by Diaz-Ortiz et al.[146]: up to 6 ML, the Co had a reduced Curie temperature and was behaving with reduced dimensionality, leading to a higher domain wall mobility and a lower coercivity. The rise was seen in other Pt/Co systems, for instance in work

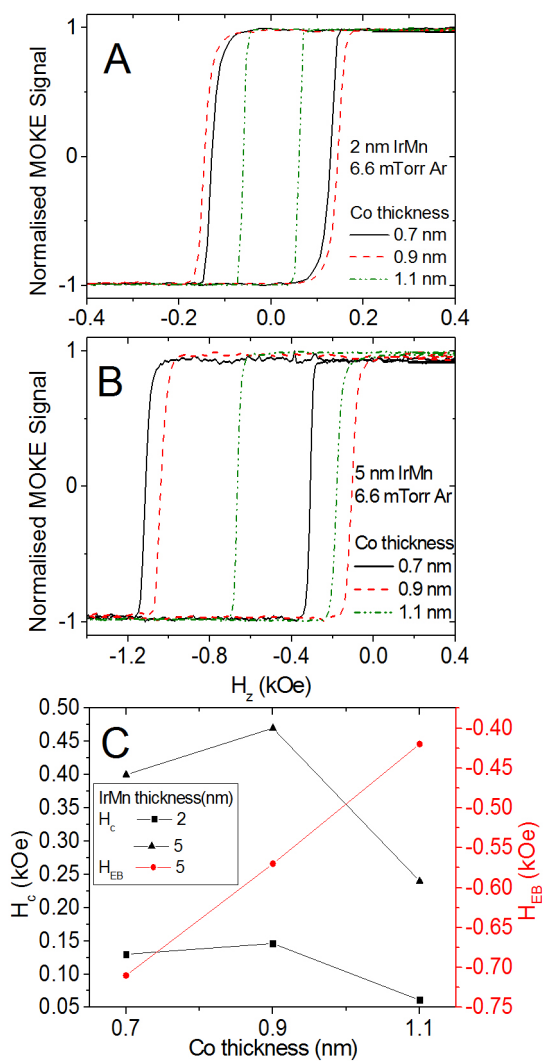


Figure 6.6: MOKE graphs for samples of Pt/Co/IrMn/Pt with three thicknesses of Co, all grown at a working Ar pressure of 6.6 mTorr. (A) shows samples with 2 nm of IrMn. (B) shows samples with 5 nm of IrMn. (C) shows extracted coercivity and exchange bias data.

by Nie et al.[99]. The drop off in coercivity at thicker Co thicknesses was only seen in well-ordered layers, as in the MBE-grown Pd/Co samples of Kingetsu[147], with an increase or levelling off seen in the rougher samples of Weller et al.[148] and Jiang et al.[149].

The change in exchange bias is also seen clearly in Fig. 6.6. With a blocking temperature below room temperature, and so no exchange bias, MOKE loops for the samples with 2 nm of IrMn were seen to be symmetrical about zero applied field. In the samples with thicker IrMn, exchange bias was seen, and changed in a more standard fashion with the highest exchange bias of 71 mT in the sample with 0.7 nm of Co. Exchange biases of 57 mT and 43 mT were seen in the 0.9 nm and 1.1 nm Co samples, respectively, which fitted with the contribution of the interfacial exchange bias diminishing with Co thickness. These results were similar to the findings by Chen et al.[150], looking at IrMn on and under Co coupled to a [Pt/Co]₃ multilayer, except they found peaks in exchange bias and coercivity occurring at lower Co thicknesses. They attributed the initial increase of exchange bias to an increased interfacial anisotropy due to the formation of a continuous film.

To see how the effective anisotropy changes, one can refer to Fig. 6.7, in which one sees the OOP anisotropy changing akin to the coercivity, though differently to the exchange bias, being non-monotonic in its evolution with Co thickness. The trend being similar to the coercivity suggest that the change in coercivity and anisotropy have the same underlying controlling parameters. One would expect the anisotropy to decrease with thicker Co layers as the interface plays less of a role, as seen between samples with 0.9 nm and 1.1 nm of Co. Were the study to have continued to thicker Co samples, one should have seen the effective OOP anisotropy field become negative as the shape anisotropy overcame the interface anisotropy and the sample's easy axis aligned with the plane of the film. This should have happened at a thickness of just over 1 nm[151], and the fact that even at 1.1 nm of Co, a strong PMA was still seen was most likely due to the actual Co thickness being slightly less than the nominal one presented here.

A feature of Fig. 6.7 which is worthy of comment is the large magnitude of the anisotropy values (1-9 T), which were several times larger than for

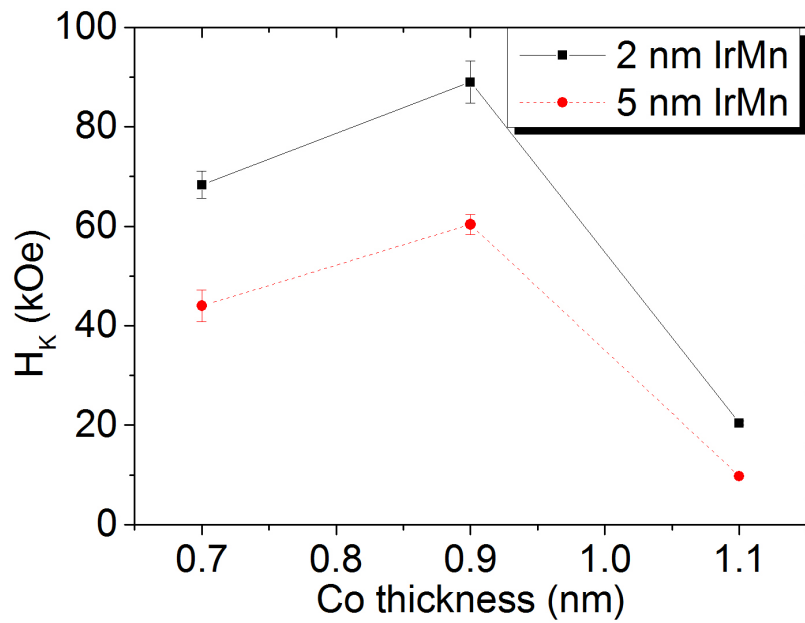


Figure 6.7: The change in effective out-of-plane anisotropy field, H_K and ordinary Hall effect contribution with Co thickness for samples of Pt/Co/IrMn/Pt with three thicknesses of Co, all grown at a working Ar pressure of 6.6 mTorr. Black squares are samples with 2 nm of IrMn. Red circles are samples with 5 nm of IrMn. Co thicknesses are displayed as their nominal thicknesses.

Pt/Co/Pt (1.5 T). This was unexpected as IrMn, when exhibiting exchange bias, has been seen to counteract PMA[152] so should result in a lower effective anisotropy field. Values of effective anisotropy reported in literature corresponded to much lower anisotropy fields[152, 153]. These large values seen in this thesis could indicate some miscalibration in the method for extracting anisotropy values (if, for instance, the applied magnetic field was smaller than recorded) or the method not being suitable for Co/IrMn samples. Despite this, the extraordinary Hall effect voltages measured were as expected for the varying applied fields, so it is likely that the trend was reliable, even if there was doubt about the absolute values. The argument for the negative effective OOP anisotropy field at the interface given by Dijken et al.[152] on a basic level is that the antiferromagnetism tilts the Co spins out of normal orientation. This could explain why the samples with 2 nm of IrMn had higher anisotropy field values than those with 5 nm IrMn, since the antiferromagnetism was not manifested.

6.3 Domain wall structures

In order to use domain wall motion methods for extraction of various samples properties, such as the Dzyaloshinskii-Moriya interaction (DMI) or spin torques, those samples must exhibit clear domain walls, ideally in the form of bubbles from isolated nucleation points as set out in Section 5.1.1.

Figure 6.8 shows imaged domain structures of Pt/Co/IrMn/Pt samples with Co thicknesses of 0.7 nm (A, D), 0.9 nm (B, E) and 1.1 nm (C, F) for two thicknesses of IrMn: 2 nm (A,B,C) and 5 nm (D,E,F). In the samples with 2 nm of IrMn, where the IrMn was too thin for exchange bias to be manifested, the domain structure was similar to Pt/Co/Pt for 0.7 nm and 0.9 nm of Co, showing isolated bubble domains. The perpendicular magnetic anisotropy (PMA) was strong enough for the samples to be OOP, with Fig. 6.7 showing that the samples with no exchange bias had larger PMA than those with exchange bias.

The sample with 1.1 nm of Co showed an interesting Voronoi-like network of domains. This was due to a sufficiently high DMI to stabilize a Néel

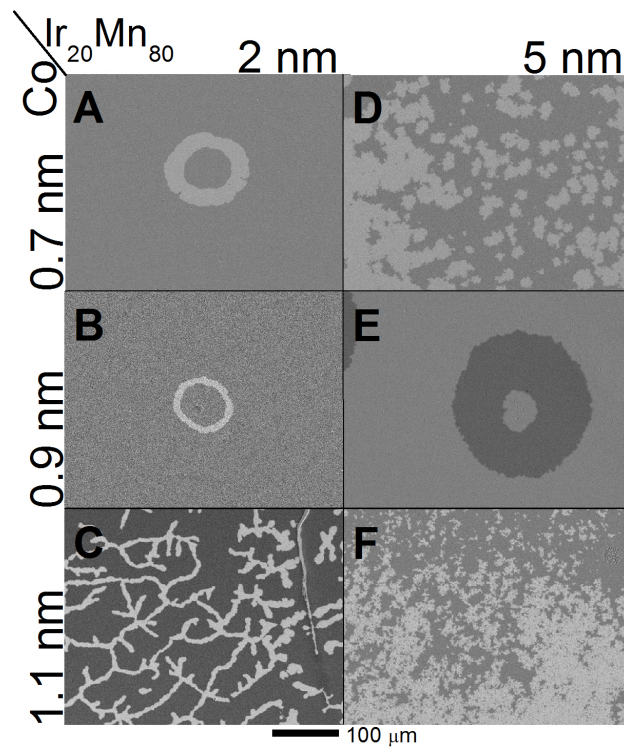


Figure 6.8: Kerr images of samples of Pt(3 nm)/Co(x nm)/IrMn(y nm)/Pt(5 nm) with varying thicknesses of Co and IrMn, all grown at 100°C at a working Ar pressure of 6.6 mTorr.

component in the domain walls which, being homochiral, formed a 360° domain wall rather than annihilating, as discussed in 3.7.3. The appearance of a Voronoi-like domain wall network in only this sample is unlikely to be due to an increased net DMI strength, since the thicker Co layer led to less of an interfacial contribution; instead the decreased interfacial PMA allowed nucleation at lower applied fields than for samples with thinner Co. It is most probable that the lack of a Voronoi-like network in the thinner Co samples was because their nucleation fields were higher than those needed to annihilate the 360° domain walls, meaning that such a network was never seen. Thus, it is the interplay between the anisotropy and the DMI in the sample that leads to such a phenomenon.

In the samples with 5 nm of IrMn, at least in the 0.7 nm and 1.1 nm Co samples, the well-formed bubble domains of the thinner IrMn were lost to be replaced with many small, rough domains. The IrMn layer, when in its paramagnetic (2 nm) state, easily follows the Co magnetisation; however, it becomes fixed when in its antiferromagnetic (5 nm) state, causing local inhomogeneities in the Co as it couples to the uncompensated spins. It is this coupling which is likely to have been the cause of the high nucleation and pinning. A similar situation to the 0.7 nm Co sample was seen by Romanens et al.[154] in the form of a higher nucleation density, but to a much lesser degree since fairly smooth bubble domains were still seen and only in one magnetic field sweep direction. They attributed this to local inhomogeneities in the exchange bias field. Since the epitaxial samples used in this thesis should have had a much decreased level of inhomogeneity, though, it is likely that there were more factors at play to make the nucleation so pronounced.

The sample with 5 nm of IrMn and 0.9 nm of Co differed from the other 5 nm IrMn samples in that there were several places where nucleation occurred at a much lower field, making it appear like the 2 nm IrMn sample. However, upon propagation of these domains, distinct differences arose, as seen in Fig. 6.9. The domain wall velocity dropped rapidly with increasing distance from the nucleation point despite having the same driving impulse. This showed that the environment changed significantly close to the nucleation point, either through a variation of the pinning site density or strength,

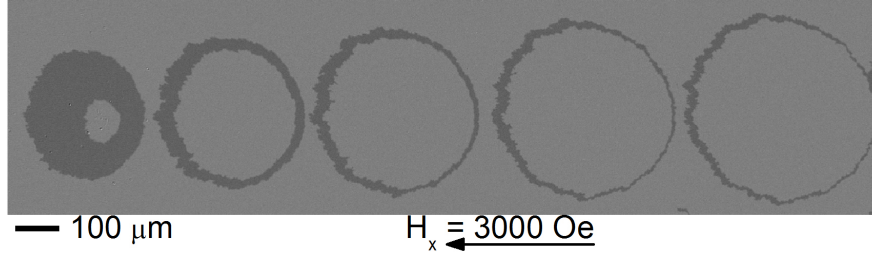


Figure 6.9: Kerr images of the propagation of a sample of Pt(3 nm)/Co(0.9 nm)/IrMn(5 nm)/Pt(5 nm) grown at a working Ar pressure of 6.6 mTorr. Images are time-evolved from left to right, with each image being taken after an OOP field pulse of the same strength and duration.

affecting the characteristic velocity or exponent factor in the creep law, respectively. It is unlikely that the domain wall energy was being modified as the same behaviour was seen, in symmetric bubble domains, when there was no applied in-plane (IP) field.

6.4 DMI

Since the domain walls of the sample with 1.1 nm Co and 2 nm IrMn formed 360° domain walls, the annihilation method could be used on them, see section 3.7.3; the results of which are shown in Fig. 6.10. The trend seen was that which was expected, with a constant coercivity for high values of maximum applied field, H_{\max} , that dropped suddenly as H_{\max} decreased below a certain value. Below this value, the applied field was enough to reverse the magnetisation in the majority of the film, but was unable to annihilate all of the 360° domain walls, leaving a proportion of them to act as nucleation centres when switching the magnetisation in the opposite direction and thus lowering the coercivity. The value was 15 ± 5 mT, which had to be converted into DMI strength through modelling the DW in simulations done by Benitez et al. [96], and led to a value 0.15 ± 0.05 mJ/m². Since, however, the model used by Benitez et al.[96] assumes a defect-free structure at a temperature of absolute zero, this served only as a minimum value. Comparing this value to literature, it was found to be an order of magnitude smaller than other

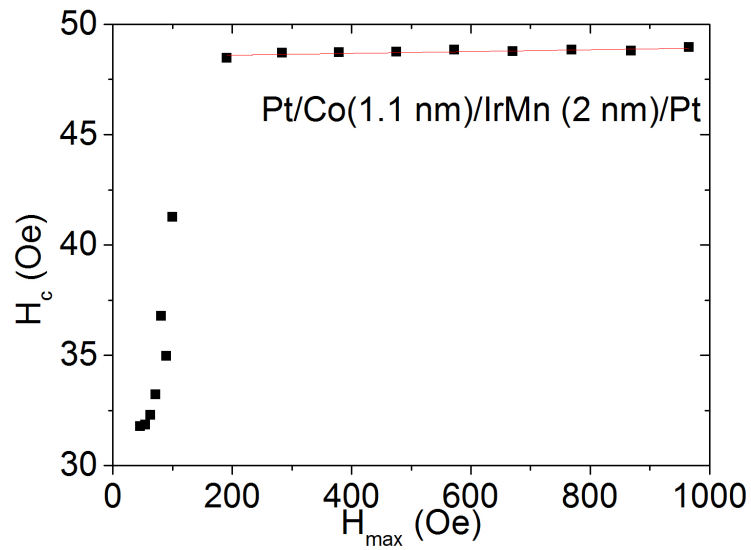


Figure 6.10: The variation of coercive field, H_c , with the maximum applied OOP field, H_{\max} , from laser MOKE scans for samples of Pt(3 nm)/Co(1.1 nm)/IrMn(2 nm)/Pt(5 nm) grown at a working Ar pressure of 6.6 mTorr. The red line corresponds to a linear fit of the data.

DMI values taken for Co in various systems by various other methods[98], though none for Pt/Co/IrMn. It was about a factor of two smaller than for the Pt/Co/AlO_x used in the annihilation method by Benitez et al., showing consistency within the method. This small value, compared to other methods, fitted with the notion that this value was a lower bound and, as highlighted by Benitez et al., could have been considerably higher.

Due to the lack of bubble domains within suitable environments in most of the samples, only samples with 2 nm of IrMn and 0.7 nm and 0.9 nm of Co could be analysed using the bubble expansion technique. The recorded domain wall velocities are shown in Fig. 6.11, with the fits to them using the basic domain wall energy varying creep model from Section 2.2.1 at various OOP field strengths and positions. The model fitted well to most of the data, however there was a distinct difference between these samples and those of Pt/Co/Pt, which was that a minimum velocity was not seen: as the applied IP field increased in strength, one of the domain walls increased in velocity as expected, whereas the other tended to a point where its movements were imperceptible. This could have been due to the effective DMI field being larger than the range of the applied IP magnetic field. If the absolute magnitudes of the anisotropy values taken earlier were, indeed, correct, the effective DMI field could have been larger than the 2800 Oe maximum IP field, even with a DMI constant, D , consistent in magnitude with other values in literature.

Despite the basic model fitting well to the data, there were inconsistencies, as seen particularly in the 0.9 nm Co sample at 90 mT and -90 mT OOP field, in the form of bumps around $H_x = 750$ Oe (emphasised by blue arrows in Fig. 6.11 (C) and (D)). This is a feature not permitted by the basic DW energy variation model; however, it was seen in a model proposed by Pellegren et al.[73]. Figure 6.11 also shows that the OOP field strength did not affect the form of the velocity curve, merely changing the magnitude of the velocities, and that the samples were homogenous on a large scale as moving to a different position produced the same results. Comparing data from the two samples showed that, again the form was the same, but the sample with the thinner Co layer showed slightly faster DW motion for a

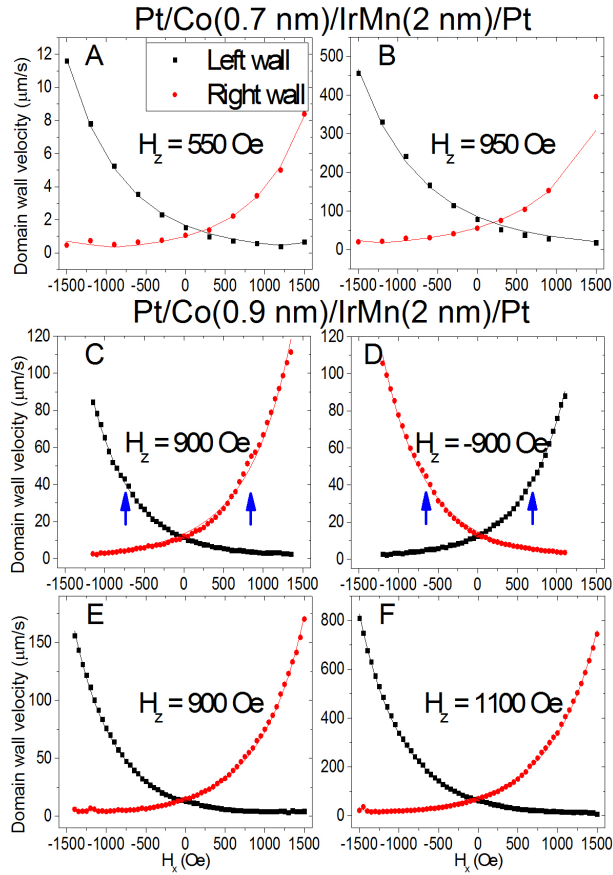


Figure 6.11: The variation of domain wall velocity with applied in-plane field, H_x , propagated with a given out-of-plane field, H_z , from Kerr microscope images for samples of Pt(3 nm)/Co(t nm)/IrMn(2 nm)/Pt(5 nm) grown at a working Ar pressure of 6.6 mTorr. The lines correspond to fits of the data using the basic domain wall energy varying creep model. (C) and (D) were taken at a different part of the sample to (E) and (F). The blue arrows in (C) and (D) emphasise bumps, deviating from the model.

given driving field.

In order to ascertain the effect of crystallographic direction on the domain wall expansion, the sample was rotated about its normal, in both directions by 45° . The result is seen in Fig. 6.12 and shows negligible change to the form of the curves, indicating little or no effect of crystallographic direction. One aspect highlighted by Fig. 6.12 (B) is the deviation of the model from the data at high IP fields ($|H_x| > 1500$ Oe). One possible explanation is that of domain tilting suppressing DW velocity, though if the anisotropy fields were as high as measured, this is likely to have been negligible at such relatively low fields. It is possible that the DMI field was larger than the applied field and as the effective IP field neared zero, roughness in the sample dominated and severely slowed down the domain wall. This would not, however, explain the deviation from the model in walls with the DMI field in the same direction as the applied IP field, as the increase in their velocity became roughly linear with applied IP field.

Figure 6.13 shows the extracted values for DMI using the basic DW energy varying creep model. Discounting outliers, which have been seen to be from bad fits, there was spread of about a factor of two, showing the difficulty in reliably fitting data with no clear minimum. There was no clear trend in these samples and no difference in average H_{DMI} value above uncertainty between the 0.9 nm Co and 0.7 nm Co samples. This was not unexpected as since the anisotropy values for these samples, which should be affected by the same factors as the DMI as discussed in Section 6.3, were fairly similar, any change in DMI would be small and could well have been hidden in the spread. One key feature of Fig. 6.13 is the large DMI constant, D , which attained values between -0.6 mJ/m² and -1 mJ/m². This is comparable, but of a different sign, to the D value found for Pt/Co/Ir by Hrabec et al.[2] (1.2 mJ/m²) and a factor of two or more smaller, and a different sign, to Pt/Co/Ir multilayers measured by Moreau-Luchaire et al.[155] (2 mJ/m²). The magnitude of the D value is promising, as it is close to that needed to stabilise skyrmions[155], and so be used in skyrmion-based applications. However, the contradiction in sign was not expected. Whilst the magnitude of the DMI contribution from each Co interface can vary, its

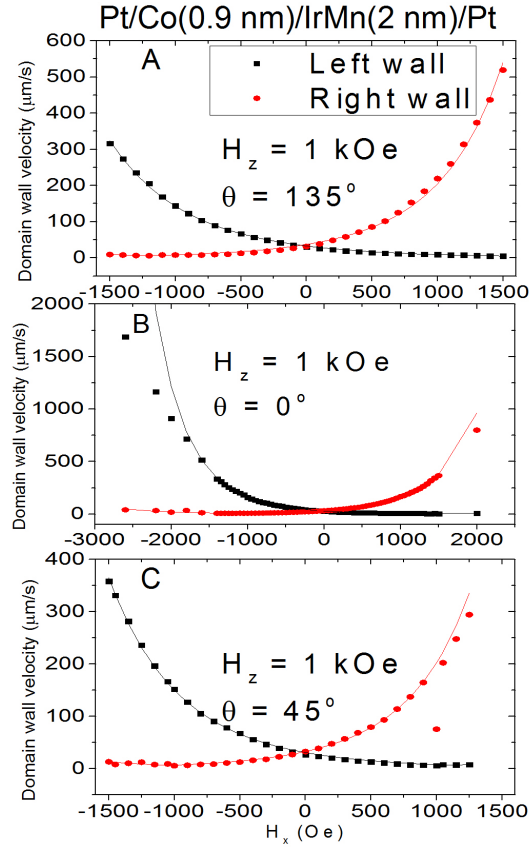


Figure 6.12: The variation of domain wall velocity with applied in-plane field, H_x , propagated with a given out-of-plane field, H_z , from Kerr microscope images for a sample of Pt(3 nm)/Co(0.9 nm)/IrMn(2 nm)/Pt(5 nm) grown at a working Ar pressure of 6.6 mTorr. The lines correspond to fits of the data using the basic domain wall energy varying creep model. θ corresponds to the angle of the sample with respect to the IP field.

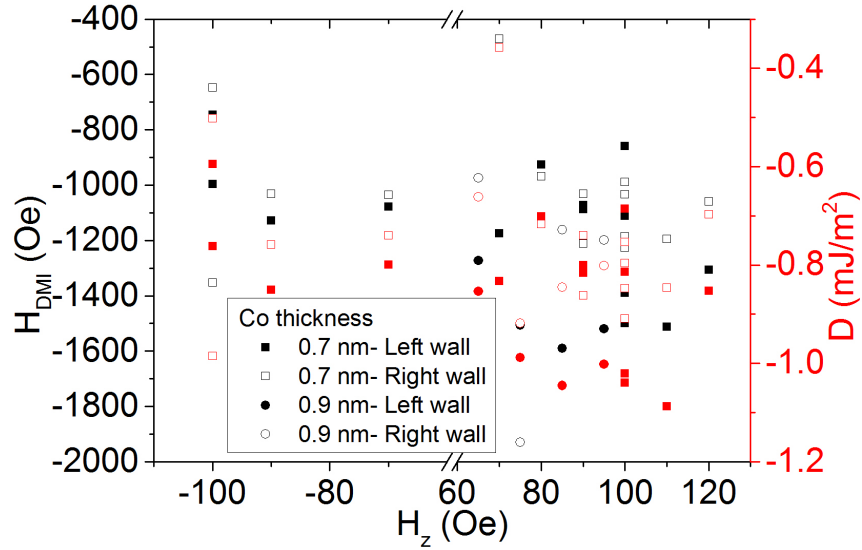


Figure 6.13: The variation of fitted effective DMI field, H_{DMI} , and DMI constant, D , with applied out-of-plane field, H_z , for samples of Pt(3 nm)/Co(t nm)/IrMn(2 nm)/Pt(5 nm) grown at a working Ar pressure of 6.6 mTorr. The data was taken from both left- and right-moving domain walls and fitted using the basic domain wall energy varying creep model.

sign is generally well-characterised and is not known to change. There is a lack of literature dealing with the sign of DMI at a Co/IrMn interface; however, since IrMn has a much lower spin-orbit coupling than Pt[156], its DMI contribution should be insufficient to reverse the sign of the net DMI, especially when considering the large magnitude. A recent arXiv paper by Ma et al.[157] looked at the DMI at an IrMn/CoFeB interface and found a contribution of up to 0.13 mJ/m^2 , confirming the low strength and opposite sign. This all showed that there is more to understand about the nature of DMI in these structures and could form a promising avenue of research.

6.5 Conclusions

It has been shown that sputter deposited films of Pt/Co/Ir₂Mn₈/Pt, grown at elevated substrate temperatures, were epitaxial in structure across a range of substrate temperatures, similar to Pt/Co/Pt films seen in Chapter 4. At room temperature, samples with 5 nm of IrMn showed perpendicular exchange bias greater than their coercivity for several thicknesses of Co and when grown at several different working pressures. As the deposition temperature was raised from 100°C to 300°C the exchange bias and the coercivity became of a similar magnitude.

The anisotropy was seen to be very high for samples with Co thinner than 1.1 nm, though the reliability of the absolute values was in question. The unusual relative trend of anisotropy values showed that disorder at the interface must change with Co thickness.

The mechanics of magnetisation switching were seen to vary significantly for different layer thicknesses. For 2 nm of IrMn with Co thinner than 1.1 nm, bubble domain nucleation and expansion was seen. The basic domain wall energy variation creep law model described the velocity vs IP field data taken at low applied fields, but deviated significantly above about 1500 Oe in a fashion not described by any model yet proposed. The extracted DMI constant values found ranged between -0.6 and -1.0 mJ/m^2 . There was, however, little difference between the values of effective DMI field when values for each sample were averaged over the different driving fields. In

1.1 nm of Co, a Voronoi-like network of 360° domain walls were observed, indicating an effective DMI field high enough to stabilise a Néel component in the domain walls, with an extracted lower bound for the DMI constant in line with literature.

In 5 nm IrMn samples, with exchange bias, there was seen to be a switching by many rough domains, making effective DMI field extraction impractical using the standard bubble domain expansion technique. Brillouin light scattering would be a viable method for these samples, although that technique was beyond the scope of this project. In the 0.9 nm Co sample, points of low anisotropy were seen, leading to the nucleation of bubble domains which decreased greatly in velocity as they expanded away from the point of nucleation, though this behaviour was not repeatable in a later sample growth.

Chapter 7

Conclusions

This thesis began with an overview of some important topics in condensed matter physics, their history and how this project fits into the general scientific narrative. Key theory was provided, necessary for the understanding of results and measurement techniques and those techniques were described. The growth and characterisation of Pt/Co/Pt samples was then delved into, showing how various structural and magnetic properties of the films changed with deposition temperature. It was seen that the samples were epitaxial, with the degree of their overall interfacial disorder depending on the deposition temperature of the top Co/Pt bilayer. By changing the deposition order and which layers varied in deposition temperature, both Co interfaces were found to contribute to the anisotropy of the system. The Dzyaloshinskii-Moriya interaction (DMI) was measured for these samples and the results correlated with the finding of structure. The magnitude and sign of the net DMI was found to depend on the relative degrees of disorder at the Co interfaces. These degrees of disorder were seen to correlate with the deposition temperature such that as the deposition temperature increased, the DMI became more positive. Investigation into stacks of Pt/Co/Ir₂₀Mn₈₀ concluded the experimental part of this thesis, seeing how an antiferromagnetic layer affected the magnetisation dynamics, including DMI. Using a basic model for DW motion, DMI values far higher than in Pt/Co/Pt were found, although none of the models which were popular in literature could

fully describe the domain wall behaviour. Finally, a summary of key results is currently being provided here.

In this thesis, Chapter 4, it was demonstrated that thin films of Pt/Co/Pt can be grown epitaxially on Al_2O_3 (0001). By heated deposition of the Pt seed layer, a smooth interface was formed, onto which the Co/Pt bilayer could be deposited at temperatures in the range of 100°C to 300°C . Due to the nature of the sputtering system, there was a variation in base pressures between depositions, and it was seen that for lower base pressure growths, a higher working pressure was needed to stabilise the plasma. Over the range of deposition temperatures and base pressures, the samples were seen to be epitaxial to such an extent that no X-ray diffraction peaks were seen above noise apart from those expected from a structure with Pt (111). Using the fitting of low-angle X-ray reflection data to a model, the disorder at the interfaces was taken and an average of disorder for the trilayer was found to form a peak with deposition temperature around 250°C . Roughness data taken from X-ray rocking curves about the first Kiessig fringe showed a decrease in interface roughness with deposition temperature, indicating that the peak in total disorder was due to competition between increasing intermixing and decreasing roughness with temperature. The magnetic behaviour of the samples was studied, mostly using the magneto-optical Kerr effect (MOKE), and the coercive field was seen to increase steadily with deposition temperature within the region of interest. Outside of the region of interest, the trends were less clear and, due to fewer samples being studied, had less statistical significance. Laser MOKE intensities and vibrating sample magnetometry (VSM) data showed the saturation magnetisation to remain constant within and between batches, respectively. When studying the effective anisotropy, several types of batches were used so as to give more information about the contributions of the various interfaces. The anisotropy stayed constant within error for the standard sample set, as it did for samples where only the deposition temperature of the top Pt layer was varied in reverse temperature order (colder to hotter). However, if both the Co and top Pt layers were grown in reverse temperature order, or just the top Pt layer's deposition temperature was varied in the standard order, the

anisotropy changed significantly with deposition temperature. This showed that not only did both interfaces contribute to the effective anisotropy, but they were also affected by annealing. By using a different substrate preparation technique, the anisotropy was also seen to change, even with the standard growth technique, emphasising the sensitivity of the anisotropy to initial growth parameters.

In order to take readings of the domain wall (DW) velocity, a new magnetic coil was designed to provide a sufficient out-of-plane (OOP) field strength to nucleate and propagate domains in the Pt/Co/Pt samples. The DW velocities were measured by expanding bubble domains, and extracted via bespoke python fitting software, as described in Section 3.7.2. Varying the OOP field strength, the velocities were seen to conform to the creep regime for all field strengths used. This extended to expansions under an in-plane (IP) field up to at least 300 Oe, where the characteristic velocity was seen to remain constant but the exponential scaling constant varied as expected due to its dependence upon the DW energy density. An asymmetry was seen between DW velocity with and against the applied IP field, displaying an effect of the Dzyaloshinskii-Moriya interaction (DMI). Out of the three most popular creep models (basic DW energy variation, universal creep law and rough wall model), the basic model was chosen to be used subsequently due to its intuitive nature and the success at fitting the data compared to the rough wall model. Assessing how the extracted DMI changes with structure, the difference between interface disorders taken from X-ray fitting was seen to greatly affect the DMI, even changing its sign. This indicated that the disorder diminishes the DMI, with the relative disorders creating sufficient structural inversion asymmetry to effect a net DMI. This correlated with temperature, the higher temperatures leading to higher DMI values. The base pressure at which the samples were grown, however, also had an effect, with higher base pressures leading to less change with deposition temperature.

Stacks of Pt/Co/Ir₂₀Mn₈₀ have been grown in a similar fashion to Pt/Co/Pt and also displayed an epitaxial nature, seen via X-ray diffraction. To bring the coercivities into a suitable range for DMI measurements, several

growth parameters were investigated. Varying deposition temperature, the coercivity was seen to rise steadily with temperature, with the exchange bias decreasing, reaching a similar value around 300°C. Thus the lowest temperature of 100°C was used to minimise coercivity and utilise the high quality of the interfacial structure responsible for the large exchange bias. Of the working pressures used, the highest was found to give the lowest coercivity in both samples with thick (5 nm) and thin (2 nm) IrMn, with and without exchange bias, respectively. Investigations were then carried out on samples grown at 100°C, with high working pressure, and with varying Co thickness. A peak was seen of coercivity and anisotropy with Co thickness about 0.9 nm which agreed with studies in literature covering a wider range of Co thicknesses. Using Kerr microscopy, a high density of small, rough domains were seen in samples with exchange bias, making them unable to be measured using the bubble expansion technique. Bubble domains were seen in the 0.9 nm sample, although in very inhomogeneous environments that could not be repeated when regrown. Bubble domains were seen, however, in the 2 nm IrMn samples with 0.7 nm and 0.9 nm of Co, though in the 1.1 nm sample a Voronoi-like network of domains was seen indicating sufficient DMI to stabilise a Néel component in the domain walls. Using the domain wall annihilation technique, a minimum bound for DMI constant in the 1.1 nm Co sample was found to be 0.15 ± 0.05 mJ/m², in line with the order of magnitude difference seen between this and other techniques for Pt/Co/AlO_x. Using the basic creep model to fit those samples in which bubble expansion was feasible, the fits worked well at low IP field, but deviated considerably at higher fields. The velocity behaviour differed from Pt/Co/Pt in that at high fields when the velocity was against the applied field, the velocity increased almost linearly with IP field strength, and when it was aligned, the velocity tended to zero with no sign of reaching a minimum. Taking DMI values from the fits, there appeared no difference between the 0.7 nm and 0.9 nm Co samples above uncertainty.

7.1 Future work

Though progress into understanding the intricacies of the DMI has been made in this project, there is still, as always, a vast amount more to be gleaned. Given a more powerful and reliable method for extracting interface disorder, combined with a growth system allowing more controllable growth, the link between interface morphology and DMI can be more firmly established. Looking further afield, the findings of this thesis could be used in magneto-resistive devices to optimise the net DMI, providing an intrinsic in-plane field; a vital feature for several applications to become viable. Epitaxial samples of Pt/Co/Ir₂₀Mn₈₀ were grown and found to have high DMI strengths in an absence of exchange bias (-0.6 to -1.0 mJ/m²). The sign on the net DMI being opposite to Pt/Co/Ir samples was previously undocumented, and so this thesis opens up the possibility of further study into what causes this effect, and could assist in further understanding the mechanism of DMI. Whilst the bubble expansion technique proved unsuitable for samples with exchange bias, other techniques may still be applicable, such as via Brillouin light scattering, which would aid in reaching the goal of comparing DMI strengths in samples with and without exchange biasing.

Bibliography

- [1] A. W. J. Wells, P. M. Shepley, C. H. Marrows, and T. A. Moore. Effect of interfacial intermixing on the Dzyaloshinskii-Moriya interaction in Pt/Co/Pt. *Phys. Rev. B*, 95:054428, 2017.
- [2] A. Hrabec, N. A. Porter, A. Wells, M. J. Benitez, G. Burnell, S. McVitie, D. McGrouther, T. A. Moore, and C. H. Marrows. Measuring and tailoring the Dzyaloshinskii-Moriya interaction in perpendicularly magnetized thin films. *Phys. Rev. B*, 90:020402(R), 2014.
- [3] R. A. Khan, P. M. Shepley, A. Hrabec, A. W. J. Wells, B. Ocker, C. H. Marrows, and T. A. Moore. Effect of annealing on the interfacial Dzyaloshinskii-Moriya interaction in Ta/CoFeB/MgO trilayers. *Appl. Phys. Lett.*, 109:132404, 2016.
- [4] S. Langenfeld, V. Tshitoyan, Z. Fang, A. W. J. Wells, T. A. Moore, and A. J. Ferguson. Exchange magnon induced resistance asymmetry in permalloy spin-Hall oscillators. *Appl. Phys. Lett.*, 108:192402, 2016.
- [5] D. Adams. *The Hitchhiker's Guide to the Galaxy*. Pan Books, 1979.
- [6] O. Smith. Some possible forms of phonograph. *Elec. Wor.*, 1888.
- [7] V. Poulsen. Method of recording and reproducing sounds or signals. *US Pat.*, 1900.
- [8] Seagate. Seagate reaches one terabit per square inch milestone in hard drive storage with new technology demonstration, 2012.

- [9] Seagate. Seagate unveils the industry's broadest 10TB portfolio, 2016.
- [10] S. S. P. Parkin, M. Hayashi, and L. Thomas. Magnetic domain wall racetrack memory. *Science*, 320:190, 2008.
- [11] W. Kang, Y. Huang, C. Zheng, W. Lv, N. Lei, Y. Zhang, X. Zhang, Y. Zhou, and W. Zhao. Voltage controlled magnetic skyrmion motion for racetrack memory. *Sci. Rep.*, 6:23164, 2016.
- [12] S. Zhang and Z. Li. Roles of nonequilibrium conduction electrons on the magnetization dynamics of ferromagnets. *Phys. Rev. Lett.*, 93:127204, 2004.
- [13] S. A. D'Yachenko, V. F. Kovalenko, B. N. Tanygin, and A. V. Tychko. Influence of the demagnetizing field on the structure of a bloch wall in a (001) plate of a magnetically ordered cubic crystal. *Phys. Sol. State*, 50, 2008.
- [14] J. H. Franken, M. Herps, H. J. M. Swagten, and B. Koopmans. Tunable chiral spin texture in magnetic domain-walls. *Sci. Rep.*, 4:5248, 2014.
- [15] M. Vaňatka, J.-C. Rojas-Sánchez, J. Vogel, M. Bonfirm, M. Belmeguenai, Y. Roussigné, A. Stahkevish, A. Thiaville, and S. Pizzini. Velocity asymmetry of Dzyaloshinskii domain walls in the creep and flow regimes. *Jour. Phys.: Cond. Matt.*, 27:325002, 2015.
- [16] A. Thiaville, S. Rohart, E. Jué, V. Cros, and A. Fert. Dynamics of Dzyaloshinskii domain walls in ultrathin magnetic films. *Europhys. Lett.*, 100:57002, 2012.
- [17] S. Emori, U. Bauer, S.-M. Ahn, E. Martinez, and G. S. D. Beach. Current-driven dynamics of chiral ferromagnetic domain walls. *Nat. Mat.*, 12:611, 2013.
- [18] S.-G. Je, D.-H. Kim, S.-C. Yoo, B.-C. Min, K.-J. Lee, and S.-B. Choe. Asymmetric magnetic domain-wall motion by the dzyaloshinskii-moriya interaction. *Phys. Rev. B*, 88:214401, 2013.

- [19] R. Lavrijsen, D. M. F. Hartmann, A. van den Brink, Y. Yin, B. Barcones, R. A. Duine, M. A. Verheijen, H. J. M. Swagten, and B. Koopmans. Asymmetric magnetic bubble expansion under in-plane field in Pt/Co/Pt: Effect of interface engineering. *Phys. Rev. B*, 91:104414, 2015.
- [20] F. C. Ummelen, D.-S. Han, J.-S. Kim, H. J. M. Swagten, and B. Koopmans. Asymmetric domain-wall depinning induced by Dzyaloshinskii-Moriya interaction. *IEEE Trans. Magn.*, page DOI 10.1109/TMAG.2015.2437453, 2015.
- [21] J. Sampaio, V. Cros, S. Rohart, A. Thiaville, and A. Fert. Nucleation, stability and current-induced motion of isolated magnetic skyrmions in nanostructures. *Nat. Nano.*, 8:839, 2013.
- [22] X. Zhang, M. Ezawa, and Y. Zhou. Magnetic skyrmion logic gates: conversion, duplication and merging of skyrmions. *Sci. Rep.*, 6:9400, 2015.
- [23] D. A. Allwood, G. Xiong, C. C. Faulkner, D. Atkinson, D. Petit, and R. P. Cowburn. Magnetic domain-wall logic. *Science*, 309:1688, 2005.
- [24] K.-W. Moon, D.-H. Kim, S.-C. Yoo, S.-G. Je, B. S. Chun, W. Kim, B.-C. Min, C. Hwang, and S.-B. Choe. Magnetic bubblecade memory based on chiral domain walls. *Sci. Rep.*, 5:9166, 2015.
- [25] D. Petit, P. R. Seem, M. Tillette, R. Mansell, and R. P. Cowburn. Two-dimensional control of field-driven magnetic bubble movement using Dzyaloshinskii-Moriya interactions. *Appl. Phys. Lett.*, 106:022402, 2015.
- [26] V. Mathet, T. Devolder, C. Chappert, J. Ferre, S. Lemerle, L. Belliard, and G. Guentherodt. Morphology and magnetic properties of Pt/Co/Pt sandwiches grown by argon sputter deposition. *Jour. Mag. Mat.*, 260:295–304, 2003.

- [27] Kitada M. and N. Shimizu. Magnetic properties of sputtered Co-Pt thin films. *Jour. Appl. Phys.*, 54:7089, 1983.
- [28] F. Menzinger and A. Paoletti. Magnetic moments and unpaired-electron densities in CoPt₃. *Phys. Rev.*, 143, 1966.
- [29] T. R. McGuire, J. A. Aboaf, and E. Klokhholm. Magnetic and transport properties of Co-Pt thin films. *Jour. Appl. Phys.*, 55:1951, 1984.
- [30] P. F. Carcia. Perpendicular magnetic anisotropy in Pd/Co and Pt/Co thin-film layered structures. *Jour. Appl. Phys.*, 63:5066, 1988.
- [31] L. Néel. Anisotropie magnétique superficielle et surstructures d'orientation. *J. Phys. Radium*, 15, 1954.
- [32] W. B. Zeper, F. J. A. M. Greidanus, P. F. Carcia, and C. R. Fincher. Perpendicular magnetic anisotropy and magneto-optical Kerr effect of vapor-deposited Co/Pt-layered structures. *Jour. Appl. Phys.*, 65:4971, 1989.
- [33] C.-J. Lin, G.-L. Gorman, C. H. Lee, R. F. C. Farrow, E. E. Marinero, H. V. Do, H. Notarys, and C. J. Chien. Magnetic and structural properties of Co/Pt multilayers. *Jour. Mag. Mag. Mat.*, 93:194–206, 1991.
- [34] F. J. A. den Broeder, D. Kuiper, H. C. Donkersloot, and W. Hoving. A comparison of the magnetic anisotropy of [001] and [111] oriented Co/Pd multilayers. *Appl. Phys.*, pages 507–512, 1989.
- [35] P. Bruno. Tight-binding approach to the orbital magnetic moment and magnetocrystalline anisotropy of transition-metal monolayers. *Phys. Rev. B*, 39, 1989.
- [36] P. F. Carcia, Z. G. Li, and W. B. Zeper. Effect of sputter-deposition processes on the microstructure and magnetic properties of Pt/Co multilayers. *Jour. Mag. Mag. Mat.*, 121:452–460, 1993.

- [37] S. Ferrer, J. Alvarez, E. Lundgren, X. Torrelles, P. Fajardo, and F. Boscherini. Surface X-ray diffraction from Co/Pt(111) ultrathin films and alloys: Structure and magnetism. *Phys. Rev. B*, 56, 1997.
- [38] E. Lundgren, B. Stanka, M. Schmid, and P. Varga. Thin films of Co on Pt(111): Strain relaxation and growth. *Phys. Rev. B*, 62, 2000.
- [39] N. Nakajima, T. Koide, T. Shidara, H. Miyauchi, H. Fukutani, A. Fujimori, K. Iio, T. Katayama, M. Nyvlt, and Y. Suzuki. Perpendicular magnetic anisotropy caused by interfacial hybridization via enhanced orbital moment in Co/Pt multilayers: Magnetic circular X-ray dichroism study. *Phys. Rev. Lett.*, 81, 1998.
- [40] P. J. Metaxas, J. P. Jamet, A. Mougin, M. Cormier, J. Ferré, V. Baltz, B. Rodmacq, B. Dieny, and R. L. Stamps. Creep and flow regimes of magnetic domain-wall motion in ultrathin Pt/Co/Pt films with perpendicular anisotropy. *Phys. Rev. Lett.*, 99:217208, 2007.
- [41] A. V. Khvalkovskiy, V. Cros, D. Apalkov, V. Nikitin, M. Krounbi, K. A. Zvezdin, A. Anane, J. Grollier, and A. Fert. Matching domain-wall configuration and spin-orbit torques for efficient domain-wall motion. *Phys. Rev. B*, 87:020402(R), 2013.
- [42] P. M. Haney, R. A. Duine, A. S. Núñez, and A. H. MacDonald. Current-induced torques in magnetic metals: Beyond spin-transfer. *J. Mag. Mag. Mat.*, 320:1300–1311, 2008.
- [43] A. Manchon, H. C. Koo, J. Nitta, S. M. Frolov, and R. A. Duine. New perspectives for Rashba spinorbit coupling. *Nat. Mat.*, 14:871–882, 2015.
- [44] E. Hall. On a new action of the magnet on electric currents. *Am. Jour. Math.*, 2, 1879.
- [45] N. W. Ashcroft and N. D. Mermin. *Solid State Physics*. Brooks Cole, 1976.

- [46] R. Karplus and J. M. Luttinger. Hall effect in ferromagnetics. *Phys. Rev.*, 95:1154, 1954.
- [47] J. Smit. The spontaneous Hall effect in ferromagnetics I. *Physica*, 21:877–887, 1955.
- [48] L. Berger. Influence of spin-orbit interaction on the transport processes in ferromagnetic nickel alloys, in the presence of a degeneracy of the 3d band. *Physica*, 30:1141–1159, 1964.
- [49] M. I. D'yakonov and V. I. Perel. Possibility of orienting electron spins with current. *JETP Lett.*, 13, 1971.
- [50] E. Martinez and G. Finocchio. Domain wall dynamics in asymmetric stacks: The roles of Rashba field and the spin Hall effect. *Trans. Mag.*, 49, 2013.
- [51] P. Chauve, T. Giamarchi, and P. Le Doussal. Creep and depinning in disordered media. *Phys. Rev. B*, 62, 2000.
- [52] S. Lemerle, J. Ferré, C. Chappert, V. Mathet, T. Giamarchi, and P. Le Doussal. Domain wall creep in an Ising ultrathin magnetic film. *Phys. Rev. Lett.*, 80, 1998.
- [53] G. Blatter, M. V. Feigel'man, V. B. Geshkenbein, Larkin A. I., and V. M. Vinokur. Vortices in high-temperature superconductors. *Rev. Mod. Phys.*, 66:1125, 1994.
- [54] D. A. Huse, C. L. Henley, and D. S. Fisher. Huse, Henley, and Fisher respond. *Phys. Rev. Lett.*, 55, 1985.
- [55] A. P. Mihai, A. L. Whiteside, E. J. Canwell, C. H. Marrows, M. J. Benitez, D. McGrouther, S. McVitie, S. McFadzean, and T. A. Moore. Effect of substrate temperature on the magnetic properties of epitaxial sputter-grown Co/Pt. *Appl. Phys. Lett.*, 103:262401, 2013.
- [56] J. Gorchon, S. Bustingorry, J. Ferré, V. Jeudy, A. B. Kolton, and T. Giamarchi. Pinning-dependent field-driven domain wall dynamics

-
- and thermal scaling in an ultrathin Pt/Co/Pt magnetic film. *Phys. Rev. Lett.*, 113:027205, 2014.
- [57] V. Jeudy, A. Mougin, S. Bustingorry, W. Savero Torres, J. Gorchon, A. B. Kolton, A. Lemaitre, and J.-P. Jamet. Universal pinning energy barrier for driven domain walls in thin ferromagnetic films. *Phys. Rev. Lett.*, 117:057201, 2016.
- [58] A. B. Kolton, A. R. Rosso, T. Giamarchi, and W. Krauth. Creep dynamics of elastic manifolds via exact transition pathways. *Phys. Rev. B*, 79:184207, 2009.
- [59] D. J. Griffiths. *Introduction to Quantum Mechanics (2nd Edition)*. Pearson Prentice Hall, 2nd edition, 2004, 2004.
- [60] I. Dzyaloshinsky. A thermodynamic theory of weak ferromagnetism of antiferromagnetics. *J. Phys. Chem. Solids*, 4:241–255, 1958.
- [61] T. Moriya. Anisotropic superexchange interaction and weak ferromagnetism. *Phys. Rev.*, 120, 1960.
- [62] H. Yang, A. Thiaville, S. Rohart, A. Fert, and M. Chshiev. Anatomy of Dzyaloshinskii-Moriya interaction at Co/Pt interfaces. *Phys. Rev. Lett.*, 115:267210, 2015.
- [63] M. Bode, M. Heide, K. von Bergmann, P. Ferriani, S. Heinze, G. Bihlmayer, A. Kubetzka, O. Peitzsch, S. Blügel, and R. Wiesendanger. Chiral magnetic order at surfaces driven by inversion asymmetry. *Nat. Lett.*, 447:190–193, 2007.
- [64] G. Chen, A. T. N’Diaye, S. P. Kang, H. Y. Kwon, C. Won, Y. Wu, Z. Q. Qiu, and A. K. Schmid. Unlocking bloch-type chirality in ultrathin magnets through uniaxial strain. *Nat. Com.*, 6:6598, 2015.
- [65] I. M. Miron, T. Moore, H. Szambolics, L. D. Buda-Prejbeanu, S. Auffret, B. Rodmacq, S. Pizzini, J. Vogel, M. Bonfim, A. Schuhl, and G. Gaudin. Fast current-induced domain-wall motion controlled by the Rashba effect. *Nat. Mat.*, 10:419–423, 2011.

- [66] K.-S. Ryu, L. Thomas, S.-H. Yang, and S. Parkin. Chiral spin torque at magnetic domain walls. *Nat. Nano.*, 8:527, 2013.
- [67] G. Chen, T. Ma, A. T. N'Diaye, H. Kwon, C. Won, Y. Wu, and A. K. Schmid. Tailoring the chirality of magnetic domain walls by interface engineering. *Nat. Com.*, 4:2671, 2013.
- [68] K.-S. Ryu, S.-H. Yang, L. Thomas, and S. S. P. Parkin. Chiral spin torque arising from proximity-induced magnetization. *Nat. Com.*, 5:3910, 2014.
- [69] S. Kim, K. Ueda, G. Go, P.-H. Jang, K.-J. Lee, A. Belabbes, M. Manchon, A. amd Suzuki, Y. Kotani, T. Nakamura, K. Nakamura, T. Koyama, D. Chiba, K. Yamada, D.-H. Kim, T. Moriyama, K.-J. Kim, and T. Ono. Microscopic origin of interfacial Dzyaloshinskii-Moriya interaction. *arXiv*, 1704:02900, 2017.
- [70] D.-H. Kim, S.-C. Yoo, D.-Y. Kim, K.-W. Moon, S.-G. Je, C.-G. Cho, B.-C. Min, and S.-B. Choe. Maximizing domain-wall speed via magnetic anisotropy adjustment in Pt/Co/Pt films. *Appl. Phys. Lett.*, 104:142410, 2014.
- [71] D. Lau, V. Sundar, J.-G. Zhu, and V. Sokalski. Energetic molding of chiral magnetic bubbles. *Phys. Rev. B*, 94:060401(R), 2016.
- [72] C. Herring. Konferenz über struktur und eigenschaften fester oberflächen lake. geneva (wisconsin) usa, 29. september bis 1. oktober 1952. *Angew. Chem.*, 65:34, 1953.
- [73] J. P. Pellegren, D. Lau, and V. Sokalski. Dispersive stiffness of Dzyaloshinskii domain walls. *Phys. Rev. Lett.*, 119:027203, 2017.
- [74] D.-Y. Kim, M.-H. Park, Y.-K. Park, J.-S. Kim, Y.-S. Nam, D.-H. Kim, S.-G. Je, B.-C. Min, and S.-B. Choe. Chirality-induced antisymmetry in magnetic domain-wall speed. *arXiv*, 1704:08751, 2017.
- [75] W. H. Meiklejohn and C. P. Bean. New magnetic anisotropy. *Phy. Rev.*, 102, 1956.

- [76] M. Ali, C. H. Marrows, and B. J. Hickey. Onset of exchange bias in ultrathin antiferromagnetic layers. *Phy. Rev. B*, 67:172405, 2003.
- [77] M. Ali, C. H. Marrows, M. Al-Jawad, B. J. Hickey, A. Misra, U. Nowak, and K. D. Usadel. Antiferromagnetic layer thickness dependence of the IrMn/Co exchange-bias system. *Phy. Rev. B*, 68:214420, 2003.
- [78] A. P. Malozemoff. Random-field model of exchange anisotropy at rough ferromagnetic-antiferromagnetic interfaces. *Phy. Rev. B*, 35:3679, 1987.
- [79] J. Sort, V. Baltz, F. Garcia, B. Rodmacq, and B. Dieny. Tailoring perpendicular exchange bias in [Pt/Co]-IrMn multilayers. *Phys. Rev. B*, 71:054411, 2005.
- [80] A. van den Brink, G. Vermeij, A. Solignac, J. Koo, J. T. Kohlhepp, H. J. M. Swagten, and B. Koopmans. Field-free magnetization reversal by spin-Hall effect and exchange bias. *Nat. Com.*, 7:10854, 2016.
- [81] S. Fukami, C. Zhang, S. DuttaGupta, A. Kurenkov, and H. Ohno. Magnetization switching by spinorbit torque in an antiferromagnet-ferromagnet bilayer system. *Nat. Mat.*, 15:535, 2016.
- [82] A. Kohn, A. Kovács, R. Fan, G. J. McIntyre, R. C. C. Ward, and J. P. Goff. The antiferromagnetic structures of IrMn₃ and their influence on exchange-bias. *Sci. Rep.*, 3:02412, 2013.
- [83] R. Yanes, J. Jackson, L. Udvardi, L. Szunyogh, and U. Nowak. Exchange bias driven by Dzyaloshinskii-Moriya interactions. *Phys. Rev. Lett.*, 111:217202, 2013.
- [84] W. Zhang and K. M. Krishnan. Epitaxial exchange-bias systems: From fundamentals to future spin-orbitronics. *Mat. Sci. and Eng. R*, 105:1–20, 2016.

- [85] C. L. Canedy, X. W. Li, and G. Xiao. Extraordinary Hall effect in (111) and (100)-orientated Co/Pt superlattices. *Jour. App. Phys.*, 81:5367, 1997.
- [86] P. Sigmund. Theory of sputtering. I. sputtering yield of amorphous and polycrystalline targets. *Phys. Rev.*, 184, 1969.
- [87] M. C. Saint-Lager, R. Baudoing-Savois, M. De Santis, P. Dolle, and Y. Gauthier. Thickness effect on alloying of ultrathin Co films on Pt(111): a real time and in situ UHV study with synchrotron X-ray diffraction. *Sur. Sci.*, 418:485–492, 1998.
- [88] H. Kiessig. Interferenz von Röntgenstrahlen an dünnen schichten. *Ann. Phys.*, 402, 1931.
- [89] D. E. Savage, J. Kleiner, N. Schimke, Y.-H. Phang, T. Jankowski, J. Jacobs, R. Kariotis, and M. G. Lagally. Determination of roughness correlations in multilayer films for X-ray mirrors. *Jour. Appl. Phys.*, 69:1411, 1991.
- [90] L. Grave De Peralta. *Thin film characterisation by X-ray reflectivity*. PhD thesis, Texas Tech University, 2000.
- [91] J. Kerr. On rotation of the plane of polarization by reflection from the pole of a magnet. *Phil. Mag.*, 5, 1877.
- [92] M. Faraday. Experimental researches in electricity. nineteenth series. *Phil. Trans.*, 136:1–20, 1846.
- [93] J. Zak, E. R. Moog, C. Liu, and S. D. Bader. Fundamental magneto-optics. *J. App. Phys.*, 68:4203, 1990.
- [94] H. Ohldag, A. Scholl, F. Nolting, E. Arenholz, S. Maat, A. T. Young, M. Carey, and J. Stohr. Correlation between exchange bias and pinned interfacial spins. *Phys. Rev. Lett.*, 91:017203, 2003.
- [95] K.-W. Moon, J.-C. Lee, S.-B. Choe, and K.-H. Shin. Determination of perpendicular magnetic anisotropy in ultrathin ferromagnetic films by

- extraordinary Hall voltage measurement. *Rev. Sci. Inst.*, 80:113904, 2009.
- [96] M. J. Benitez, A. Hrabec, A. P. Mihai, T. A. Moore, G. Burnell, D. McGrouther, C. H. Marrows, and S. McVitie. Magnetic microscopy and topological stability of homochiral Néel domain walls in a Pt/Co/AlO_x trilayer. *Nat. Comm.*, 6:8957, 2015.
- [97] R. Lo Conte, E. Martinez, A. Hrabec, A. Lamperti, T. Schulz, L. Nasi, L. Lazzarini, R. Mantovan, F. Maccherozzi, S. S. Dhesi, B. Ocker, C. H. Marrows, T. A. Moore, and M. Kläui. Role of B diffusion in the interfacial Dzyaloshinskii-Moriya interaction in Ta/Co₂₀Fe₆₀B₂₀/MgO nanowires. *Phys. Rev. B*, 91:014433, 2015.
- [98] D.-S. Han, N.-H. Kim, J.-S. Kim, Y. Yin, J.-W. Koo, J. Cho, L. Sukmock, M. Kläui, H. J. M. Swagten, B. Koopmans, and C.-Y. You. Asymmetric hysteresis for probing Dzyaloshinskii-Moriya interaction. *Nano Lett.*, 16, 2016.
- [99] Y. Nie, X. Yang, P. Zhang, and H. Sang. Magnetization and coercivity in Co/Pt multilayers with constant total Co layer thickness. *Trans. Nonferrous Met. Soc. China*, 20, 2010.
- [100] K. Ando, S. Takahashi, K. Harii, K. Sasage, J. Ieda, S. Maekawa, and E. Saitoh. Electric manipulation of spin relaxation using the spin Hall effect. *Phys. Rev. Lett.*, 101, 2008.
- [101] C.-F. Pai, Y. Ou, L. H. Vilela-Leao, D. C. Ralph, and R. A. Buhrman. Dependence of the efficiency of spin Hall torque on the transparency of Pt/ferromagnetic layer interfaces. *Phys. Rev. B*, 92:064426, 2015.
- [102] T. A. Moore, I. M. Miron, G. Gaudin, G. Serret, S. Auffret, B. Rodmacq, A. Schul, S. Pizzini, J. Vogel, and M. Bonfim. High domain wall velocities induced by current in ultrathin Pt/Co/AlO_x wires with perpendicular magnetic anisotropy. *Appl. Phys. Lett.*, 93:262504, 2008.

- [103] F. Ono and H. Maeta. Determination of lattice parameters in hcp cobalt by using X-ray Bonds method. *Jour. Phys. Coll.*, 49, 1988.
- [104] J. W. Arblaster. Crystallographic properties of platinum. *Plat. Met. Rev.*, 41, 1997.
- [105] Y. V. Shvyd'ko, M. Lucht, E. Gerdau, M. Lerche, E. E. Alp, W. Sturhahn, J. Sutter, and T. S. Toellner. Measuring wavelengths and lattice constants with the Mossbauer wavelength standard. *J. Synchrotron Rad.*, 9:17–23, 2002.
- [106] M. Ota, M. Itou, Y. Sakurai, A. Koizuma, and H. Sakurai. Perpendicular magnetic anisotropy in Co/Pt multilayers studied from a view point of anisotropy of magnetic Compton profiles. *Appl. Phys. Lett.*, 96:152505, 2010.
- [107] Y. An, L. Duan, T. Liu, Z. Wu, and J. Liu. Structural and magnetic properties of Pt in Co/Pt multilayers. *Appl. Sur. Sci.*, 257:7427–7431, 2011.
- [108] T. Ueno, J. Sinha, N. Inami, Y. Takeichi, S. Mitani, K. Ono, and M. Hayashi. Enhanced orbital magnetic moments in magnetic heterostructures with interface perpendicular magnetic anisotropy. *Sci. Rep.*, 5:14858, 2015.
- [109] S. Emori, E. Martinez, K.-J. Lee, H.-W. Lee, U. Bauer, S.-M. Ahn, P. Agrawal, D. C. Bono, and G. S. D. Beach. Spin Hall torque magnetometry of Dzyaloshinskii domain walls. *Phys. Rev. B*, 90:184427, 2014.
- [110] S. Pizzini, J. Vogel, S. Rohart, L. D. Buda-Prejbeanu, E. Jué, O. Boulle, I. M. Miron, C. K. Safeer, S. Auffret, G. Gaudin, and A. Thiaville. Chirality-induced asymmetric magnetic nucleation in Pt/Co/AlO_x ultrathin microstructures. *Phys. Rev. Lett.*, 113:047203, 2014.

-
- [111] M. Belmeguenai, J.-P. Adam, Y. Roussigné, S. Eimer, T. Devolder, J.-V. Kim, S. M. Cherif, A. Stashkevich, and A. Thiaville. Interfacial Dzyaloshinskii-Moriya interaction in perpendicularly magnetized Pt/Co/AlO_x ultrathin films measured by Brillouin light spectroscopy. *Phys. Rev. B*, 91:180405(R), 2015.
- [112] V. Holy, J. Kubena, and I. Ohlídal. X-ray reflection from rough layered systems. *Phys. Rev. B*, 47, 1993.
- [113] Y. H. Phang, D. E. Savage, R. Kariotis, and M. G. Lagally. X-ray diffraction measurement of partially correlated interfacial roughness in multilayers. *Jour. Appl. Phys.*, 74:3181, 1993.
- [114] K. Inaba, S. Kobayashi, K. Uehara, A. Okada, S. L. Reddy, and T. Endo. High resolution X-ray diffraction analyses of (La,Sr)MnO₃/Zn/sapphire(0001) double heteroepitaxial films. *Adv. Mat. Phys. Chem.*, 3:72–89, 2013.
- [115] H. Huang, X. Hu, J. Zhang, N. Su, and J. Cheng. Facile fabrication of platinum-cobalt alloy nanoparticles with enhanced electrocatalytic activity for a methanol oxidation reaction. *Sci. Rep.*, 7:45555, 2017.
- [116] N. Kato. A theoretical study of Pendellosung fringes. Part I. general considerations. *Acta Cryst.*, 14:526–532, 1961.
- [117] R. W. G. Wyckoff. *Crystal Structures 1, second edition*. Interscience Publishers, 1963.
- [118] T. K. Hatwar and T. N. Blanton. Highly ordered Co/Pt superlattice thin films prepared using ultrathin seed layers. *Trans. Mag.*, 33, 1997.
- [119] C. T. Chantler, K. Olsen, R. A. Dragoset, J. Chang, A. R. Kishore, S. A. Kotochigova, and D. S. Zucker. X-ray form factor, attenuation, and scattering tables. *NIST Phys. Meas. Lab.*, 14:526–532, 2005.
- [120] M. Wormington, C. Panaccione, K. M. Matney, and D. K. Bowen. Characterization of structures from X-ray scattering data using genetic algorithms. *TRS Phil. Trans. A*, 357:1761, 1999.

- [121] P. Beliën, R. Schad, C. D. Potter, G. Verbanck, V. V. Moshchalkov, and Y. Bruynseraede. Relation between interface roughness anti giant magnetoresistance in MBE-grown polycrystalline Fe/Cr superlattices. *Phys. Rev. B*, 50, 1994.
- [122] M. Salvato, A. Aurigemma, A. Tesauero, and C. Attansio. Surface and structural disorder in MBE and sputtering deposited Cu thin films revealed by X-ray measurements. *Vac.*, 82:556–560, 2008.
- [123] Y. Yoneda. Anomalous surface reflection of X-rays. *Phys. Rev.*, 131, 1963.
- [124] L. G. Schulz and F. R. Tangherlini. Optical constants of silver, gold, copper, and aluminum. II. The index of refraction n . *J. Opt. Soc. Amer.*, 44:362, 1954.
- [125] J. Ferré, C. Chappert, H. Bernas, J.-P. Jamet, P. Meyer, O. Kaitasov, S. Lemerle, V. Mathet, F. Rousseaux, and H. Launois. Irradiation induced effects on magnetic properties of Pt/Co/Pt ultrathin films. *J. Magn. Magn. Mat.*, 198, 1999.
- [126] J.-H. Kim and S.-C. Shin. Interface roughness effects on the surface anisotropy in Co/Pt multilayer films. *J. Appl. Phys.*, 80:3121, 1996.
- [127] S. Bandiera, R. C. Sousa, B. Rodmacq, and B. Dieny. Enhancement of perpendicular magnetic anisotropy through reduction of Co-Pt interdiffusion in (Co/Pt) multilayers. *Appl. Phys. Lett.*, 100:142410, 2012.
- [128] O. Robach, C. Quiros, P. Steadman, K. F. Peters, E. Lundgren, J. Alvarez, H. Isern, and S. Ferrer. Magnetic anisotropy of ultrathin cobalt films on pt(111) investigated with X-ray diffraction: Effect of atomic mixing at the interface. *Phys. Rev. B*, 65:054423, 2002.
- [129] M. Quinsat, Y. Ootera, T. Shimada, M. Kado, S. Hashimoto, H. Morise, S. Nakamura, and T. Kondo. Dzyaloshinskii-Moriya interaction in Pt/Co/Pt films prepared by chemical vapor deposition with various substrate temperatures. *AIP Adv.*, 7:056318, 2017.

- [130] J. Alvarez, E. Lundgren, X. Torrelles, H. Isern, K. F. Peters, P. Steadman, and S. Ferrer. Magnetization of Pt in the Co/Pt(110) system investigated with surface X-ray magnetic diffraction: Evidence for in-plane magnetic anisotropy. *Phys. Rev. B*, 60, 1999.
- [131] J. Okabayashi, T. Koyama, M. Suzuki, M. Tsujikawa, M. Shirai, and D. Chiba. Induced perpendicular magnetization in a Cu layer inserted between Co and Pt layers revealed by X-ray magnetic circular dichroism. *Sci. Rep.*, 7:46132, 2017.
- [132] M. J. Sablik. Modeling the effect of grain size and dislocation density on hysteretic magnetic properties in steels. *J. Appl. Phys.*, 89:5610, 2001.
- [133] A. K. Lindquist, J. M. Feinberg, R. J. Harrison, J. C. Loudon, and A. J. Newell. Domain wall pinning and dislocations: Investigating magnetite deformed under conditions analogous to nature using transmission electron microscopy. *J. Geophys. Res. Solid Earth*, 120:1415–1430, 2015.
- [134] P. M. Shepley, H. Tunncliffe, K. Shahbazi, G. Burnell, and T. A. Moore. Tuning domain wall energy with strain: balancing anisotropy and exchange energies in Pt/Co/Ir. *arXiv*, 1703:05749, 2017.
- [135] R. Diaz Pardo, W. Saverio Torres, A. B. Kolton, S. Bustingorry, and V. Jeudy. Universal depinning transition of domain walls in ultrathin ferromagnets. *Phys. Rev. B*, 95:184434, 2017.
- [136] J. D. Evans. *Straightforward Statistics for the Behavioral Sciences*. Brooks/Cole Publishing Company, 1996.
- [137] A. L. Balk, K.-W. Kim, D. T. Pierce, M. D. Stiles, J. Unguris, and S. M. Stavis. Simultaneous control of the Dzyaloshinskii-Moriya interaction and magnetic anisotropy in nanomagnetic multilayers. *arXiv*, 1609:09790, 2016.

- [138] Y. H. Park, J. W. Choi, J. Chang, H.-J. Choi, and H. C. Koo. Exchange-biased ferromagnetic electrodes and their application to complementary spin transistors. *Curr. Appl. Phys.*, 15:532–535, 2015.
- [139] S.-H. Yang, K.-S. Ryu, and S. Parkin. Domain-wall velocities of up to 750 m/s driven by exchange-coupling torque in synthetic antiferromagnets. *Nat. Nano.*, 10:221–226, 2015.
- [140] V. Tshitoyan, C. Ciccarelli, A. P. Mihai, M. Ali, A. C. Irvine, T. A. Moore, T. Jungwirth, and A. J. Ferguson. Electrical manipulation of ferromagnetic NiFe by antiferromagnetic IrMn. *Phys. Rev. B*, 92:214406, 2015.
- [141] L. Frangou, S. Oyarzun, S. Auffret, L. Vila, S. Gambarelli, and V. Baltz. Enhanced spin pumping efficiency in antiferromagnetic IrMn thin films around the magnetic phase transition. *Phys. Rev. Lett.*, 116:077203, 2016.
- [142] J. Moritz, P. Bacher, and B. Dieny. Numerical study of the influence of interfacial roughness on the exchange bias properties of ferromagnetic/antiferromagnetic bilayers. *Phys. Rev. B*, 94:104425, 2016.
- [143] P. He, W. A. McGahan, S. Nafis, J. A. Woollam, Z. S. Sham, S. H. Liou, F. Sequeda, T. McDaniel, and H. Do. Sputtering pressure effect on microstructure of surface and interface, and on coercivity of Co/Pt multilayers. *Jour. Appl. Phys.*, 70:6044, 1991.
- [144] X. Ji and K. Krishnan. Competing magnetic interactions in perpendicular exchange-biased $[\text{Co/Pt}]_y/\text{FeMn}$ multilayers. *J. Appl. Phys.*, 99:08C105, 2006.
- [145] J. Camarero, J. J. de Miguel, R. Miranda, and A. Hernando. Thickness-dependent coercivity of ultrathin Co films grown on Cu(111). *J. Phys.: Condens. Matter*, 12:7713, 2000.

- [146] A. Diaz-Ortiz, F. Aguilera-Granja, and J. L. Moran-Lopez. Equilibrium thermodynamics of cobalt-copper slabs. *Phys. Rev. B*, 53:6514, 1996.
- [147] T. Kingetsu. Dependence of coercivity on Co layer thickness in (111)Pd/Co superlattices grown by molecular-beam epitaxy. *Jpn. J. Appl. Phys.*, 33:1890–1891, 1994.
- [148] D. Weller, H. Notarys, T. Suzuki, G. Gorman, T. Logan, and I. McFadyen. Thickness dependent coercivity in sputtered Co/Pt multilayers. *Trans. Mag.*, 28, 1992.
- [149] Q. Jiang, H.-N. Yang, and G.-C. Wang. Effect of interface roughness on hysteresis loops of ultrathin Co films from 2 to 30 ML on Cu(001) surfaces. *Surf. Sci.*, 373:181–194, 1997.
- [150] J.-Y. Chen, J.-F. Feng, Z. Diao, G. Feng, J. M. D. Coey, and X.-F. Han. Magnetic properties of exchange-biased [Co/Pt]_n multilayer with perpendicular magnetic anisotropy. *Trans. Mag.*, 46, 2010.
- [151] Y. F. Liu, J. W. Cai, and S. L. He. Large perpendicular exchange bias in IrMn/CoFe/[Pt/Co] multilayers grown on a Ta/Pt buffer layer. *J. Phys. D: Appl. Phys.*, 42:115002, 2009.
- [152] S. van Dijken, M. Besnier, J. Moritz, and J. M. D. Coey. IrMn as exchange-biasing material in systems with perpendicular magnetic anisotropy. *Jour. Appl. Phys.*, 97:10K114, 2005.
- [153] J. Kanak, T. Stobiecki, and S. van Dijken. Influence of interface roughness, film texture, and magnetic anisotropy on exchange bias in [Pt/Co]₃/IrMn and IrMn/[Co/Pt]₃ multilayers. *IEEE Trans. Mag.*, 44, 2008.
- [154] F. Romanens, S. Pizzini, F. Yokaichita, M. Bonfim, Y. Pennec, J. Camarero, J. Vogel, J. Sort, F. Garcia, B. Rodmacq, and B. Dieny. Magnetic relaxation of exchange biased Pt/Co multilayers studied by time-resolved Kerr microscopy. *Phys. Rev. B*, 72:134410, 2005.

- [155] C. Moreau-Luchaire, C. Moutafis, N. Reyren, J. Sampaio, C. A. F. Vaz, N. Van Horne, K. Bouzehouane, K. Garcia, C. Deranlot, P. Warnicke, P. Wohlhüter, J.-M. George, M. Weigand, J. Raabe, V. Cros, and A. Fert. Additive interfacial chiral interaction in multilayers for stabilization of small individual skyrmions at room temperature. *Nat. Nano.*, 11:444–448, 2016.
- [156] W. J. Kong, Y. R. Ji, X. Zhang, H. Wu, Q. T. Zhang, Z. H. Yuan, C. H. Wan, X. F. Han, T. Yu, K. Fukuda, H. Naganuma, and M.-J. Tung. Field-free spin Hall effect driven magnetization switching in Pd/Co/IrMn exchange coupling system. *Appl. Phys. Lett.*, 109:132402, 2016.
- [157] X. Ma, G. Yu, S. A. Razavi, S. S. Sasaki, X. Li, K. Hao, S. H. Tolbert, K. L. Wang, and X. Li. DzyaloshinskiiMoriya interaction across antiferromagnet / ferromagnet interface. *arXiv*, 1706:00535, 2017.

Appendix A

Domain wall velocity fits

For the purposes of being translucent, further fits of the basic domain wall energy density variation creep law model to domain wall velocity against applied in-plane field data from Pt/Co/Pt samples are provided.

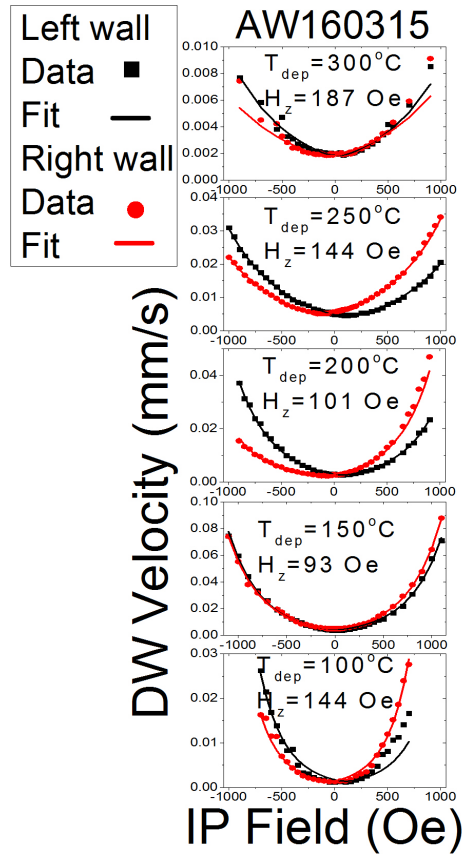


Figure A.1: Examples of fits to DW velocity vs IP field data using the basic DW energy variation model. Data from samples of set type A at different deposition temperatures are presented.